CHARGE CARRIER DYNAMICS AND DEFECT GENERATION AT THE SI/SIO$_2$ INTERFACE PROBED BY FEMTOSECOND OPTICAL SECOND HARMONIC GENERATION

Dissertation

zur Erlangung des akademischen Grades
Doctor rerum naturalium (Dr. rer. nat.)

vorgelegt dem Rat der Physikalisch-Astronomischen Fakultät
der Friedrich-Schiller-Universität Jena

von Dipl.-Phys. Torsten Scheidt
geboren am 27. Nov. 1974 in Würzburg

1. Gutachter:	Prof. Dr. H. Stafast Institut für Physikalische Hochtechnologie (IPHT) und Physikalisch-Astronomische Fakultät Friedrich-Schiller-Universität Jena
2. Gutachter:	Prof. Dr. R. Sauerbrey Institut für Optik und Quantenelektronik Physikalisch-Astronomische Fakultät Friedrich-Schiller-Universität Jena
3. Gutachter:	Prof. Dr. Dr. h. c. A. Laubereau Fakultät für Physik Physik Department E11 Technische Universität München

Tag der letzten Rigorosumsprüfung:	1. Juli 2005
Tag der öffentlichen Verteidigung:	5. Juli 2005

Nkosi sikelel’ iAfrika
May her spirit rise high up

Contents

Introduction **3**

1 State of Research **5**

2 Theoretical Background **10**

2.1 Maxwell’s Equations 10

2.2 Nonlinear Polarization 11

2.3 Nonlinear Wave Equation 12

2.4 Second Order Susceptibility Tensor 14

2.4.1 Definition 14

2.4.2 Symmetry Properties 14

2.4.3 Contracted Notation 15

2.5 SHG in Reflection from Centrosymmetric Media 16

2.5.1 Fields from General Bulk and Surface Sources 16

2.5.1.1 Fields from General Bulk Sources 18

2.5.1.2 Fields from General Surface Sources 19

2.5.2 Nonlinear Source Terms for SHG 20

2.5.3 SH Fields from Nonlinear Sources 21

2.5.4 Rotational SH Anisotropy 22

2.5.5 Electric Field Induced Second Harmonic (EFISH) 24

3 Experimental Setup and Methods **26**

3.1 The Ti:Sapphire Laser System 26

3.2 Laser Pulse Characterization 28

3.3 Experimental Setup for SHG 33

3.4 Experimental Setup for UV Irradiation 36

3.5 Sample Preparation and Properties 38

4 Experimental Results 40

4.1 SH Response of Virgin Si/SiO_2 . . . 41

4.2 SH Response of Pre-Irradiated Si/SiO_2 . . . 42

4.2.1 Time Dependent SH Measurements in Pre-Irradiated Si/SiO_2 . . . 42

4.2.2 SH Imaging and Scanning Electron Microscopy of Pre-Irradiated Si/SiO_2 . . . 45

4.3 SH Response of Highly Doped Si/SiO_2 . . . 47

4.4 SHG in UV Laser Pre-Irradiated Si/SiO_2 . . . 51

4.4.1 Time Dependent SH Response of UV Laser Pre-Irradiated Si/SiO_2 51

4.4.2 SH Imaging of UV Laser Pre-Irradiated Spots . . . 53

5 Discussion 56

5.1 SH Signal Evolution in Virgin Si/SiO_2 . . . 56

5.2 SH Signal Evolution in Pre-Irradiated Si/SiO_2 . . . 60

5.3 Deconvolution of e^- and h^+ EFISH Contributions . . . 63

5.4 Relaxation during Dark Periods . . . 64

5.5 SH Signal Evolution in Highly Doped Si/SiO_2 . . . 67

5.5.1 Doping Related Ionization of Interface Defect States . . . 67

5.5.2 Photoinduced Charge Carrier Screening . . . 73

5.6 UV Laser Induced Sample Modifications . . . 75

5.6.1 Time Dependent SHG in UV Laser Pre-Irradiated Si/SiO_2 . . . 75

5.6.2 SH Imaging of UV Laser Pre-Irradiated Spots . . . 76

5.6.2.1 Fluence Dependence of the UV Modification Process . 77

5.6.2.2 Accumulation of UV Modifications at Low Laser Fluence 78

Summary and Conclusions 80

Outlook 83

Bibliography 85

Introduction

Modern electronic devices are present in our ervery day lives. Particularly in the fields of data recording, processing and storage, optoelectronics as well as sensor technology enormous developments and improvements have been achieved over the last decades. They have led to unseen growth numbers in the communication and entertainment industries as well as in the information technology sector. Popular examples are cell phones, CD and DVD players, flat panel displays, flash memory cards, digital cameras, and laptop computers.

The ever increasing demand for faster, smaller, more reliable, and less power consuming electronics requires growing device integration densities in metal-oxide-semiconductor (MOS) technology. The miniaturization of logic devices, however, is reaching its physical limits. On the nanometer (nm) and Ångstrom (Å) length scales not only quantum effects begin to influence the functionality of electronic devices, but particularly surfaces and interfaces play an increasingly important role. In modern and future MOS field effect transistors (MOSFET) using ultrathin gate oxides, for example, the morphology of the oxide-semiconductor interface as well as the structure of the thin oxide layers stongly influence the performance as well as the aging characteristics of the device.

A profound physical understanding of the structural, optical as well as electronic properties of the employed nano-scale material structures is therefore of great interest, especially since surfaces and interfaces exhibit properties and a behaviour that are distinctly different from those of the adjacent bulk materials. The related physical challenges and questions have stimulated the development of sensitive diagnostic techniques particularly suitable to access surface and interface properties. Optical second harmonic generation (SHG) stands out among them as a remote and non-destructive tool with *in situ* capability and specific interface sensitivity. SHG was predicted by Göppert-Mayer in 1931 [1]. Since the optical nonlinearity is several orders of magnitude weaker than the linear optical response of most media, the experimental discovery of SHG by Franken *et al.* [2] occurred only 30 years later after the development of lasers, which have provided the light intensities necessary for efficient SHG. Theoretical frameworks to describe SHG from surfaces and interfaces were developped by Bloembergen *et al.* [3, 4] around the same time and especially since the advances in ultrafast laser technology over the last ten to fifteen years SHG has matured into a powerful and versatile probing technique for the study of a variety of surfaces and interfaces [5, 6].

Since SHG is a photon based technique and therefore non-intrusive, it is suitable to study buried solid-solid interfaces which are not accessible by other techniques. Especially, in the case of centrosymmetric crystalline materials, which show a structural inversion symmetry, SHG proves to be uniquely surface or interface sensitive, since the SHG contribution from the bulk material is parity forbidden within the electric dipole approximation [7]. The second harmonic (SH) signal generated in reflection from centrosymmetric structures, first experimentally observed by Brown *et al.* in 1965 [8], arises from atomically thin surface or interface layers, where the bulk symmetry is broken due to the rearrangement of atoms at the surface or due to the interface specific bonding configurations.

A very prominent example for a solid-solid boundary is the $\mathrm{Si/SiO_2}$ interface. It plays a technologically outstanding role and is the most widely used system in modern electronic MOS devices. Despite its extensive research history over the last 30 years [9] there is still a number of unresolved fundamental problems concerning dielectric growth and microstructure, particularly in the increasingly important field of ultrathin (< 5 nm) oxide layers. A detailed microscopic understanding of a variety of mechanisms such as oxide leakage, charge trapping at the interface, defect creation, time dependent break down or hot electron effects has yet to emerge [5, 10].

Apart from the technological issues and open questions $\mathrm{Si/SiO_2}$ is an interesting material system from the viewpoint of basic solid state physics. It represents the boundary between a centrosymmetric crystalline (Si) and an amorphous ($\mathrm{SiO_2}$) solid. It is hence a model system to study the structural transition between these two phases. The optical and especially nonlinear optical properties of the Ångstrom scale transition region (suboxide) between Si and $\mathrm{SiO_2}$ differ from those of the adjacent bulk phases. SHG as an interface sensitive non-contact optical probe plays a key role in the study of such boundary transitions [11]. Furthermore, $\mathrm{Si/SiO_2}$ serves as a test system for numerical calculations of the structural and optical properties of solid-solid boundaries [12].

The following chapter gives a brief overview over the extensive research history of the $\mathrm{Si/SiO_2}$ interface, the main focus lying on the accomplishments achieved by the SHG method. Indicating some interesting unresolved issues regarding the dynamics of charge carriers and particularly their trapping as well as trap generation at the $\mathrm{Si/SiO_2}$ interface, the problem statement of this dissertation is defined and put into perspective.

Chapter 1

State of Research

A large variety of methods has been employed to investigate the properties of the $\mathrm{Si/SiO_2}$ interface like electrical measurements [13], X-ray techniques [14], bombardment techniques [15, 16], electron spin resonance measurements [17, 18], scanning electron microscopy (SEM) [19], ballistic electron emission microscopy (BEEM) [20], tunneling microscopy [21] as well as various types of optical methods. Among the latter SHG has become a widely recognized technique particularly due to its unique atomic scale surface sensitivity in combination with its non-invasive access to buried solid-solid interfaces. In the following paragraphs a brief overview is given over important SHG work with many of the investigations and issues still being very active fields of current research.

The SH intensity originating from a Si surface was found to depend on the angle of rotation around the surface normal (rotational SH anisotropy) [22–24]. This behaviour is directly related to the structural symmetry of the surface and indicates its crystalline orientation (e.g. Si(100) or Si(111)) [25, 26]. The detailed theoretical description of SHG in reflection from cubic centrosymmetric media and the related symmetry considerations were mainly developped by Sipe, Shen, Guyot-Sionnest, Lüpke, Bottomley, van Driel, Marowsky, Felderhof, Liebsch, and coworkers [26–41].
Apart from the symmetry analysis of silicon surfaces, SHG has been used for the $in\ situ$ study of the oxidation mechanisms of silicon surfaces and the formation dynamics of $\mathrm{SiO_2}$ [42–44]. Real time monitoring of the oxide formation and its mechanisms on Si(111)-7×7 provides a representative example [43]. The SHG efficiency depends on the oxide thickness and has been determined for 2 to 300 nm thickness. Thickness dependent SH intensity oscillations observed in the s-polarized SH response of $\mathrm{Si/SiO_2}$ under p-polarized excitation can well be described by a model taking into account multiple internal reflections of the SH radiation [45]. However the thickness dependence of the p-polarized SH response shows strong deviations from the proposed multiple reflection model and can be explained using quantum electrodynamics [46]. Apart from the oxidation of silicon, SHG has been used in recent years to monitor the progress of a variety of surface chemical reactions at the $\mathrm{Si/SiO_2}$ interface and H-terminated silicon surfaces [47–49].

Thin $\mathrm{SiO_2}$ layers prepared on Si substrates are typically amorphous without well defined stoichiometry. Particularly the microscopic structure of the interfacial suboxide regions ($\mathrm{SiO_x}, \mathrm{x} < 2$) depends on the preparation technique, such as native, thermal or plasma oxidation, wet chemical processing or annealing. SHG measurements have shown to reflect the history as well as differences in the preparation methods of $\mathrm{Si/SiO_2}$ [50–59]. For instance, in correlation with atomic force microscopy (AFM) and X-ray scattering rotational SH anisotropy measurements in $\mathrm{Si/SiO_2}$ samples prepared with systematically varied interfacial microroughness have demonstrated SHG to be a rapid and non-contact tool to measure Ångstrom level interface roughness [60, 61], a critically important issue in the fabrication of electronic devices using ultrathin oxides.

Spectroscopic SHG studies have revealed different types of resonances in the SH spectra recorded in $\mathrm{Si/SiO_2}$ using tunable laser sources. Some of these resonances originate from a variety of interface specific electronic transitions. Strong resonances with energies between 3.6 and 3.8 eV, for instance, are attributed to Si interband transitions at the $\mathrm{Si(100)/SiO_2}$ interface which have no equivalent in the bulk of crystalline silicon [62]. Furthermore, strain effects at the $\mathrm{Si/SiO_2}$ interface and the related influence on the interfacial bonding configurations are accessible by spectroscopic SHG. Stress at the $\mathrm{Si/SiO_2}$ interface can originate from the difference in the thermal expansion coefficients of the silicon substrate and the oxide layer and from the structural mismatch at the interface. A strong resonance band at 3.3 eV photon energy is attributed to direct transitions between valence and conduction band states in only a few monolayers of strained silicon near the $\mathrm{Si/SiO_2}$ interface [63]. Redshifts of the interband critical points E_0' and E_1 in the SH spectra of $\mathrm{Si/SiO_2}$ by 40 and 70 meV compared with the bulk silicon values have been observed and are unambiguously attributed to strain [64].

Interface defects, which are due to deviations from the perfect saturation of dangling bonds at the interface, play a key role in interfacial charge trapping. They are believed to be mainly located at edges. Rotational SH anisotropy measurements have been performed to investigate the influence of atomic scale steps on the SH response from the buried $\mathrm{Si/SiO_2}$ interface [65]. Particularly, oxidized vicinal Si(111) substrates have been subject to detailed studies [45, 50–52, 66, 67]. One-fold and three-fold symmetry contributions to the rotational SH anisotropy can be related to steps and terraces, respectively [35, 45]. A pronounced influence of the offcut angle with respect to the (111) surface orientation on the rotational SH anisotropy pattern has been observed and explained in terms of oriented Si-O bonds located at step edges [45]. Changes in the relative phase between step and terrace related contributions to the rotational SH anisotropy have been reported for annealing temperatures above 900 °C and are explained by a modification of atomic bonding configurations at the interfacial steps [50–52]. A complete understanding of the microscopic structure of the bonding configurations at the $\mathrm{Si/SiO_2}$ interface is yet elusive and still subject to intense research, particularly due to the important implications in the field of MOS device fabrication [11, 68–74].

The focus of this dissertation lies on time dependent electric field induced SHG experiments in $\mathrm{Si/SiO_2}$ and the analysis thereof. Therefore, the following paragraphs provide a more detailed summary of current accomplishments concerning electric field induced second harmonic (EFISH) generation.

Early after the experimental discovery of SHG it was recognized that the nonlinear surface or interface properties of centrosymmetric media are strongly affected by electric fields [75]. The first electric field induced SHG experiments at the $\mathrm{Si/SiO_2}$ interface in MOS structures were performed by Aktsipetrov $et\ al.$ in the mid 1990's [76], who applied external voltages between the Si substrate and the metallic electrode coating the $\mathrm{SiO_2}$ layer. The amplitudes of the measured rotational SH anisotropy patterns showed a clear dependence on the bias voltage.
In 1995 Mihaychuk $et\ al.$ reported on a surprising time dependent increase on a time scale of several seconds in the SH intensity generated in native $\mathrm{Si/SiO_2}$ upon irradiation by near infrared ($\lambda = 770$ nm) femtosecond (~ 110 fs) laser pulses at a repetition rate of 76 MHz [77]. This increase occured without an externally applied voltage and clearly appeared to be a photoinduced effect. The ultrathin native $\mathrm{SiO_2}$ layer is transparent for the applied near infrared (NIR) radiation, because of its large bandgap of 8.9 eV. Electronic phenomena in bulk silicon are unlikely to induce the observed SH increase, since the photogenerated carrier densities are too low ($< 10^{18}\ \mathrm{cm^{-3}}$). Furthermore, the bulk carrier recombination times are $< 10^{-3}$ s. Following these considerations Mihaychuk $et\ al.$ tentatively attributed the observed SH increase on a time scale of several seconds to a photoinduced charge transfer process across the $\mathrm{Si/SiO_2}$ interface. Hot electrons generated by multi-photon excitation in Si are injected from silicon into the $\mathrm{SiO_2}$ layer and subsequently trapped. The resulting charge separation yields an interfacial electric field, which reaches magnitudes > 10^4 V/m sufficient to induce measurable changes in the interfacial SH response. The time dependent EFISH increase reflects the dynamics of the charge separation process across the $\mathrm{Si/SiO_2}$ interface and is a direct measure for the transient interfacial charge density.
In subsequent studies by the same group (van Driel) it was found that EFISH due to negative surface charging via internal photoemission is particularly pronounced in ultrathin oxides and that oxygen serves as a catalyst for electron trapping at the $\mathrm{SiO_2/air}$ interface [78]. Furthermore, a universal mechanism for gas adsorption and electron trapping on oxidized silicon was proposed based on an electrostatic model involving monopole (electron) - dipole (gas) coupling. It suits to explain the enhancement of photoinduced surface

charging in the presence of ambient oxygen [79]. Complementary SHG and multiphoton photoemission (MPPE) measurements recorded with Si/SiO_2 samples exposed to oxygen in a gas chamber show residual electron trapping in the SiO_2 layers after evacuation of the chamber [80] indicating oxygen independent trapping mechanisms.
In a number of recent studies different groups investigated the trapping of charge at the Si/SiO_2 interface employing EFISH measurements. Detailed EFISH studies in Si/SiO_2 based MOS structures were performed by the groups of Aktsipetrov, Downer, Kurz and Rasing investigating, for instance, the role of the spatial charge distribution at the interface, the influence of the oxide thickness or charge carrier induced screening effects on EFISH as well as trapping of tunneled charge carriers near the Si/SiO_2 interface [81–89]. Tolk's group recently employed EFISH measurements to determine the energy offsets between the silicon and SiO_2 [90] conduction bands and to characterize X-ray radiation damage in Si/SiO_2 [91]. Fang *et al.* studied different types of charge trap sites at the Si/SiO_2 interface using EFISH generation [92, 93] and Reider's group reported on photoinduced trap creation in Si/SiO_2 under NIR femtosecond irradiation [94, 95]. Surface charging of Si/SiO_2 under electron bombardment was monitored using SHG by van Driel's group [96] and Mitchell *et al.* demonstrated the effect of photogenerated charge carriers on the EFISH response of oxidized silicon electrodes in an electrochemical cell [97]. The active control of charge trapping in Si/SiO_2 by chemical modifications involving self assembled monolayers chemically bound to the SiO_2 surface was investigated by Fomenko *et al.* using SHG [98].

The bulk of the EFISH studies concerned with charge trapping mechanisms in the Si/SiO_2 system is focused on the photoinduced electron effects. The literature on the important role of holes is, however, sparse. Wang *et al.* recently reported on a surprising enhancement of the SH intensity recorded in Si/SiO_2 after the interruption of the incident femtosecond irradiation for approximately 100 s. This effect was only observed for oxides exceeding 40 Å thickness and attributed to the injection of holes into the SiO_2 layers under irradiation. Hole relaxation into silicon under dark conditions is leading to an enhanced residual interfacial electric field, since electrons are suggested to remain trapped in the SiO_2 layers [99]. This interpretation was questioned by the authors themselves in a later study [100], which dealt with time dependent EFISH experiments in zirconium modified $Si/(ZrO_2)_x(SiO_2)_x$ interfaces in comparison with thermally grown Si/SiO_2. In a very recent study Fomenko *et al.* performed SHG experiments with Si/SiO_2 pre-irradiated with UV light of 4.9 and 6.7 eV photon energies provided by a low pressure mercury lamp [126]. The authors observe a characteristic change in the time dependent SH response of UV pre-irradiated Si/SiO_2 which is attributed to the trapping of holes in SiO_2.

It is the aim of this dissertation to present novel insight into some aspects of the photoinduced charge carrier dynamics at the native $\mathrm{Si/SiO_2}$ interface. Particular emphasis lies on the so far sparsely investigated role of holes in the interfacial EFISH response. Some interesting novel phenomena regarding hole injection in $\mathrm{SiO_2}$, hole trap generation as well as relaxation are revealed [101, 102]. In addition, novel time dependent EFISH experiments in substantially doped $\mathrm{Si/SiO_2}$ samples are performed in order to study the doping induced charging of electrically active interface states. Furthermore, SHG is employed as a tool to study modification processes in $\mathrm{Si/SiO_2}$ samples induced by pulsed UV irradiation of 4.03 eV photon energy provided by an excimer laser source.

Overall, this work delivers some novel contributions to a more profound understanding of the basic physical mechanisms involved in interfacial charge carrier dynamics and trapping as well as defect generation. Apart from the relevance in basic solid state physics dealing with buried solid-solid interfaces, the presented results and interpretations stand in the context of the technologically important research concerned with $\mathrm{Si/SiO_2}$ systems using ultrathin oxide layers, which are becoming increasingly important.

Chapter 2

Theoretical Background

This chapter gives a brief overview over the classical theory, which describes the interaction of ultrashort light pulses with dielectric media leading to nonlinear optical effects. In particular the theoretical description of optical second harmonic generation is presented. Special emphasis lies on the phenomenological theory for SHG from centrosymmetric media in a reflection geometry.

2.1 Maxwell's Equations

In general, the propagation of electromagnetic waves in matter is classically described by Maxwell's equations (SI units):

$$\vec{\nabla} \cdot \vec{D} = \varrho \tag{2.1}$$

$$\vec{\nabla} \cdot \vec{B} = 0 \tag{2.2}$$

$$\vec{\nabla} \times \vec{E} = -\frac{\partial}{\partial t}\vec{B} \tag{2.3}$$

$$\vec{\nabla} \times \vec{H} = \frac{\partial}{\partial t}\vec{D} + \vec{j} \tag{2.4}$$

The case is considered, in which no free charge carriers are present in the medium $(\varrho = 0)$, the currents are neglegible $(\vec{j} = 0)$ and the medium is non-magnetic $(\vec{B} = \mu_0 \vec{H})$. With these assumptions Eqs. 2.1-2.4 can be summarized yielding the following wave equation:

$$\triangle \vec{E} = \mu_0 \frac{\partial^2}{\partial t^2}\vec{D} \tag{2.5}$$

The dielectric field $\vec{D}$ is related to the vacuum electric field $\vec{E}$ as follows:

$$\vec{D} = \epsilon_0 \vec{E} + \vec{P} \tag{2.6}$$

Here $\vec{P}$ is the polarization, which represents the response of the medium to the incident electric field. Each atom in the medium experiences an electric field induced dipole moment. The sum of all atomic dipole moments results in the macroscopic polarization $\vec{P}$ of the medium. For electric field amplitudes, which are small compared to the inter-atomic fields ($\ll$ 1V/Å = 10^8 V/cm), the polarization $\vec{P}$ follows a linear function of the electric field $\vec{E}$. In this case the atoms are approximated by harmonic oscillators (Lorentz model).

2.2 Nonlinear Polarization

In the general case of large electric field amplitudes ($\geq 10^8$ V/cm) the above mentioned harmonic approximation is no longer valid and the electrons displaced by the electric field will rather follow the curve of a realistic inter-atomic potential (see Fig. 2.1).

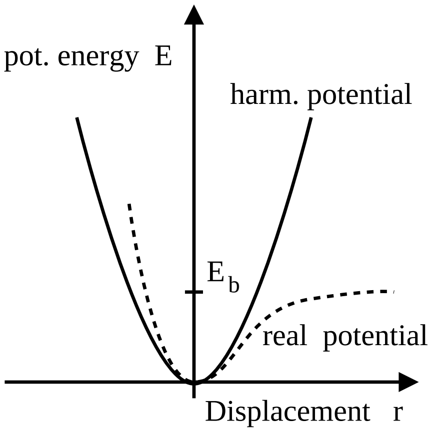

FIGURE 2.1: Comparison of ideal harmonic potential (Lorentz model) with typical realistic inter-atomic potential; E_b: binding energy.

Therefore, the polarization $\vec{P}$ is in general expanded in terms of higher powers of the electric field amplitude. The i$^{\text{th}}$ component P_i of the polarization $\vec{P}$ can then be written as:

$$P_i = \epsilon_0 \left(\sum_j \chi_{ij}^{(1)} E_j + \sum_{jk} \chi_{ijk}^{(2)} E_j E_k + \sum_{jkl} \chi_{ijkl}^{(3)} E_j E_k E_l + \dots \right) \tag{2.7}$$

The expansion coefficients $\chi^{(n)}$ are tensors of rank n+1 and are called the n$^{\text{th}}$ order optical susceptibilities. When summarizing the quadratic and higher terms in Eq. 2.7, the polarization $\vec{P}$ can be written as the sum of the linear $\vec{P}^{(1)}$ and nonlinear contributions $\vec{P}^{NL}$:

$$\vec{P} = \vec{P}^{(1)} + \vec{P}^{NL} = \epsilon_0 \chi^{(1)} \cdot \vec{E} + \vec{P}^{NL} \tag{2.8}$$

The dielectric field $\vec{D}$ can then be written as:

$$\vec{D} = \epsilon_0 \vec{E} + \vec{P} = \epsilon_0 \vec{E} + \vec{P}^{(1)} + \vec{P}^{NL} = \epsilon_0 (1 + \chi^{(1)}) \cdot \vec{E} + \vec{P}^{NL} = \epsilon_0 \epsilon^{(1)} \cdot \vec{E} + \vec{P}^{NL} \quad (2.9)$$

Here $\epsilon^{(1)} \equiv 1 + \chi^{(1)}$ is the first order dielectric tensor.

In the special case of isotropic media, $\chi^{(1)}$ and hence $\epsilon^{(1)}$ is reduced to a scalar and can be related to the refractive index n of the medium.

$$\epsilon^{(1)} = 1 + \chi^{(1)} = (n + i\kappa)^2 \quad (2.10)$$

κ describes the linear absorption and is related to the more commonly used absorption coefficient α via the equation $\alpha = 2\kappa\omega/c$.

2.3 Nonlinear Wave Equation

When Eqs. 2.8 and 2.9 are inserted in the above wave equation (2.5), the following equation is obtained:

$$\triangle \vec{E} - \frac{\epsilon^{(1)}}{c^2} \frac{\partial^2}{\partial t^2} \vec{E} = \frac{\partial^2}{\partial t^2} \mu_0 \vec{P}^{NL} \quad (2.11)$$

Eq. 2.11 respresents the nonlinear wave equation for anisotropic, dispersive and lossless media. It forms the basis for the theoretical description of all nonlinear optical effects in dielectric media.

In the following, the nonlinear wave equation 2.11, which is a second order differential equation, will be linearized employing the so-called slowly varying envelope approximation (SVEA). For the general case of dispersive media each frequency component of the field must be considered separately. Thus, the electric field vector $\vec{E}(z,t)$ as well as the nonlinear polarization vector $\vec{P}^{NL}(z,t)$ are represented by the sum over n positive frequency components ω_n:

$$\vec{E}(z,t) = \sum_n E_n(z,t) e^{i(k_n z - \omega_n t)} + c.c. \quad (2.12)$$

$$\vec{P}^{NL}(z,t) = \sum_n P_n^{NL}(z,t) e^{i(k_n z - \omega_n t)} + c.c. \quad (2.13)$$

The propagation direction is chosen to be along the z-axis and k_n is the respective wave vector.

In the visible frequency range, which is relevant for the experiments in this study, $\omega_n \approx 10^{15}\ \mathrm{s}^{-1}$ holds for the fundamental carrier frequencies. The temporal variation of the electric field envelope $E_n(z,t)$ takes place on a time scale, which is approximately two orders of magnitude larger for the femtosecond laser pulses employed here ($\tau \approx 10^{-13}$ s). Therefore the following approximations are applicable for the electric field envelopes:

$$\frac{\partial^2}{\partial t^2}E_n \ll \omega_n \frac{\partial}{\partial t}E_n \tag{2.14}$$

$$\frac{\partial^2}{\partial z^2}E_n \ll k_n \frac{\partial}{\partial z}E_n \tag{2.15}$$

Furthermore, it is assumed that for the nonlinear polarization, where higher harmonics are considered as carrier waves, also the first order derivatives of the envelope functions are neglegible [103]:

$$\frac{\partial^2}{\partial t^2}P_n^{NL} \ll \omega_n \frac{\partial}{\partial t}P_n^{NL} \ll \omega_n^2 P_n^{NL} \tag{2.16}$$

When Eqs. 2.12 and 2.13 are inserted into the nonlinear wave equation 2.11 and the respective derivatives are omitted according to Eqs. 2.14-2.16, it is found that for each frequency component ω_n the following first order differential equation in the amplitude functions must be satisfied:

$$\left(\frac{\partial}{\partial z} + \frac{n_{\omega_n}}{c}\frac{\partial}{\partial t}\right) E_n(z,t) = i\frac{\omega_n}{2\epsilon_0 n_{\omega_n} c} P_n^{NL}(z,t)e^{-ik_n z} \tag{2.17}$$

Consequently, Eq. 2.17 represents the linearized form (SVEA) of the general nonlinear wave equation 2.11 and with the above mentioned approximations describes the electric field in the medium due to the induced nonlinear polarization.

The intensity of the light pulses employed in the experiment determines, which terms of the nonlinear polarization $P_n^{NL}(z,t)$ are to be included in Eq. 2.17. The larger the involved electric fields, the more relevant become higher order terms $\chi^{(n)}$.

Examples for $\chi^{(2)}$-effects, which are also called 3-photon processes, are sum and difference frequency generation, particularly second harmonic generation as a special case thereof, as well as parametric amplification processes.

Frequency tripling, self-phase modulation, self-focussing as well as four wave mixing are $\chi^{(3)}$ or 4-photon effects.

In this work optical second harmonic generation (SHG) is employed as a probe to investigate crystalline material systems. Therefore, the properties of the second order susceptibility tensor $\chi^{(2)}$, are in the following discussed in further detail.

2.4 Second Order Susceptibility Tensor

2.4.1 Definition

As seen in Eq. 2.7, the second order optical susceptibility $\chi^{(2)}$ relates the amplitude of the second order nonlinear polarization and the electric field amplitudes. The second order nonlinear polarization is generally defined as:

$$P_i^{(2)} = \epsilon_0 \left(\sum_{jk} \chi_{ijk}^{(2)} E_j E_k \right) \tag{2.18}$$

$\chi^{(2)}$ forms a tensor of rank three and in general consists of 27 cartesian components. As shown in detail in reference [104], the full description of the mutual interaction of three waves of frequencies ω_1, ω_2 and $\omega_3 = \omega_1 + \omega_2$ requires to determine 12 tensors of rank three, which results in a total of 324 different complex components. Fortunately, symmetry considerations yield relations between various components of $\chi^{(2)}$ and hence drastically reduce the number of independent entries.

2.4.2 Symmetry Properties

The general symmetry properties of the second order susceptibility tensor $\chi^{(2)}$ include:

Time reversal symmetry:

$$\chi_{ijk}^{(2)}(-\omega_n - \omega_m, -\omega_n, -\omega_m) = \chi_{ijk}^{(2)}(\omega_n + \omega_m, \omega_n, \omega_m)^* = 0 \tag{2.19}$$

Intrinsic permutation symmetry:

$$\chi_{ijk}^{(2)}(\omega_n + \omega_m, \omega_n, \omega_m) = \chi_{ikj}^{(2)}(\omega_n + \omega_m, \omega_m, \omega_n) \tag{2.20}$$

Full permutation symmetry:

$$\chi_{ijk}^{(2)}(\omega_n + \omega_m, \omega_n, \omega_m) = \chi_{jki}^{(2)}(\omega_m - \omega_n, \omega_m, -\omega_n) \tag{2.21}$$

The reality of physical fields reduces the number of independent tensor elements to 162. The intrinsic permutation symmetry of $\chi^{(2)}$ further decreases the number to 81 parameters and full permutation symmetry leads to only 27 of these entries. Under most experimental conditions the frequency of the optical field is much smaller than the lowest resonance of the material system. In this case the medium is practically lossless and the nonlinear susceptibility is essentially frequency independent. Under these assumptions the full permutation symmetry described in Eq. 2.21 transforms into the so-called Kleinmann symmetry condition [7, 104], which allows for index permutation without simultaneous frequency permutation:

$$\begin{aligned}\chi^{(2)}_{ijk}(\omega_n+\omega_m,\omega_n,\omega_m) &= \chi^{(2)}_{jki}(\omega_n+\omega_m,\omega_n,\omega_m) = \chi^{(2)}_{kij}(\omega_n+\omega_m,\omega_n,\omega_m)\\ &= \chi^{(2)}_{ikj}(\omega_n+\omega_m,\omega_n,\omega_m) = \chi^{(2)}_{jik}(\omega_n+\omega_m,\omega_n,\omega_m)\\ &= \chi^{(2)}_{kji}(\omega_n+\omega_m,\omega_n,\omega_m)\end{aligned} \tag{2.22}$$

In addition to the general symmetry properties of $\chi^{(2)}$ given in Eqs. 2.19 - 2.21 and the Kleinmann symmetry condition (Eq. 2.22), crystalline media can be divided in 32 crystal classes [105], which show specific spatial symmetry properties. These crystalline symmetries can reduce the number of independent entries of $\chi^{(2)}$ even further.

One important symmetry property is inversion symmetry, which occurs in 11 of the 32 crystal classes. Crystalline structures with this property are called centrosymmetric and it can be shown that $\chi^{(2)}$ vanishes for these material systems [104]. The form of $\chi^{(2)}$ can be determined for structures of each particular crystal class. Such calculations were originally performed by Butcher [106] and the results are summarized in [104].

2.4.3 Contracted Notation

In the case of lossless media, where the Kleinmann symmetry condition holds, the second order susceptibility tensor is often written in contracted form:

$$d_{il} = \frac{1}{2}\chi^{(2)}_{(ijk)} \tag{2.23}$$

Here it is assumed that $\chi^{(2)}_{ijk}$ is symmetric in the last two indices, which is generally satisfied in the case of second harmonic generation, since $\omega_n \equiv \omega_m$ in Eq. 2.21. The number of independent parameters is hence reduced to 18. The indices j and k are summarized as follows:

$$\begin{array}{cccccccc} jk: & 11 & 22 & 33 & 23,32 & 31,13 & 12,21 \\ l: & 1 & 2 & 3 & 4 & 5 & 6 \end{array} \tag{2.24}$$

The second order nonlinear polarization can then be written as:

$$\begin{bmatrix} P_x(2\omega) \\ P_y(2\omega) \\ P_z(2\omega) \end{bmatrix} = 2\epsilon_0 \begin{bmatrix} d_{11} & d_{12} & d_{13} & d_{14} & d_{15} & d_{16} \\ d_{21} & d_{22} & d_{23} & d_{24} & d_{25} & d_{26} \\ d_{31} & d_{32} & d_{33} & d_{34} & d_{35} & d_{36} \end{bmatrix} \begin{bmatrix} E_x^2(\omega) \\ E_y^2(\omega) \\ E_z^2(\omega) \\ 2E_y(\omega)E_z(\omega) \\ 2E_x(\omega)E_z(\omega) \\ 2E_x(\omega)E_y(\omega) \end{bmatrix} \tag{2.25}$$

If the Kleinmann symmetry condition 2.22 is explicitly applied, it is found that only 10 of the 18 elements of d_{il} are independent entries.

If the symmetry of crystal surfaces is considered, the number of independent tensor elements reduces further and for the low index cubic crystal faces (001) and (111) and (110) only the following non-zero entries in the matrix in Eq. 2.25 remain [35]:

(001) face:

$$d_{15} = d_{24}, d_{31} = d_{32}, d_{33} \tag{2.26}$$

(111) face:

$$d_{11} = -d_{12} = -d_{26}, d_{15} = d_{24}, d_{31} = d_{32}, d_{33} \tag{2.27}$$

(110) face:

$$d_{15}, d_{24}, d_{31}, d_{32}, d_{33} \tag{2.28}$$

where the d_{ij} are different for the different faces.

2.5 SHG in Reflection from Centrosymmetric Media

In the following the phenomenological description of SHG from cubic centrosymmetric media in a reflection geometry is outlined, as it is applicable in the experiments performed in this study.

Most calculations in surface optics can be divided in two distinct parts. The first part deals with the determination of a source of electromagnetic radiation, which has microscopic origin, whereas the second part involves the computation of the actual electric fields generated by this source in the geometry of interest.

2.5.1 Fields from General Bulk and Surface Sources

In order to calculate the generated electric fields originating from a general source of radiation a Green's function approach is applicable [26]. This approach involves an integral over the source and can hence be used to calculate the generated electric fields for any source distribution.

First, the reflection geometry as shown in Fig. 2.2 is considered, as it is used in the here performed experiments.

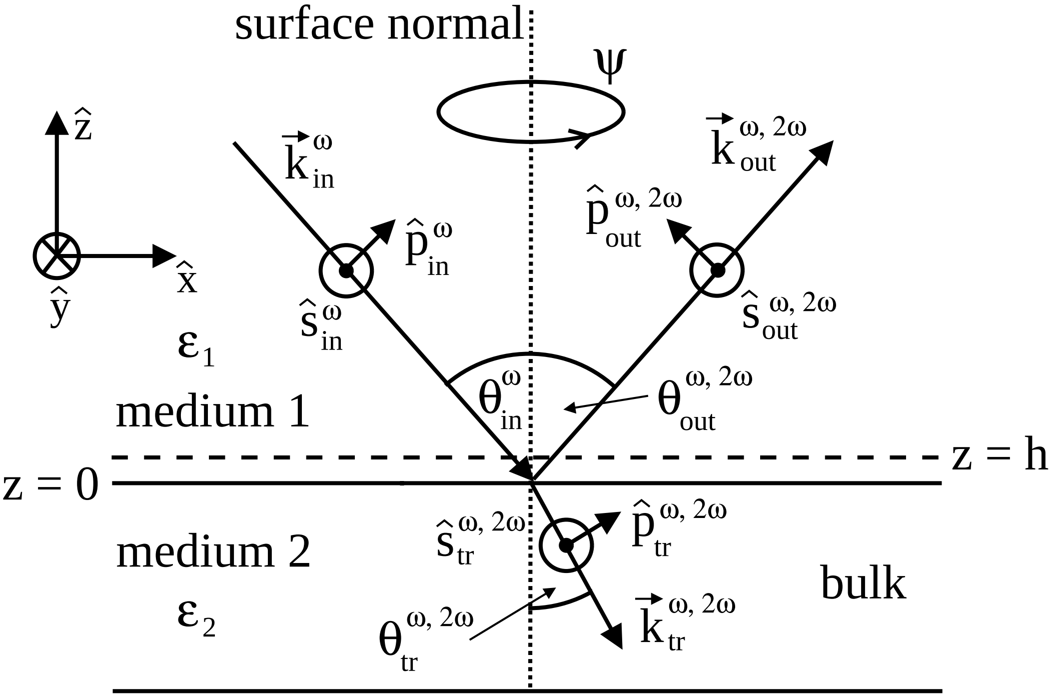

FIGURE 2.2: Geometry of SHG in reflection from an interface at $z = 0$. Polarization dipole sheet located at $z = h$.

Medium 1 can either be air, vacuum or any arbitrary optically linear dielectric medium transparent at the frequencies ω and 2ω. Medium 2 is the centrosymmetric material under investigation. A fundamental plane wave of frequency ω, represented by the wave vector $\vec{k}^{\omega}_{in}$ is incident on the interface ($z = 0$) under the angle θ^{ω}_{in}. It is partially reflected at the interface under the angle $\theta^{\omega}_{out} = \theta^{\omega}_{in}$ and partially transmitted into medium 2 under the angle θ^{ω}_{tr} as denoted by $\vec{k}^{\omega}_{out}$ and $\vec{k}^{\omega}_{tr}$, respectively. The SH waves are represented by the wave vectors $\vec{k}^{2\omega}_{out}$ and $\vec{k}^{2\omega}_{tr}$ and the angles $\theta^{2\omega}_{out}$ and $\theta^{2\omega}_{tr}$. All waves are propagating in the $x - z$ plane. The polarization directions of the fundamental and SH waves are defined by $\hat{p}^{\omega,2\omega}_{in,tr,out}$ and $\hat{s}^{\omega,2\omega}_{in,tr,out}$. The wave vectors can be expressed in terms of the unit vectors $\hat{x}$, $\hat{y}$, $\hat{z}$ in Fig. 2.2 as follows:

$$\begin{aligned} &\vec{k}_{in}^{\omega} = p^{\omega}\hat{x} - q_1^{\omega}\hat{z}, \vec{k}_{out}^{\omega} = p^{\omega}\hat{x} + q_1^{\omega}\hat{z}, \vec{k}_{tr} = p^{\omega}\hat{x} - q_2^{\omega}\hat{z}, \\ &\vec{k}_{out}^{2\omega} = p^{2\omega}\hat{x} + q_1^{2\omega}\hat{z}, \vec{k}_{tr}^{2\omega} = p^{2\omega}\hat{x} - q_2^{2\omega}\hat{z} \end{aligned} \tag{2.29}$$

Here the $q_i^{\omega} = [(k_i^{\omega})^2 - (p^{\omega})^2]^{1/2}$ and $q_i^{2\omega} = [(k_i^{2\omega})^2 - (p^{2\omega})^2]^{1/2}$ are the positive z-components of the respective wave vectors in medium $i = 1, 2$, with $k_i^{\omega} = \frac{\omega}{c}\sqrt{\epsilon_i(\omega)}$ and $k_i^{2\omega} = \frac{2\omega}{c}\sqrt{\epsilon_i(2\omega)}$. p^{ω} and $p^{2\omega}$ are the x-components of the fundamental and SH waves, respectively.

In the following, the electric fields generated by general bulk and surface sources are constructed considering the above introduced reflection geometry.

2.5.1.1 Fields from General Bulk Sources

It is supposed there is a source of radiation inside the bulk of medium 2 for $z < 0$ taking the general form:

$$\vec{P}(\vec{r}) = \vec{P}(z)\exp(i\vec{\kappa}\cdot\vec{R}) \tag{2.30}$$

with a spatial variation characterized by a wave vector $\vec{\kappa}$ and $\vec{R} = (x, y)$. This form is suitable, within the plane wave approximation, for many experiments in nonlinear optics at interfaces [5]. It applies for the bulk SH contribution originating from magnetic dipole and electric quadrupole terms as defined below in Eq. 2.35.

Each sheet of polarization at a given z-position inside medium 2 produces an upward and a downward wave. The downward wave is not considered, since it propagates away from the interface and is not detected. The upward wave is partly reflected down at the interface and partly transmitted into region 1, where it is measured. The electric field of frequency ω in region 1 arising from the general source (Eq. 2.30) in medium 2 ($z < 0$) can thus be expressed as [5, 26]

$$\vec{E}(\vec{r}) = \vec{E}(z)\exp(i\vec{\kappa}\cdot\vec{R}) = \vec{E}\exp(iq_1^{\omega}z)\exp(i\vec{\kappa}\cdot\vec{R}) \tag{2.31}$$

involving the integral over the source as follows:

$$\vec{E} = 2\pi i(k_q^{\omega})^2(q_2^{\omega})^{-1}(\hat{s}^{\omega}t_{21}^{s}\hat{s}^{\omega} + \hat{p}_{1+}^{\omega}t_{21}^{p}\hat{p}_{2+}^{\omega}) \cdot \int_{-\infty}^{0} \exp(-iq_2^{\omega}z')\vec{P}(z')dz' \tag{2.32}$$

The factor $\exp(-iq_2^\omega z') = \exp[iq_2^\omega(0 - z')]$ in Eq. 2.32 describes the propagation from the position z' inside medium 2 up to the interface. The factor $\exp(iq_1^\omega z)$ in Eq. 2.31 describes the propagation from the interface up into region 1. The tensor factor $(\hat{s}^\omega t_{21}^s \hat{s}^\omega + \hat{p}_{1+}^\omega t_{21}^p \hat{p}_{2+}^\omega)$ describes the transmission of the wave from medium 2 into medium 1 and takes the relevant Fresnel factors into account. It also accounts for the usual change of the p-polarized direction upon transmission as denoted by $\hat{p}_{1+}^\omega$ and $\hat{p}_{2+}^\omega$, with $\hat{p}_{i\pm}^\omega = k_i^{-1}(p\hat{z} \mp q_i\hat{x})$. The explicit expressions for $t_{ij}^{p,s}$ are listed in Ref. [5].

It is noted that under the experimental conditions applied here, the phase matching condition [7, 104] for SHG is trivially satisfied, since the escape depth of the observed SH signal generated in $\mathrm{Si/SiO_2}$ using a reflection geometry is approximately 100 nm (section 3.5). On such length scales the wave vector mismatch between the fundamental and SH waves is neglegible.

2.5.1.2 Fields from General Surface Sources

The surface second order nonlinear response is modelled by a polarization sheet of only few atomic layers located at $z = h$ in Fig. 2.2 representing the interfacial region of broken inversion symmetry. The general source term for the polarization sheet takes the form:

$$\vec{P}(\vec{r}) = \vec{P}\delta(z - h)\exp(i\vec{\kappa} \cdot \vec{R}) \tag{2.33}$$

This term assumes a plane wave behaviour in the $x - y$ plane [$\vec{R} = (x, y)$] with wave vector $\vec{\kappa}$ and is applicable for the surface SH contribution arising from the below determined effective surface nonlinear source term (Eq. 2.38).

The electric field in region 1 for $z > h$ consists of the upward wave generated by the source as well as the upward reflection from the interface of the downward wave generated by the source. The total electric field in region 1 ($z > h$) arising from the polarization sheet represented by the general source term in Eq. 2.33 takes the form:

$$\vec{E} = 2\pi i(k_1^\omega)^2(q_1^\omega)^{-1}[\hat{s}^\omega(1 + r_{12}^s\hat{s}^\omega) + \hat{p}_{1+}^\omega(\hat{p}_{1+}^\omega + r_{12}^p\hat{p}_{1-}^\omega)] \cdot \vec{P} \tag{2.34}$$

Eq. 2.34 is usually derived by first modelling the source as a thin slab, solving for the fields in region 1 and 2 and in the thin slab employing the saltus conditions at the boundaries and finally taking the limit of the slab to a δ function [5, 108]. The tensor factor $[\hat{s}^\omega(1 + r_{12}^s\hat{s}^\omega) + \hat{p}_{1+}^\omega(\hat{p}_{1+}^\omega + r_{12}^p\hat{p}_{1-}^\omega)]$ takes the relevant Fresnel factors into account. The expressions for $r_{ij}^{p,s}$ which are listed in Ref. [5].

2.5.2 Nonlinear Source Terms for SHG

In the following the specific source terms describing the bulk and surface contributions to the SH response of centrosymmetric media in a reflection geometry are identified.

In the bulk of centrosymmetric media the second order optical susceptibility vanishes $\chi^2_{ijk} \equiv 0$ due to the inversion symmetry of the crystalline structure. Hence, the electric dipolar SH response is parity forbidden. Therefore, to lowest order only magnetic dipole and electric quadrupole terms can contribute to the nonlinear polarization of bulk centrosymmetric media. The latter involves the electric field gradient and can be written as [5, 26, 109]:

$$P_i^{2\omega} = \sum_{jkl} \epsilon_0 \chi^{(3)}_{Q_{ijkl}} E_j^\omega \nabla_k E_l^\omega \tag{2.35}$$

Eq. 2.35 represents the bulk SH source term for centrosymmetric media. For cubic crystals, such as silicon, this expression reduces to:

$$\begin{aligned} P_i^{2\omega} &= \epsilon_0(\delta - \beta - 2\gamma) E_j^\omega \nabla_j E_i^\omega + \epsilon_0 \beta E_i^\omega \nabla_j E_j^\omega + \\ &\quad \epsilon_0 \gamma \nabla_i (E_j^\omega E_j^\omega) + \epsilon_0 \zeta E_i^\omega \nabla_i E_i^\omega \end{aligned} \tag{2.36}$$

with

$$\delta = 2\chi^{(3)}_{Q_{iiii}},\ \beta = 2\chi^{(3)}_{Q_{iijj}},\ \gamma = \chi^{(3)}_{Q_{ijij}},\ \zeta = \delta - \beta - 2\gamma - 2\chi^{(3)}_{Q_{ijji}}, \tag{2.37}$$

where δ, β, γ are isotropic coefficients and ζ is anisotropic. For excitation with a single plane wave only the last two terms in Eq. 2.36 contribute [26, 109].

The surface or interface contribution to SHG from centrosymmetric media can have two origins. Firstly, close to a surface or interface the inversion symmetry of a centrosymmetric medium is broken, due to the surface or interface specific rearrangement of atoms. Therefore, an electric dipolar SH response can arise from an interfacial region with a thickness of only a few atomic layers. Secondly, there is a discontinuity in the electric field component normal to the interface, resulting in a large gradient in the normal fundamental field. Through higher order multiple terms (Eq. 2.35) this gradient can generate considerable SH contributions, for example $\nabla_z[\chi^{(3)}_{Q_{izkl}} E_k^\omega E_l^\omega]$. Both effects have been discussed in the past [26, 30–32, 107] and can be combined by the definition of an effective surface dipolar second order susceptibility $\chi^{(2)}_S$ leading to a nonlinear polarization of the form [26, 35]:

$$P_i^{2\omega} = \epsilon_0 \sum_{jk} \chi^{(2)}_{S_{ijk}} E_j^\omega E_k^\omega \delta(z - h) \tag{2.38}$$

Eq. 2.38 represents the surface SH source term for centrosymmetric media. In the geometry in Fig. 2.2 this effective dipolar SH contribution is considered to arise from a dipolar polarization sheet located approximately an atomic distance (dashed line at $z = h$) above the interface, as accounted for by the δ-function in Eq. 2.38. It represents the thin interfacial region with broken inversion symmetry and non-vanishing dipolar SH response. Here the convention $z = +h$ is used for the position of the polarization sheet, which is not essential. $z = -h$ would yield only a rescaling of the problem [5, 35].

2.5.3 SH Fields from Nonlinear Sources

The above outlined derivation, which leads to the electric fields generated by the general source terms in Eqs. 2.30 and 2.33 can now be explicitly applied to obtain the SH field in region 1 originating from the nonlinear SH source terms as identified in section 2.5.2 (Eqs. 2.35 and 2.38).

Considering the reflection geometry as shown in Fig. 2.2, the transmitted fundamental field in medium 2 can be expressed as:

$$\vec{E}_t^{\omega}(\vec{r}) = (E_i^s t_{12}^s \hat{s}^{\omega} + E_i^p t_{12}^p \hat{p}_{2-}^{\omega}) \exp[i(p^{\omega} x - q_2^{\omega} z)] \equiv \hat{e}^{\omega} |E_i^{\omega}| \exp[i(p^{\omega} x - q_2^{\omega} z)] \quad (2.39)$$

with $|E_i^{\omega}|^2 = |E_i^s|^2 + |E_i^p|^2$. For an isotropic medium 2 the bulk nonlinear polarization (Eq. 2.35) then reduces to:

$$\vec{P}^{2\omega}(z) = \gamma \exp[i(p^{2\omega} \hat{x} - q_2^{2\omega} \hat{z})] \hat{e}^{\omega} \hat{e}^{\omega} |E_i^{\omega}|^2 \exp(-i q_2^{2\omega} z) \quad (2.40)$$

Following the above outlined derivation and evaluating the integral over the source, the SH field in region 1 originating from the bulk SH contribution is obtained:

$$\vec{E}^{2\omega}(\vec{r}) = \frac{2\pi i (k_1^{2\omega})^2}{q_1^{2\omega}} \gamma \mathbf{L^1} (\hat{e}^{\omega} \hat{e}^{\omega}) |E_i^{\omega}|^2 \exp[i(p^{2\omega} x + q_1^{2\omega} z)] \quad (2.41)$$

where

$$\mathbf{L^1} = \frac{2 q_1^{2\omega}}{q_2^{2\omega}} \frac{\hat{s}^{2\omega} T_{12}^s s^{2\omega} + \hat{p}_{1+}^{2\omega} T_{12}^p p_{2+}^{2\omega}}{q_2^{2\omega} + 2 q_1^{\omega}} \cdot (q_1^{\omega} \hat{z} - p^{\omega} \hat{x}) \quad (2.42)$$

accounts for the respective Fresnel factors for the SH waves. The expressions for $T_{ij}^{p,s}$ are listed in Ref. [5].

Analogously the surface nonlinear polarization (Eq. 2.38) reduces to

$$\vec{P}^{2\omega}(\vec{r}) = \overleftrightarrow{\chi}_{S}^{(2)} \hat{e}^{\omega}\hat{e}^{\omega}|E_i^{\omega}|^2 \exp(i2p^{\omega}x)\delta(z-h) = \vec{P}\delta(z-h)\exp(i2px) \tag{2.43}$$

and the SH field in region 1 originating from the surface SH contribution is obtained:

$$\vec{E}^{2\omega}(\vec{r}) = \frac{2\pi i (k_1^{2\omega})^2}{q_1^{2\omega}} \mathbf{M^1} \cdot \vec{P} \exp[i(p^{2\omega}x + q_1^{2\omega}z)] \tag{2.44}$$

with $\mathbf{M^1} = [\hat{s}^{2\omega}](1 + R_{12}^{s})\hat{s}^{2\omega} + \hat{p}_{1+}^{2\omega}(\hat{p}_{1+}^{2\omega} + R_{12}^{p}\hat{p}_{1-}^{2\omega})]$ taking the Fresnel factors for the SH waves into account. The $R_{ij}^{p,s}$ are listed in Ref. [5].

Finally, combining the bulk and surface contributions to the generated SH field the total SH intensity can be written as:

$$I^{2\omega} = \frac{32\pi^3\omega^2}{c^3} \sec^2\theta_{in}^{\omega} |\hat{e}^{out}\left(\mathbf{L^1}\overleftrightarrow{\chi}_{Q}^{(3)} + \mathbf{M^1}\overleftrightarrow{\chi}_{S}^{(2)}\right)\hat{e}^{\omega}\hat{e}^{\omega}|^2 (I^{\omega})^2 \tag{2.45}$$

Here medium 1 is assumed to be dispersionless with $n = 1$, which implies $\theta_{out}^{2\omega} = \theta_{out}^{\omega}$. Then $(k_1^{2\omega}/q_1^{2\omega})$ = $\sec^2\theta_{in}^{\omega}$ holds with $(k_1^{2\omega})^2 = 4\omega^2/c^2$ [5]. The unit vector $\hat{e}^{out}$ denotes the polarization direction of the SH field which is chosen to be detected. It is noted that $I^{2\omega}$ is a quadratic function in I^{ω}. A general proof by Sipe *et al.* [27] states that the isotropic surface and bulk SH contributions originating from centrosymmetric media are inseparable for SHG from the general crystal face and always observed simultaneously. The following section deals with anisotropic SH contributions.

2.5.4 Rotational SH Anisotropy

The high tensorial ranks of the nonlinear susceptibilities in Eq. 2.35 and 2.38 give rise to anisotropic second harmonic generation. Hence the intensity of the emitted SH wave depends on the relative orientation between the crystal axes and the polarization directions of the fundamental beam.

To express the generated SH intensity as a function of the azimuthal angle of rotation ψ around the surface normal (Fig. 2.2), the anisotropic SHG source terms need to be transformed from the crystal coordinate system into the beam frame.
In the following the transformation of the tensor $\chi_{S_{ijk}}^{(2)}$ representing the surface contribution to the SH response expressed in the crystal coordinates into the beam frame [26, 34, 35] is briefly summarized. The transformation of $\chi_{Q_{ijkl}}^{(3)}$ can be performed analogously.

As depicted in Fig. 2.3 the relative orientations of the crystal ($\hat{e}_1$, $\hat{e}_2$, $\hat{e}_3$) and beam frames ($\hat{x}$, $\hat{y}$, $\hat{z}$) are related by multiple rotations. The $\hat{e}_i$ ($i = 1, 2, 3$) are chosen to coincide with the cubic crystal axes (100), (010) and (001), respectively. In the following, each successive rotation is denoted by an additional prime. The orientation of the general surface normal with respect to the cubic crystal axes is specified by two angles α and β. To transform $\chi^{(2)}_{S_{ijk}}$ from the crystal to the beam frame, two successive rotations are performed, first by the angle β about the $\hat{e}_3$ axis, then by the angle α about the $\hat{e}_2'$ axis.

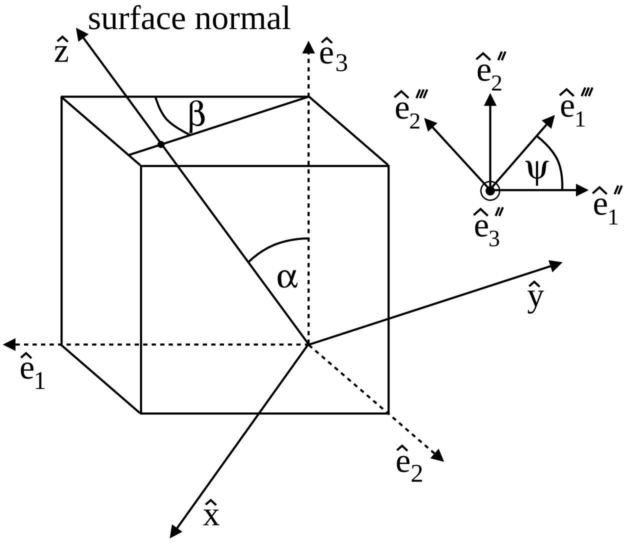

FIGURE 2.3: Diagram of the relative orientation between the crystal ($\hat{x}$, $\hat{y}$, $\hat{z}$) and beam ($\hat{e}_1$, $\hat{e}_2$, $\hat{e}_3$) coordinate systems, related by multiple rotations.

The transformation rules for $\chi^{(2)}_{S_{ijk}}$ for the two rotations are given by:

$$\chi^{(2)}_{S_{i'j'k'}} = \sum_{ijk} R_{i'i}(\beta)R_{j'j}(\beta)R_{k'k}(\beta)\chi^{(2)}_{S_{ijk}} \tag{2.46a}$$

$$\chi^{(2)}_{S_{i''j''k''}} = \sum_{i'j'k'} S_{i''i'}(\alpha)S_{j''j'}(\alpha)S_{k''k'}(\alpha)\chi^{(2)}_{S_{i'j'k'}} \tag{2.46b}$$

Here $R_{ij}(\beta)$ and $S_{ij}(\alpha)$ are rotation matrices, the explicit forms of which are given in Ref. [34].

The azimuthal rotation about the surface normal is represented by a rotation about $\hat{e}_3''$ by the angle ψ in Fig. 2.3. The transformation rule is equal to the one given in Eq. 2.46a using the rotation matrix R_{ij} with β substituted by ψ [34]. The $\hat{e}_i'''$ ($i = 1, 2, 3$) and beam frames are then coincident as indicated in the inset in Fig. 2.3. ψ is defined such that $\hat{e}_1''$ and $\hat{e}_2''$ coincide with $\hat{e}_1'''$ and $\hat{e}_2'''$ for $\psi = 0$, respectively.

Performing the above described transformations for both, the surface (Eq. 2.38) and bulk (Eq. 2.35) nonlinear source terms, with particular emphasis on the low index crystal faces (001), (111) and (110) of cubic centrosymmetric crystals (Eqs. 2.26-2.28) the following expressions are obtained for the p-polarized SH fields arising from surface and bulk terms under p-polarized excitation, which are exclusively measured in this study [35]:

$$E_{p,p}^{surf,2\omega}(\psi) \propto \left[\sum_{n=0}^{3} a_{p,p}^{n} \cos(n\psi)\right] \cdot [E_p^{\omega}]^2 \tag{2.47}$$

$$E_{p,p}^{bulk,2\omega}(\psi) \propto \left[b(p,p) + \sum_{n=0}^{4} c_{g,p}^{n}(\alpha,\beta) \cos(n\psi)\right] \cdot [E_p^{\omega}]^2 \tag{2.48}$$

Here the Fourier coefficients $a_{p,p}^n$, $b_{p,p}^n$ and $c_{p,p}^n(\alpha,\beta)$ are introduced for simplicity and combine the relevant Fresnel factors, independent tensor elements and angular functions. For further algebraic detail as well as the expressions for differently polarized SH fields it is referred to Ref. [35].

The total SH intensity as a function of ψ in the (p,p) polarization combination originating from bulk and surface source terms is then proportional to the absolute square of the sum of the bulk and surface SH fields:

$$I_{p,p}^{2\omega} \propto |E_{p,p}^{bulk,2\omega}(\psi) + E_{p,p}^{surf,2\omega}(\psi)|^2 \tag{2.49}$$

Finally, combining Eqs. 2.47, 2.48 and Eq. 2.49 the total p-polarized SH intensitity generated in reflection from cubic centrosymmetric media under p-polarized excitation shows the following dependence on the azimuthal angle ψ [33]:

$$I_{p,p}^{2\omega}(\psi) \propto |\sum_{n=0}^{4} c_n^{tot}(p,p) \cos(n\psi)|^2 \cdot (I_p^{\omega})^2 \tag{2.50}$$

where the Fourier coefficients $c_n^{tot}(p,p)$ combine the previous coefficients in Eqs. 2.47 and 2.48 for the surface and bulk contributions. It is noted that the expression in Eq. 2.50 holds for crystal faces of $C_{1\nu}$ symmetry and is applicable to the low index cubic crystal faces (100), (111) and (110).

2.5.5 Electric Field Induced Second Harmonic (EFISH)

Due to the forbidden electric dipole contribution to the SH response, centrosymmetric media are very sensitive to external pertubations, such as externally applied electric fields or internal electric fields caused by charge carrier separation processes. The SH polarization due to a quasi-static, time dependent electric field $E(t)$ (EFISH: electric field induced second harmonic) can be expressed as [76, 78, 81, 89]

$$P_i^{2\omega} = \epsilon_0 \sum_{jkl} \chi_{B_{ijkl}}^{(3)} E_j^{\omega} E_k^{\omega} E_l(t) \tag{2.51}$$

where $\chi^{(3)}_{B_{ijkl}}$ are the components of the bulk dipole allowed third order nonlinear susceptibility. Although electric field induced second harmonic generation is based on a $\chi^{(3)}$ process, it can result in a significant SH contribution, since the involved electric fields can become very large. In the specific case of the $\mathrm{Si/SiO_2}$ system charge densities $> 10^{12}\ \mathrm{cm}^{-2}$ at the interface are common and interfacial electric fields $> 10^6 \mathrm{V/m}$ can be achieved. Through Eq. 2.51 they are capable of inducing drastic changes in the SH response of $\mathrm{Si/SiO_2}$ [76, 78].

The temporal SH intensity evolution generated by photoinduced charge separation at the $\mathrm{Si/SiO_2}$ interface can be written as [78]:

$$I^{2\omega}(t) = |\chi^{(2)}_0 + \chi^{(3)}_B E(t)|^2 (I^\omega)^2 \tag{2.52}$$

Here I^ω and $I^{2\omega}(t)$ denote the intensities of the fundamental and time dependent SH waves. $\chi^{(3)}_B$ represents the dipole allowed third order nonlinear susceptibility of silicon and $\chi^{(2)}_0$ is the effective SH susceptibility arising from all other sources. $E(t)$ is the time dependent interfacial electric field, generated by photoinduced charge separation across the interface [77, 78]. It is noted that at the incident laser intensities applied here the total SH signal is governed by the EFISH component.

The equilibrium SH intensity reached upon saturation of charge carrier separation ($t \gg 1$) is a direct measure for the interfacial charge density n_c [80]

$$n_c \propto |\chi^{(2)}_{i,eff}| \propto \sqrt{I^{(2\omega)}} \tag{2.53}$$

with $\chi^{(2)}_{i,eff}$ being the combined effective photoinduced second order susceptibility, which depends on the internal electric field.

EFISH measurements probing internal electric fields, and thus giving access to interfacial charge carrier dynamics, lie in the focus of this dissertation and form the majority of the here presented experiments.

Chapter 3

Experimental Setup and Methods

The following chapter describes the commercial Titanium:sapphire laser source employed in this work as well as explains its working principle and the underlying physical phenomena. In order to determine the characteristic laser pulse parameters essential for the quantitative evaluation of the SHG experiments, a custom-built laser pulse diagnostics setup was implemented during the course of this work and is described below. Most importantly, the experimental setup for SHG in reflection is explained, which was designed and constructed as part of this work and used to perform all SH measurements presented in this dissertation. Details about the preparation of the $\mathrm{Si/SiO_2}$ samples as well as their properties are given.

3.1 The Ti:Sapphire Laser System

The material system most commonly used as laser gain medium to generate ultrashort laser pulses is titanium doped sapphire ($\mathrm{Ti{:}Al_2O_3}$). Its fluorescence band is strongly broadened due to lattice vibrations (phonons) and the laser gain line shape covers the wavelength range from 660 to 1180 nm with a maximum at 795 nm [110]. Since the pulse duration and the spectral pulse width are related by the Fourier theorem and indirectly proportional, the corresponding theoretical limit for the minimum laser pulse duration amounts to 4 fs. Sub-two-cycle pulses of 5.4 fs have been demonstrated directly out of a Ti:sapphire oscillator [111] and pulse durations close to the theoretical limit have been achieved by external pulse compression [112].

In order to generate ultrashort laser pulses it is necessary to constructively superpose a large number of longitudinal modes ($\rightarrow$ broad fluorescence spectrum) inside the laser cavity, all having a fixed phase condition relative to each other. In Ti:sapphire oscillators this is achieved by 'Kerr-Lense-Modelocking' (KLM) [113]. The third order nonlinear optical susceptibilty $\chi^{(3)}$ of the Ti:sapphire crystal results in a refractive index, which depends on the intensity of the incident light: $n = n_0 + n_2 I$ ($n_2 = 3.1 \times 10^{-16}\mathrm{cm^2/W}$).

Thus an intense laser mode with a given transverse intensity distribution experiences a tranverse refractive index profile inside the Ti:sapphire crystal, which acts as a focussing lense (selffocussing). As a result, laser modes, which randomly interfere constructively to intense light pulses undergo stronger selffocussing than low intense continuous wave (cw) modes. The laser oscillator is then designed in such a way that it shows a higher quality for strongly selffocused modes. Consequently, intense pulses formed by constructively interfering modes with fixed phase relation see a lower loss and are amplified, whereas cw modes experience higher losses and eventually die out (SAM: Self Amplitude Modulation).

The longitudinal intensity distribution of short intense light pulses leads to an intensity dependent phase shift (SPM: Self Phase Modulation). For a positive non-linear refractive index ($n_2 > 0$), as in the case of Ti:sapphire, this results in positive temporal pulse spreading. This is also referred to as frequency chirp and positive spreading denotes the case where blue spectral components are retarded with respect to the red. Further positive pulse spreading is caused by the optical components in the laser cavity (e.g. mirrors, lenses), which introduce normal (positive) group velocity dispersion (GVD). Therefore, in order to obtain stable modelocking and minimally short laser pulses, prism pairs are implemented in the oscillator, which produce an anomalous (negative) GVD and compensate for the positive frequency chirp caused by the Ti:sapphire crystal and other optical components.

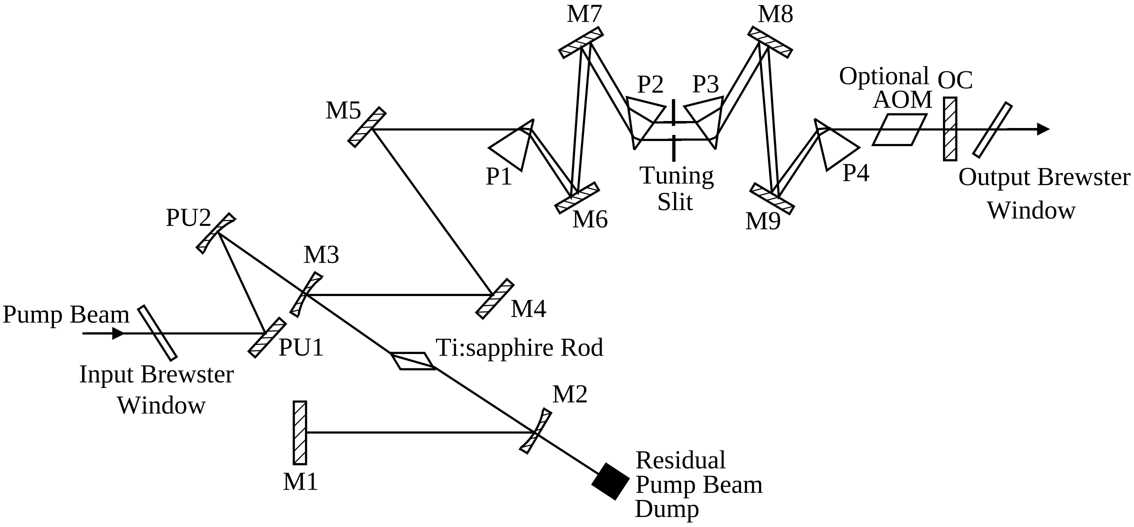

FIGURE 3.1: Configuration of the commercial Ti:sapphire oscillator (Spectra Physics, Tsunami).

Fig. 3.1 shows a schematic of the commercial Ti:sapphire oscillator employed in this work

(Spectra Physics, Mountain View, CA, USA, Tsunami). The pump beam supplied by a commercial intra-cavity frequency doubled $\mathrm{Nd{:}YVO_4}$ laser (Spectra Physics, Millenia V) with 5.5W maximum output power (cw) at a wavelength of 532nm enters through an input Brewster window and is guided as well as focused into the Ti:sapphire rod by the mirrors PU1 and PU2. M2 and M3, which form part of the folded Ti:sapphire oscillator configuration, are curved dichroic mirrors highly transmittive for the pump frequency (λ_{Pump} = 532 nm) and highly reflective for the laser frequency (NIR). The residual pump beam is blocked behind M2. M1 is the end mirror of the Ti:sapphire oscillator. P1 - P4 form the prism pairs used to compensate for positive GVD. A tuning slit of constant width and adjustable position between P2 and P3 provides for frequency tuning. After leaving the oscillator through the output coupler OC, the beam is guided through an output Brewster window. The total length of the folded oscillator configuration determines the repetition rate of the emitted laser pulse sequence (80 MHz, see below). An acousto-optical modulator (AOM) can optionally be employed to actively start and stabilize modelocking.

3.2 Laser Pulse Characterization

In order to evaluate SHG experiments quantitatively, it is essential to determine the properties and defining parameters of the employed laser source. As part of this work an experimental setup was developped to measure the relevant laser pulse parameters. The setup employed a custom-built pulse train detector to determine the repetition rate as well as a charge coupled device (CCD) array spectrometer (Ocean Optics HR4000) to record the spectral composition of the laser pulses. The average power was measured with a standard commercial power meter (Coherent, Santa Clara, CA, USA, Field Master with LM-3 power head). The heart of the setup, however, is the custom-built autocorrelator used to measure the temporal pulse duration. It is based on a Michelson interferometer and schematically shown in Fig. 3.2.

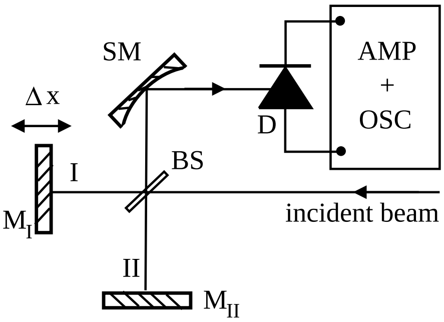

FIGURE 3.2: Schematic of the custom-built autocorrelator, M_{I}, M_{II}: mirrors, BS: beam splitter, SM: spherical mirror, D: AlGaAs detector diode, AMP: amplifier, OSC: oscilloscope, Δx: optical path length difference.

The incident laser beam is divided by a 1:1 dielectric beam splitter (BS) into two branches I and II, which are both back reflected onto themselves by the mirrors $\mathrm{M_I}$ and $\mathrm{M_{II}}$. A spherical mirror (SM) is used to focus the reflections of the two branches, which are spatially superposed by the beamsplitter, in a custom-modified reversed biased AlGaAs-light emitting diode (LED), which is used as a detector. The band gap energy of the AlGaAs-diode is larger ($\approx$ 1.9 eV) than the single photon energy of the incident laser pulses (1.59 eV). Linear absorption is therefore suppressed and the generated photo current is expected to be mainly due to two photon absorption (TPA) in the diode. Fig. 3.3 shows the measured photo current generated in the AlGaAs-diode by pulsed NIR fs irradiation as a function of the incident laser intensity in normalized arbitrary units. The photocurrent is amplified, recorded in a quasi-cw measurement averaging over the 80 MHz pulse sequence and displayed using a standard oscilloscope. The data in Fig. 3.3 are least square fitted by the function $y \propto x^{2.07}$, yielding an approximately quadratic relationship. This is experimental evidence that the electron-hole pairs generating the observed photo current are dominantly created by two photon absorption (TPA) in the AlGaAs detector diode.

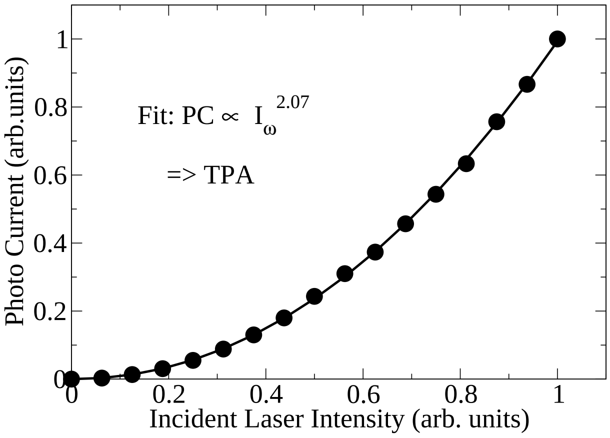

FIGURE 3.3: (Normalized) photo current (PC) of AlGaAs detector diode vs. (normalized) incident laser intensity (I_ω). Filled circles: data points; solid line: fit; approx. quadratic relation; two photon absorption (TPA).

If the difference in optical path length Δx between the branches I and II of the Michelson interferometer is varied as indicated in Fig. 3.2 yielding a time delay $\Delta t = \Delta x/c$ between the splitted pulses I and II, an interference pattern is observed in the recorded photo current as a function of Δt. This interference pattern is conventionally called the autocorrelation function of the laser pulse. The expected maximum signal to offset ratio $PC(S)/PC(O)$ of the autocorrelation function is calculated as follows taking the two-photon absorption process in the detector diode into account. $PC(O)$ denotes the case of uncorrelated laser pulses reaching the detector diode from branches I and II for $\Delta \mathrm{t} \gg \tau_\mathrm{P}$, whereas $PC(S)$ denotes the case of full temporal overlap.

$$\frac{PC(S)}{PC(O)} \propto \frac{I(S)^2}{I(O)^2} \propto \frac{(|E_I + E_{II}|^2)^2}{(|E_I|^2)^2 + (|E_{II}|^2)^2} = \frac{(2 \cdot E_I)^4}{2 \cdot (E_I)^4} = \frac{16 \cdot (E_I)^4}{2(E_I)^4} = \frac{8}{1} \tag{3.1}$$

Here $I(S)$ and $I(O)$ are the resultant signal and offset laser intensities incident on the detector diode, respectively. E_I and E_{II} are the electric field amplitudes of the laser pulses originating from the two branches I and II, respectively. $E_I = E_{II}$ holds, since a 1:1 beam splitter is used.

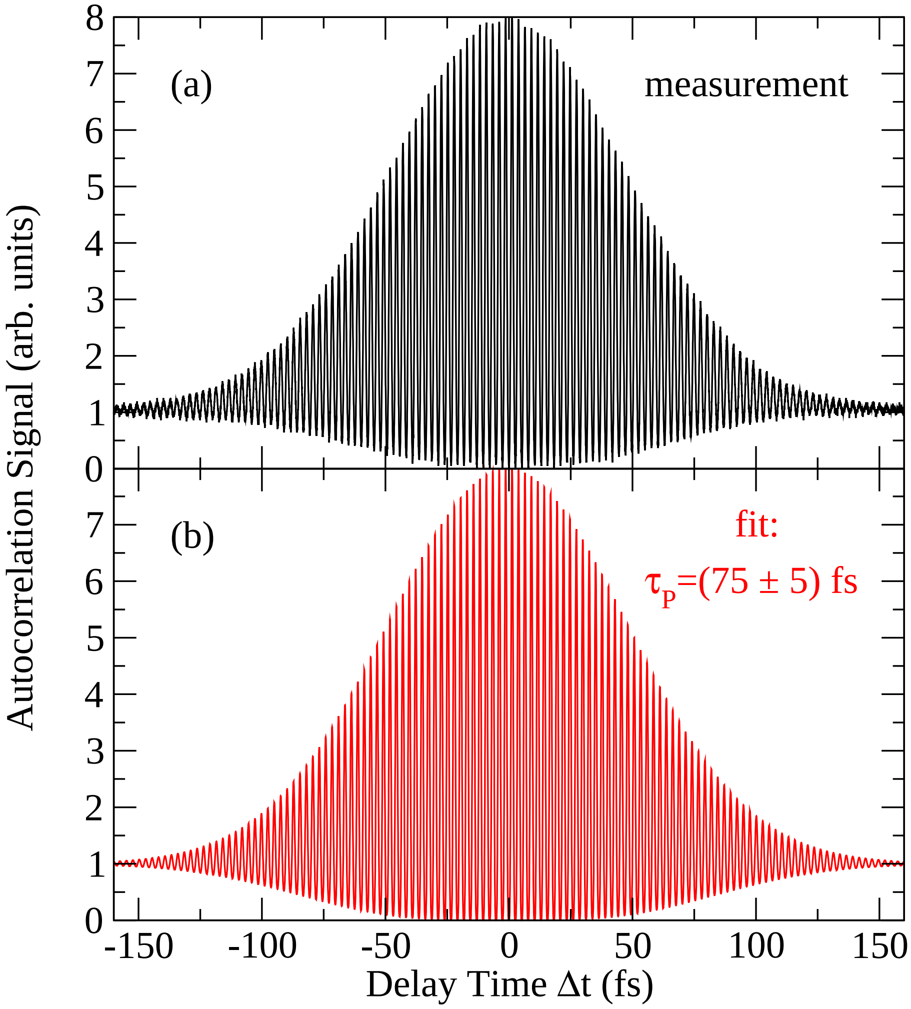

FIGURE 3.4: (a): Typical measured autocorrelation trace of the Ti:sapphire laser output. (b): data fit: laser pulse duration (FWHM of intensity envelope): $\tau_P = (75 \pm 5)$ fs.

Figs. 3.4 (a) and (b) show a typical measured autocorrelation trace of the here employed Ti:sapphire laser output and the corresponding numerical data fit, respectively. Fit and experiment, which are plotted separately for visibility, show very good agreement and reflect the 8/1 maximum signal to offset ratio. The fit assumes a sinusoidal carrier wave and a Gaussian envelope function for the incident laser pulse. The electric fields describing the splitted laser pulses travelling through the branches I and II of the Michelson interferometer, which are superposed in the detector diode can thus be expressed as:

$$E_I(t) = E_I \cdot e^{-2t^2/\tau^2} \cdot \sin(\omega t) \tag{3.2a}$$

$$E_{II}(t - \Delta t) = E_{II} \cdot e^{-2(t-\Delta t)^2/\tau^2} \cdot \sin(\omega(t - \Delta t) + \phi) \tag{3.2b}$$

Here ω is the frequency of the carrier wave. The $1/e$-width of the Gaussian electric field envelope function amounts to $\sqrt{2} \cdot \tau$. The phase shift between the two carrier waves introduced by the dielectric beam splitter is denoted by ϕ and Δt is the time delay between the splitted pulses I and II.

Given a two photon absorption process, the measured photo current $PC(\Delta t)$ as a function of the delay time Δt is proportional to the square of the total intenstity $I(\Delta t)$ incident on the detector integrated over time t, which is written as:

$$PC(\Delta t) \propto I^2(\Delta t) = \int (|E_I(t) + E_{II}(t - \Delta t)|^2)^2 dt \tag{3.3}$$

The right hand side of Eq. 3.3 represents a convolution integral, which can be computed after the insertion of Eqs. 3.2a and 3.2b. The result is represented by the curve in Fig. 3.4 (b), which is least square fitted to the experimental data using an appropriate software package [114]. ω is measured directly (see below). $E_I = E_{II}$, ϕ and τ are fit parameters, which, once extracted, fully determine the electric field function of the laser pulses in Eqs. 3.2a and 3.2b.

The temporal pulse duration τ_P is conventionally given by the full width at half maximum (FWHM) of the intensity envelope function of the laser pulse, which is related to the electric field envelope by $I \propto |E|^2$. For the Gaussian functions as defined in Eqs. 3.2a and 3.2b for the electric field envelope τ is equivalent to the $1/e$-width of the intensity envelope and $\tau_P = \sqrt{\ln 2} \cdot \tau$ (FWHM). Finally, τ_P is extracted from the fit and amounts to $\tau_P = (75 \pm 5)$ fs for the here employed laser source. It is noted that for vanishing delay time Δt = 0, destructive interference is observed (Fig. 3.4), which is rationalized by the phase shift of ϕ = $\pi/2$ between the splitted pulses I and II introduced by the employed dielectric beam splitter.

As mentioned in section 3.1, the temporal pulse duration τ_P and the spectral frequency width $\Delta\nu$ of the laser pulse are related by the Fourier transform. Fig. 3.5 shows a typical measurement of the spectral composition of the Ti:sapphire laser output, which corresponds to the autocorrelation trace shown in Fig. 3.4. A Gaussian data fit (solid line in Fig. 3.5) yields a wavelength band width of $\Delta\lambda = (11.9 \pm 0.5)$ nm taken at FWHM as well as a center wavelength of 782.8 nm. The center frequency ω of the carrier wave hence amounts to $\omega = 2\pi c/\lambda = 2.41 \cdot 10^{15}$ s^{-1}. The time band width product $\tau_P \cdot \Delta\nu$ of the Ti:sapphire laser output is finally determined and amounts to the value (0.44 ± 0.04),

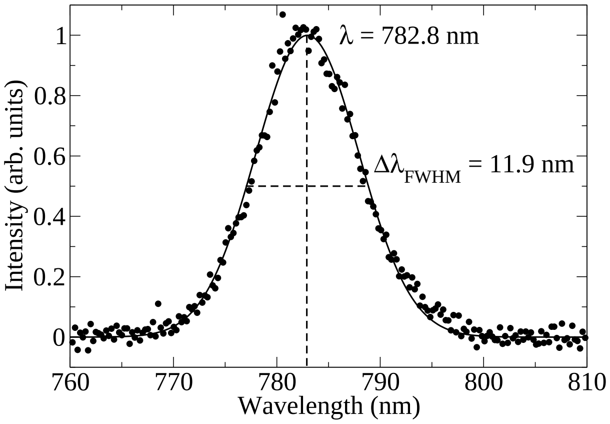

FIGURE 3.5: Measured spectral composition of Ti:sapphire laser output corresponding to the autocorrelation trace in Fig. 3.4, solid line: Gaussian fit, center wavelength: λ = 782.8 nm, wavelength band width $\Delta\lambda_{\mathrm{FWHM}}$ = (11.9±0.5) nm.

which is within the experimental uncertainty equivalent to the theoretical band width limit for Gaussian pulse shapes of 0.44.

The spatial shape of the laser beam profile is recorded on a silicon CCD camera (Spiricon SP980M) and found to be very close to a Gaussian TEM_{00} mode. Fluctuations in laser power remain $\leq$3% over several hours, which makes normalization in the experiments unnecessary. The output of the Ti:Sapphire oscillator is vertically polarized.

Table 3.1 summarizes the characteristic parameters of the Ti:sapphire laser source. The values of the listed parameters are applicable for the laser pulses as incident on the sample. The maximum pulse power P_{max} is determined assuming a Gaussian temporal intensity envelope for the laser pulse and hence calculated by $P_{max} = 0.94 \cdot E_P/\tau_P$, where E_P is the total pulse energy.

TABLE 3.1: Characteristic parameters of the employed Ti:sapphire laser source.

Max Average Power	P_{av}	840 mW
Repetition Rate	f_{rep}	80 MHz
Max Pulse Energy	E_P	10.5 nJ
Minimum Pulse Duration	τ_P	(75 ± 5) fs (FWHM of Intensity Envelope)
Max Pulse Power	P_{max}	130 kW
Center Wavelength	λ	782.8 nm
Spectral Width	$\Delta\lambda$	(11.9 ± 0.5) nm (FWHM at λ = 782.8 nm)
Time Band Width Product	$\tau_P \cdot \Delta\nu$	0.44 ± 0.04 ($\approx$ theoretical limit)
Max Pump Power	P_{Pump}	5.5 W
Pump Wavelength	λ_{Pump}	532 nm
Radial Mode		$\approx \mathrm{TEM}_{00}$
Polarization		vertical

3.3 Experimental Setup for SHG

Figure 3.6 shows a schematic diagram of the experimental setup, which was developped as part of this work and used to perform all SHG measurements presented here. The vertically polarized output of the Ti:sapphire oscillator is guided by gold mirrors M1 (Edmund Ind. Optics, Barrington, NJ, USA, protective coating, 1/4 wave surface accuracy at 632.8nm) through a $\lambda/2$-retarder plate (B. Halle Nachfl. GmbH, Berlin, Germany) and the polarizer P1 (Halbo Optics, Chelmsford, UK). In this way, firstly, the intensity incident on the sample can be varied by rotating the $\lambda/2$-retarder plate, and secondly, the incident polarization can be chosen by the polarizer P1. A red cut-off filter F1 (Edmund Ind. Optics, transmission < 1% (> 90%) for wavelengths < 570 nm (> 620 nm)) is used to avoid any SH potentially generated in the optical components to reach the sample. The fundamental laser beam is then focused onto the sample surface by the achromat L1 (Edmund Ind. Optics, focal length f=35 mm, NIR anti reflection coated).

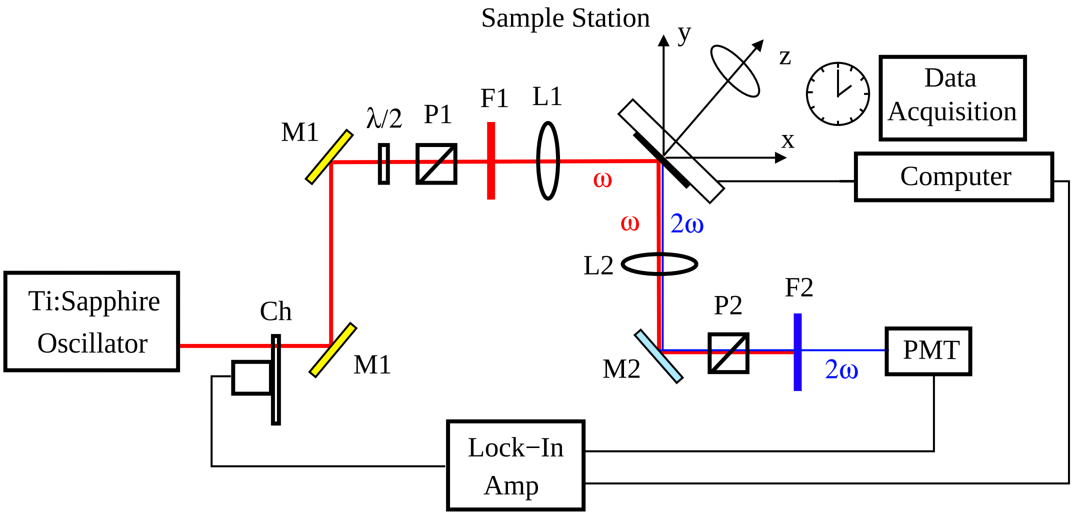

FIGURE 3.6: Schematic diagram of the experimental setup used for SHG experiments. Lock-in technique for noise reduction, computer automated data acquisition. CH: light chopper, M1: gold coated mirrors, $\lambda/2$: retarder plate, P1,P2: polarizers, F1: red cut-off filter, L1,L2: lenses, M2: UV-aluminium coated mirror, F2: filter combination, PMT: photomultiplier tube.

An incident angle of 45° and a fundamental frequency of 782.8 nm was chosen for all experiments. The reflected light is collected using a double convex lense L2 (Edmund Ind. Optics, f=125 mm, VIS-NIR anti reflection coated) and guided by an aluminium mirror M2 (Edmund Ind. Optics, UV enhanced aluminium coating, 1/4 wave surface accuracy at 632.8nm) through the analyzer P2 (Halbo Optics). The fundamental frequency is separated from the SH by a filter combination F2 consisting of a blue cut-off filter (Edmund Ind. Optics, transmission <1% (>95%) for wavelengths > 525 nm (< 490nm)) and a bandpass interference filter with a band width of 10 nm centered at the SH frequency of 391.4 nm.

The SH signal is detected by a photomultiplier tube (PMT) (Hamamatsu R760) in a quasi-cw measurement integrating over the 80 MHz laser pulse sequence. The PMT is connected to a high voltage of 1200 V in all experiments. To reduce the signal to noise ratio a lock-in amplifier (Ithaco, Dynatrac Model 393) is used in combination with a 500Hz light chopper (Ch). Computer automated data acquisition (National Instruments, Austin, TX, USA, Labview) is employed involving A/D-conversion at a sampling rate of 700 Hz as well as data point averaging. The $\mathrm{Si/SiO_2}$ sample is mounted on a 3D sample stage (Newport, Irvine, CA, USA), which allows for SH measurements as a function of the azimuthal angle in rotation about the z-axis (rotational SH anisotropy) as well as the X-Y-position of the sample (spatial SH imaging). The maximum experimental resolutions are 1.8^o for the SH anisotropy measurements and $5\mu\mathrm{m}$ for spatial SH imaging. The setup is suitable to record the time dependence of the SH signal with a resolution of ~ 0.2 s. The SHG experiments can be performed polarization resolved with respect to excitation and detection. The four polarization combinations between the incident fundamental and analyzed SH waves are denoted by p-p, p-s, s-p and s-s (p = parallel, s = perpendicular with respect to plane of incidence).

The intensity of the laser fundamental incident on the sample is not easily accessible by a direct measurement. Therefore, the z-scan technique is employed to determine the Rayleigh length and hence the laser spot size at the focal position. The total generated SH power $P_{2\omega}(z)$ is measured experimentally as a function of the sample position z along the propagation direction of the incident beam. The following formalism based on the standard theory of Gaussian beam propagation [115] allows to correlate $P_{2\omega}(z)$ with the focal spot size and hence to determine the laser intensity incident on the sample.

Since the laser beam is directed onto the sample under an angle $\theta = 45°$, an elliptic Gauss function is assumed for the transverse spatial intensity profile of the incident fundamental wave:

$$I_\omega(x,y) = I_{\omega 0} \cdot \exp(-2x^2/w^2) \cdot \exp(-2\cos^2\theta \ \cdot y^2/w^2) \tag{3.4}$$

Here $I_{\omega 0}$ is the intensity at the position ($x = 0, y = 0$) and $w = w(z)$ is the radius of the incident beam of frequency ω at the position z along the propagation direction. It is noted that the Gauss function as defined in Eq. 3.4 for the fundamental intensity envelope is consistent with the convention that $w(z)$ denotes the $1/e$-beam radius of the electric field envelope. $w(z)$ is then related to the Rayleigh length z_R by [115]

$$w = w(z) = w_0 \cdot \left(1 + z^2/z_R^2\right)^{1/2} \tag{3.5}$$

where

$$z_R = \pi w_0^2/\lambda \tag{3.6}$$

holds for the Rayleigh length z_R with $\lambda = 2\pi c/\omega$. The waist radius $w_0 = w(z = 0)$ is the minimum beam radius at the waist position $z = 0$.

The total fundamental power P_ω incident on the sample is calculated by evaluating the integral $P_\omega = \int\int I_\omega(x, y)dxdy$, which yields:

$$P_\omega = I_{\omega 0} \cdot \frac{\pi w^2}{2\cos\theta} \tag{3.7}$$

According to Eq. 2.45 the generated SH intensity is a quadratic function of the incident fundamental intensity, which yields the following expression for the transverse spatial shape of the SH intensity $I_{2\omega}(x, y)$ assuming Eq. 3.4 for the fundamental wave:

$$I_{2\omega}(x, y) = \eta \cdot I_\omega^2(x, y) = \eta \cdot I_{\omega 0}^2 \cdot \exp(-4x^2/w^2) \cdot \exp(-4\cos^2\theta \ \cdot y^2/w^2) \tag{3.8}$$

Here η is introduced for the SH conversion efficiency.

Integrating over $I_{2\omega}(x, y)$ the total generated SH power is obtained:

$$P_{2\omega} = \eta \cdot I_{\omega 0}^2 \cdot \frac{\pi w^2}{4\cos\theta} \tag{3.9}$$

The comparison of Eqs. 3.7 and 3.9 yields:

$$P_{2\omega} = \eta \cdot P_\omega^2 \cdot \frac{\cos\theta}{\pi w^2} \propto \frac{1}{w^2} \tag{3.10}$$

Inserting Eq. 3.5 into Eq. 3.10, the SH power $P_{2\omega} = P_{2\omega}(z)$ as a function of the position z is finally expressed in terms of the Rayleigh length z_R:

$$P_{2\omega} = P_{2\omega}(z) = \eta \cdot P_\omega^2 \cdot \frac{\cos\theta}{\pi w_0^2(1 + z^2/z_R^2)} = \frac{K}{1 + z^2/z_R^2} \tag{3.11}$$

with $K = (\eta P_\omega^2 \cos\theta)/(\pi w_0^2)$.

Fig. 3.7 shows a typical measurement of the total SH power $P_\omega(z)$ generated at the $\mathrm{Si/SiO_2}$ interface as a function of the sample position z. The solid curve is a fit according to Eq. 3.11 with K and z_R as fit parameters. The Rayleigh length is extracted and amounts to z_R = 0.244 mm, which according Eq. 3.6 results in a beam waist of w_0 = 7.5 μm at the focal position $z = 0$. Hence the spot diameter is found to be 15 $\mu\mathrm{m}$ with an estimated error bar of ± 2 $\mu\mathrm{m}$. In all experiments the $\mathrm{Si/SiO_2}$ sample is positioned at $z = 0$.

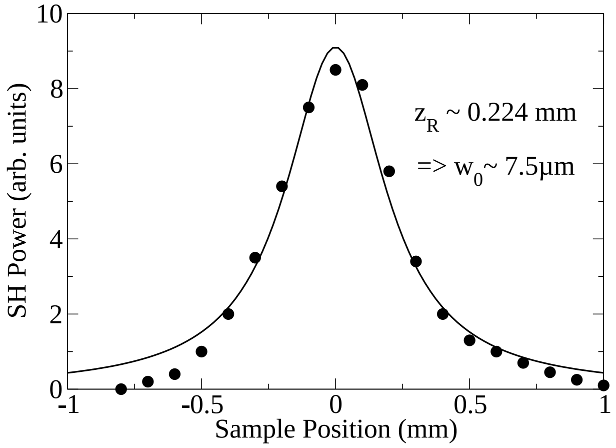

FIGURE 3.7: Measured SH power as a function of the sample position z along the incident laser beam propagation direction. solid line: Fit according to Eq. 3.11: Rayleigh length z_R = 0.224 mm, beam waist (radius) w_0 = 7.5 μm.

Using the value for the maximum pulse power P_{max} = 130 kW listed in Table 3.2, the maximum laser peak intensity directly incident on the sample is finally determined employing Eq. 3.7 and amounts to $\approx 100\mathrm{GW/cm^2}$.

3.4 Experimental Setup for UV Irradiation

In the experiments presented in section 4.4 $\mathrm{Si/SiO_2}$ samples are irradiated with UV excimer laser pulses. Fig. 3.8 shows a schematic diagram of the experimental setup, which was built during the course of this work and employed for the UV irradiation of $\mathrm{Si/SiO_2}$.

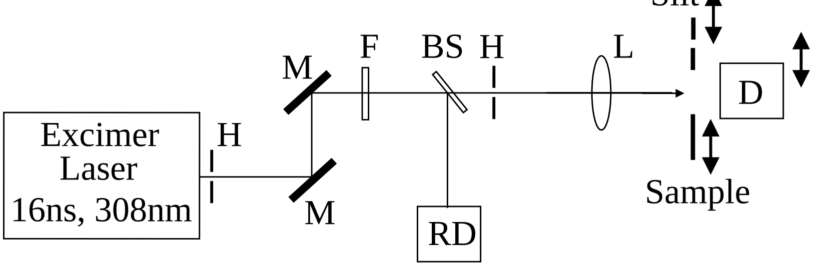

FIGURE 3.8: Setup for UV irradiation of $\mathrm{Si/SiO_2}$, H: pin holes, M: dielectric mirrors, F: attenuation filters, BS: beam splitter, L: lense, RD: reference detector, D: detector.

Here, M are dielectric mirrors, F are neutral density filters used to attenuate the beam and vary the pulse energy incident on the sample, BS is a dielectric beam splitter, L a lense of 300 mm focal length, H are pin holes used for beam shaping. D and RD are detectors recording the pulse energy. The XeCl excimer laser source (Lambda Physik, EMG 101 MSC) provides laser pulses of 16 ns duration at a repetition rate between 1 and 20Hz and an ultraviolet (UV) wavelength of 308 nm (4.03 eV photon energy).

In a first step, the ratio $\mathrm{E_D/E_{RD}}$ between the energy readings of the detector (D) and the reference detector (RD) is determined precisely by averaging over 100 laser shots. In a second step, the cross-sectional energy distribution of the UV laser pulses is determined by the stepwise translation of a slit through the beamline while the transmitted energy is recorded. In a third step, the slit as well as the detector (D) are removed and the sample is placed into the beamline exactly at the position, where the slit measurement is taken (indicated by arrows in Fig. 3.8).

Following this procedure, the total energy of each laser pulse incident on the sample can be determined by evaluating the respective reading of the reference detector (RD) and multiplying it by the ratio $\mathrm{E_D/E_{RD}}$. Uncertainties due to pulse-to-pulse energy fluctuations are eliminated in this way. The spatial energy distribution of the approximately elliptic UV laser beam shape is determined by the slit measurement. Fig. 3.9 shows a typical normalized energy distribution recorded across the long axis of the approximately elliptic beam cross-section. The Gaussian fit yields a 1/e-width of (1.1 ± 0.1) mm in satisfactory agreement with the experiment. For all experiments presented in this study a 1/e-width of 2l = 1.1 mm was chosen.

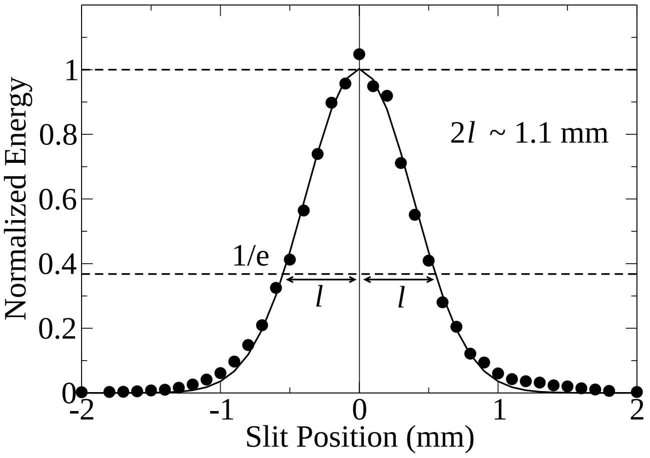

FIGURE 3.9: Normalized energy distribution determined across the long axis of the approximately elliptic excimer laser output by the slit method, solid line: Gaussian fit: 1/e-width (1.1 ± 0.1) mm.

The ratio between the short (y-direction) and the long axis (x-direction) of the elliptic spatial beam shape is ~ 0.75. Thus, an elliptic Gaussian profile as in Eq. 3.12 can be assumed for the energy distribution of the excimer laser pulses,

$$E(x, y) = E_0 \left(exp(-x^2/l^2) \cdot exp(-y^2/(0.75 \cdot l)^2)\right) \tag{3.12}$$

with E_0 being the peak energy of the laser pulse at the position $x = y = 0$. The total pulse energy is represented by the integral $\int\int E(x, y)dxdy$. The measured total pulse energy values between 3.2 mJ and 20 mJ hence correspond to fluences between 0.45 and 2.8 $\mathrm{J/cm^2}$. Taking the pulse duration of 16 ns into account, these values are eqivalent to peak intensities between 28 $\mathrm{MW/cm^2}$ and 175 $\mathrm{MW/cm^2}$.

3.5 Sample Preparation and Properties

All samples investigated in this study were Czochralski-grown single crystalline silicon wafers (Wacker Siltronic, Burghausen, Germany or Crystec, Berlin, Germany) with (100) surface orientation. In all cases the as-delivered wafers were first degreased by sonicating in organics (methanol, acetone, trichlorethylene, acetone, methanol), rinsed with deionized water and then treated in an aqueous HF solution to remove the oxide [116, 117]. After that the samples were stored under dark normal laboratory conditions (room temperature, atmospheric pressure) to build up a native $\mathrm{SiO_2}$ layer with an equilibrium thickness below 5nm [77]. All measurements were recorded within a time window of 70 - 110 hours after sample preparation.

Boron (B) doped p-type wafers (Crystec, Berlin, Germany) of resistivities between > 6000 $\Omega\mathrm{cm}$ and < 0.01 $\Omega\mathrm{cm}$ were studied, which is equivalent to doping concentrations between < $2 \cdot 10^{12}$ $\mathrm{cm^{-3}}$ and > $8.5 \cdot 10^{18}$ $\mathrm{cm^{-3}}$. Phosphorous (P) as well as Arsenic (As) doped n-type wafers (Crystec, Berlin, Germany) of resistivities ranging from 1800 - 2000 $\Omega\mathrm{cm}$ to < 0.005 $\Omega\mathrm{cm}$, which correspond to doping levels between $\sim$ 10^{12} $\mathrm{cm^{-3}}$ and > 10^{19} $\mathrm{cm^{-3}}$ were investigated.

The optical constants (absorption coefficient [118, 119]) of silicon imply that the absorption depth of the fundamental NIR frequency of 782.8 nm used for SHG is $\sim$ $11\mu\mathrm{m}$. The escape depth of the generated SH frequency of 391.4 nm is, however, $\sim$ 100 nm. $\mathrm{SiO_2}$ is transparent down to vacuum UV due to its large band gap of 8.9 eV [80]. SHG in $\mathrm{Si/SiO_2}$ is hence either a pure interface effect or a bulk effect (higher order multipole terms or EFISH) originating from the $\sim$ 100 nm thin silicon layer near the interface.

A first order calculation employing the optical constants as well as the heat conductivity of silicon indicates that NIR irradiation of 10.5 nJ pulse energy at a repetition rate of 80 MHz yields no significant heat accumulation in $\mathrm{Si/SiO_2}$ due to the pulsed radiation, particularly since $\sim$ 50% of the incident light is reflected. In addition, the incident beam is periodically interrupted by the employed light chopper (section 3.3). The peak intensity damage threshold of silicon is reported in the literature to be $10^3\ \mathrm{GW/cm^2}$ for laser pulses of 90 fs duration at a wavelength of 620 nm [24, 120] and $10^4\ \mathrm{GW/cm^2}$ for 120 fs pulses in the NIR spectral region (700 - 1000) nm [121]. Another source quotes that the damage threshold of silicon for NIR light is reached for peak intensities of about 100 $\mathrm{GW/cm^2}$. Since the latter value is only an estimate and the former quotes result from experimental investigations, it is assumed that for the here applied peak intensities damage of the sample plays a neglegible role. At the employed excimer laser wavelength of 308 nm the penetration depth in silicon amounts to $\approx$ 10 nm.

Chapter 4

Experimental Results

In the following chapter the SH measurements performed at native $\mathrm{Si/SiO_2}$ interfaces during the course of this work are presented. All samples are natively oxidized silicon wafers cut in the (100) surface orientation and, hence, under p-polarized excitation and detection they yield a rotational SH anisotropy pattern as typically shown in Fig. 4.1, reflecting the four fold symmetry [26, 33, 65, 84, 92]. The solid line in Fig. 4.1 is a fitting curve following Eq. 2.50. All time dependent SH measurements are performed at a maximum of the azimuthal rotational SH anisotropy pattern of the respective sample and in the (p,p) polarization combination in order to obtain comparable SH signal heights.

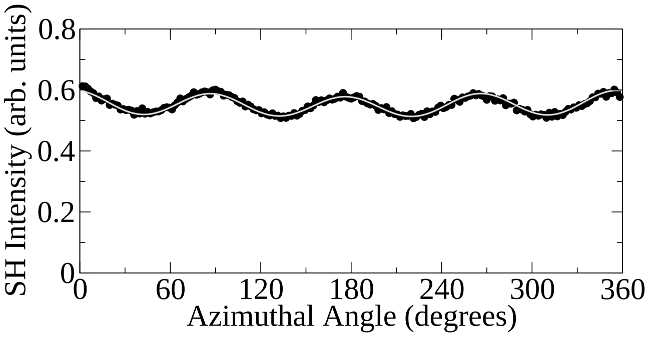

FIGURE 4.1: Rotational SH anisotropy pattern of natively oxidized Si(100) recorded with (p,p) polarization a fitted according to Eq. 2.50.

In a first set of experiments the time dependent SH response of virgin $\mathrm{Si/SiO_2}$ is investigated in the new intensity regime up to 100 $\mathrm{GW/cm^2}$. The second set is designed to systematically investigate the SH signal of pre-irradiated samples after irradiation interrupts. In the third series of measurements the temporal SH response of substantially doped $\mathrm{Si/SiO_2}$ is studied and the fourth and last set of experiments is attributed to the SHG analysis of $\mathrm{Si/SiO_2}$ after its exposure to high intensity UV excimer laser irradiation. The following chapter thus comprises four sections separately presenting the results of the different experimental series.

4.1 SH Response of Virgin Si/SiO$_2$

Figure 4.2 shows the temporal SH signal evolution of $\mathrm{Si/SiO_2}$ as a function of the applied peak intensity. Each curve is recorded starting from a virgin sample spot on a lightly Boron doped natively oxidized silicon wafer (Wacker, Burghausen, Germany, resistivity $> 10\ \Omega\mathrm{cm}$) prepared in the way described above (section 3.5).

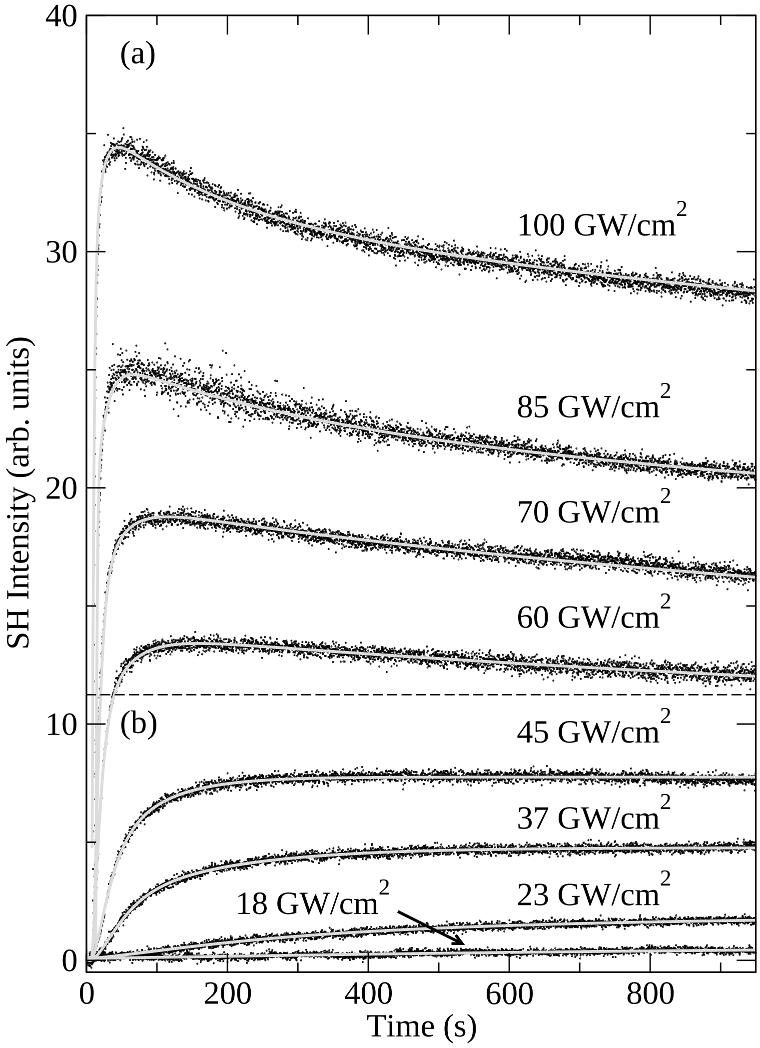

FIGURE 4.2: Temporal evolution of the SH signal in native $\mathrm{Si/SiO_2}$ interfaces irradiated at peak intensities $> 45\ \mathrm{GW/cm^2}$ (a) and $\leq 45\ \mathrm{GW/cm^2}$ (b); the solid lines are fitting curves using two exponential functions for electron dynamics ((b): Eq. 5.1 [77, 78, 80, 94])) and four exponential functions, i.e. two functions as in (b) complemented by two exponential functions for hole dynamics ((a): Eq. (5.2)); see chapter 5 and Ref. [102]).

For peak intensities $\leq$ 45 $\mathrm{GW/cm^2}$ (Fig. 4.2 (b)), the SH intensity increases on a time scale of minutes and subsequently reaches an equilibrium level. This effect is well known and referred to as electric field induced second harmonic (EFISH) generation. The observed data can be numerically reproduced by two exponential functions following Eq. 5.1 (solid curves in Fig. 4.2 (b)). These data are consistent with and fully confirm the results reported previously by various other authors [77, 78, 80, 94].

In the intensity regime between 45 - 100 $\mathrm{GW/cm^2}$ (Fig. 4.2 (a)), which is investigated for the first time in this study, the SH intensity is found to develop in a distinctly different way [101, 102]. The SH signal rises up to a maximum within 1-2 min and thereafter decreases on a time scale of many minutes. This behaviour becomes more pronounced the higher the incident peak intensity. The solid curves in Fig. 4.2 (a) are fitting curves involving four exponential functions according to Eq. 5.2 (see section 5.1).

4.2 SH Response of Pre-Irradiated Si/SiO$_2$

The following section deals with the systematic analysis of the SH response of pre-irradiated $\mathrm{Si/SiO_2}$ samples after irradiation interrupts of 10 to 600 s. The samples are first exposed to NIR femtosecond irradiation as described in the previous section 4.1, then allowed to relax during defined dark periods and subsequently re-irradiated. The temporal SH response of the $\mathrm{Si/SiO_2}$ samples pre-irradiated at various peak intensities is recorded and the relaxation behaviour of the sample as a function of the dark period duration is investigated. In addition SH imaging is employed to visualize pre-irradiated samples areas. Again lightly Boron doped samples of resitivities > 10 $\Omega\mathrm{cm}$ are chosen.

4.2.1 Time Dependent SH Measurements in Pre-Irradiated Si/SiO$_2$

Figure 4.3 includes the SH development curves of the virgin samples shown in Fig. 4.2 for irradiation times $\leq$ 960 s as well as the subsequent SH responses on alternating dark and irradiation periods. After 960 s of irradation the laser beam is blocked for 10 s (indicated by dashed line A), unblocked for 60 s until signal recovery, then blocked for 20 s (indicated by dashed line B) and unblocked for 60 s until recovery, and so forth. The subsequent blocking times are 30 s (C), 60 s (D), 180 s (E), 360 s (F), 600 s (G) with intermediate irradiation times of 180 s in between (D), (E), (F) and (G) to allow for signal recovery.

Looking at the curves recorded in the low intensity regime at 18 and 23 $\mathrm{GW/cm^2}$, the SH signal recovers within seconds after the dark period in contrast to the slow increase (minutes) of the SH intensity observed in virgin samples (Figs. 4.2(b) and 4.3). The SH increase is hence accelerated in pre-irradiated samples. Furthermore, the dark periods do not measurably affect the SH signal height upon re-irradiaion and the SH signal recovers to the equilibrium level achieved before the dark period. Such effects were previously reported by other authors [94, 95].

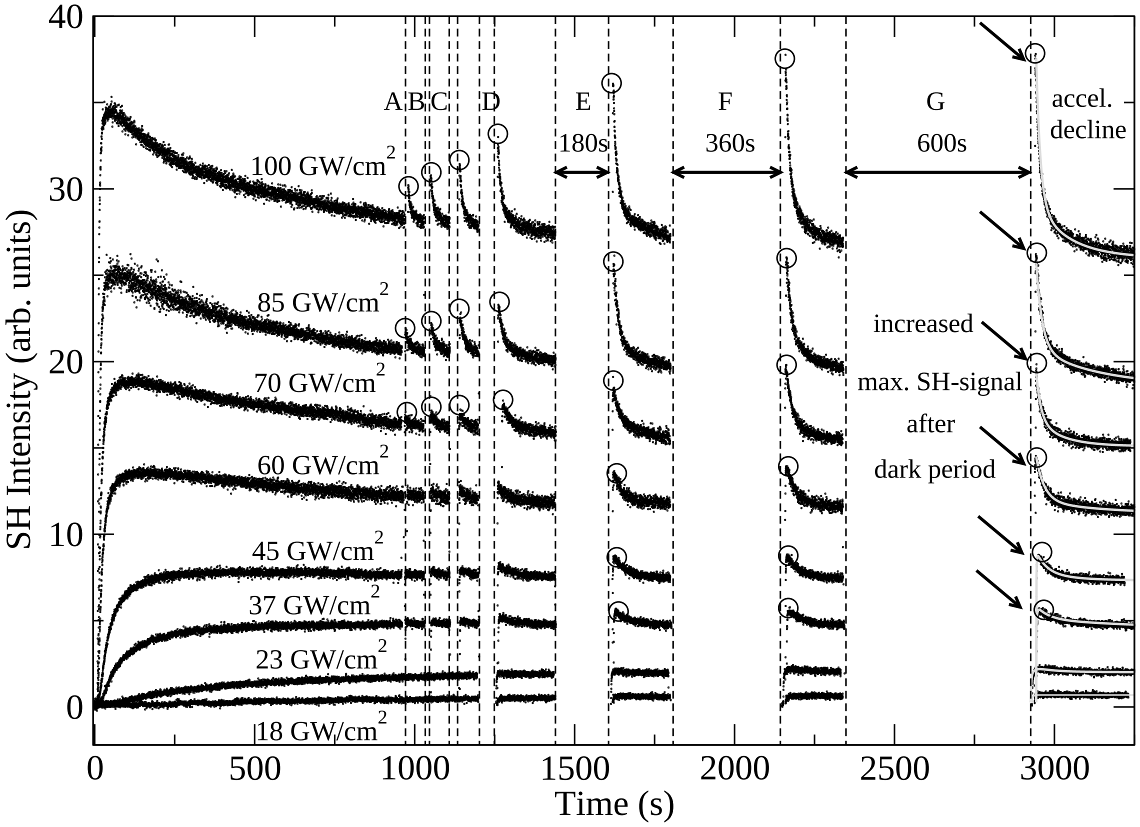

FIGURE 4.3: Temporal evolution of the SH signal in native Si/SiO$_2$ interfaces irradiated at various peak intensities. A-G indicate dark periods of 10 s (A), 20 s (B), 30 s (C), 60 s (D), 180 s (E), 360 s (F), 600 s (G); the solid lines are fitting curves for pre-irradiated samples according to Eqs. 5.1 and 5.2 [102].

In contrast to the above observations at low intensity, blocking of the laser beam yields two additional effects in the high intensity regime $\geq 37\ \mathrm{GW/cm^2}$:

(i) Upon re-irradiation the SH intensity rises above the level before the dark period (highlighted by arrows in Fig. 4.3). The magnitude of this enhancement (cf. empty circles in Fig. 4.3) increases with the duration of the dark period. For dark periods above 600 s the signal increase appears to be constant and the new SH signal maximum is reached very rapidly after unblocking the laser beam being even higher than the first maximum achieved with virgin sample spots.

(ii) The decline after each new signal maximum occurs on a significantly shorter time scale than the slow decline after the initial maximum of the virgin sample spot.

Both effects, (i) the enhancement of the SH signal amplitude after dark periods and (ii) the accelerated decline, become more pronounced the higher the peak intensity. With high peak intensity the SH signal increase up to the new maximum after dark periods (empty circles in Fig. 4.3) is faster than the experimental time resolution of 0.2 s.

To obtain further imformation about the origin of effect (i), the SH signal enhancement after dark periods observed in the high intensity regime $\geq$ 37 $\mathrm{GW/cm^2}$ (Fig. 4.3), the following experiment is performed as a test, whether the SH signal enhancement upon re-irradiation is a residual effect due to the preceeding high intensity irradiation or purely related to the intensity dependent EFISH effects in pre-irradiated samples. Hence, a virgin $\mathrm{Si/SiO_2}$ sample is first irradiated in the high intensity regime at 100 $\mathrm{GW/cm^2}$ for 960 s as in Figs. 4.2 and 4.3, thereafter allowed to relax during a dark period of 600 s and subsequently re-irradiated in the low intensity regime at 23 $\mathrm{GW/cm^2}$. The result is displayed in Fig. 4.4, where the SH intensity of the curve recorded at 23 $\mathrm{GW/cm^2}$ is multiplied by a factor 10 for visibility.

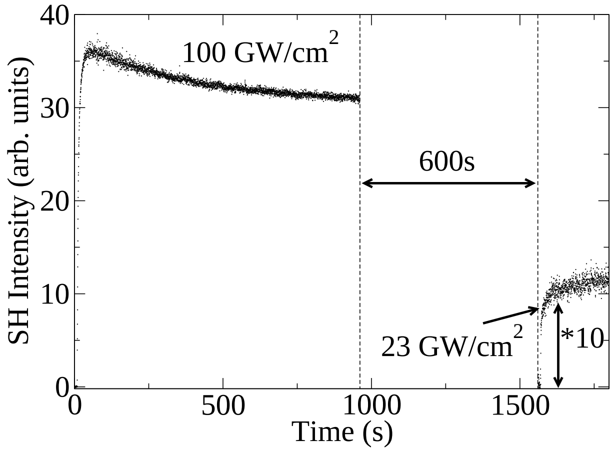

FIGURE 4.4: Temporal SH response of native $\mathrm{Si/SiO_2}$ irradiated at 100 $\mathrm{GW/cm^2}$ for 960 s and then probed at 23 $\mathrm{GW/cm^2}$ after a 600 s dark period.

The measurement in Fig. 4.4 unequivocally shows that the SH signal increases within seconds after pre-irradiation at high intensity (100 $\mathrm{GW/cm^2}$) and a sufficiently long dark period (600 s) compared to minutes with the virgin sample in Fig. 4.2. It shows no enhancement due to pre-irradation and subsequently saturates at the level related to the low intensity (23 $\mathrm{GW/cm^2}$). Hence, essentially similar temporal SH responses without SH signal enhancement are found upon re-irradiation with low intensity (23 $\mathrm{GW/cm^2}$) irrespective of the peak intensity used for pre-irradiation, as long as relaxation under dark conditions is long enough ($\geq$ 600 s). Therefore, the SH signal enhancement (empty circles in Fig. 4.3) is unambiguously related to the high intensitiy ($\geq$ 37 $\mathrm{GW/cm^2}$) EFISH

effects in the pre-irradiated samples but not to residual effects due to the preceeding irradiation. Otherwise a SH signal enhancement after dark periods would also be present upon low intensity re-irradiation following pre-irradiation at high intensity. This case is, however, ruled out by the measurement presented in Fig. 4.4.
Summarizing, drastic changes in the temporal SH response of $\mathrm{Si/SiO_2}$ samples are observed after pre-irradiation with NIR femtosecond laser pulses. The SH responses occur on a drastically shortened time scale and a SH signal enhancement after re-irradiation in the high intensity regime ($\geq 37\ \mathrm{GW/cm^2}$) is observed, the magnitude of which depends on the dark period duration [101, 102].

4.2.2 SH Imaging and Scanning Electron Microscopy of Pre-Irradiated Si/SiO$_2$

In the following, spatial SH imaging in combination with scanning electron microscopy (SEM) [125] is employed to gather further information about the change of the SH response of the $\mathrm{Si/SiO_2}$ interface observed in pre-irradiated samples.

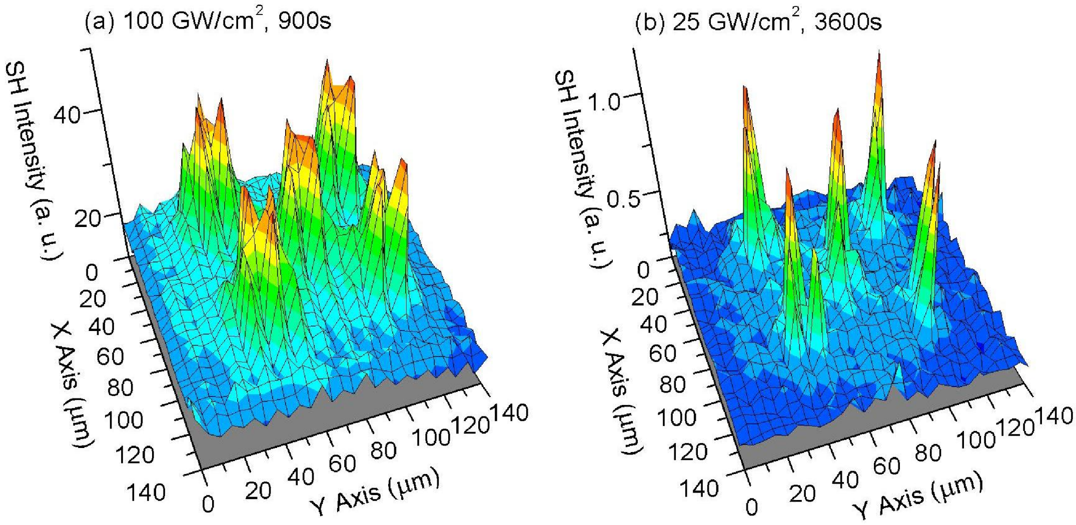

(a) 100 GW/cm^2, 900s

(b) 25 GW/cm^2, 3600s

FIGURE 4.5: SH images of samples (a) and (b) with five spots irradiated with (a) $100\ \mathrm{GW/cm^2}$ for 900 s, 0.2 s dwell time per scan position and (b) $25\ \mathrm{GW/cm^2}$ for 3600 s, 0.8 s.

Two $\mathrm{Si/SiO_2}$ samples (a) and (b) are exposed to NIR femtosecond irradiation of identical total dose $I^{(\omega)} \cdot t$, sample (a), however, to a high intensity ($100\ \mathrm{GW/cm^2}$) for 900 s and (b) to a low intensity ($25\ \mathrm{GW/cm^2}$) for 3600 s. Each sample is irradiated using these irradiation parameters at five positions in a square arrangement of 60 μm side length to ensure the unambiguous identification of the pre-irradiated sample areas. SH imaging is performed under the same irradiation conditions as the spot preparation with dwell times of 0.2 s and 0.8 s per scanning position on samples (a) and (b), respectively. The lateral step size is 5 μm for both samples in the X- and Y-directions. Both area scans are performed 90 min after the spot preparation using the experimental setup shown in Fig. 3.6.

Figure 4.5 shows the SH images of samples (a) and (b) as three dimensional (3D) plots. The pre-irradiated spots are clearly visible due to their accelerated SH response (section 4.2). The SH signal heights are consistent with the time dependent measurements shown in Figs. 4.2 and 4.3 taking into account the relevant dwell times of 0.2 s and 0.8 s as well as the applied intensities. The SH images indicate that the diameter of the visualized spots is larger in the case of high intensity pre-irradiation (a) although both exposures in Figs. 4.5 (a) and (b) apply an equal dose as well as identical Gaussian spatial beam shapes of (15 ± 2) μm diameter. Additional SH scans performed two weeks after sample preparation yield similar results indicating that the change of the SH response of Si/SiO_2 caused by the exposure to NIR femtosecond laser irradiation is irreversible [94, 95].

SEM images of the same pre-irradiated sample areas as in Fig. 4.5 are recorded with a standard commercial scanning electron microscope (Topcon ABT-60) at 7 keV beam energy at a magnification of 290.

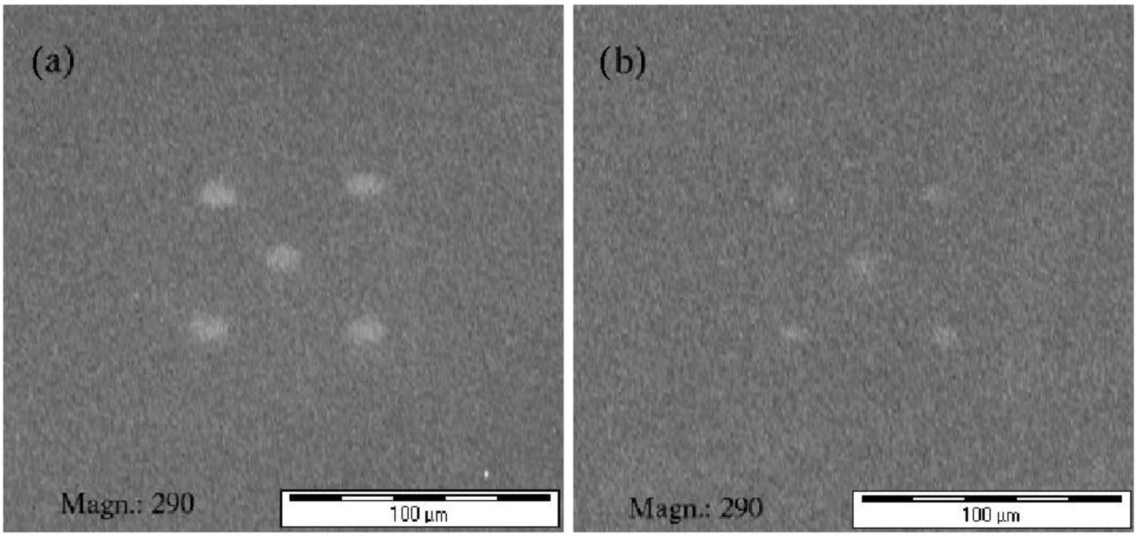

FIGURE 4.6: SEM images of samples (a) and (b) with five spots irradiated with (a) 100 GW/cm^2 for 900 s and (b) 25 GW/cm^2 for 3600 s (magnification 290).

Figure 4.6 displays the SEM images of the samples (a) and (b). The modification due to pre-irradiation is identified with a clear difference in contrast. Spots irradiated at higher peak intensity (a) show a stronger contrast than those of (b). Also the larger diameter of the spots in (a) is consistently observed in the SEM and SH images [101, 102].

4.3 SH Response of Highly Doped Si/SiO$_2$

In the following section the time dependent SH response of natively oxidized silicon wafers with doping concentrations up to $\sim 10^{19}$ cm^{-3} (p^{+}- and n^{+}- $\mathrm{Si/SiO_2}$) are investigated. All samples are Boron doped p-type silicon wafers as well as Phosphorous and Arsenic doped n-type silicon wafers of (100) surface orientation and originate from the same manufacturer (Crystec, Berlin, Germany). They are prepared using the above described procedure (see section 3.5). Moderate discrepancies in the absolute SH signal heights between the data presented in this section and in sections 4.1 and 4.2 are observed, since the doped wafers originate from a different manufacturer. This fact implies differences in the surface preparation techniques (e.g. polishing) and it is well established that e.g. differences in surface roughness affect the SH signal height of oxidized silicon wafers [5, 50, 60, 61, 66].

Figure 4.7 shows the temporal evolution of the SH response of natively oxidized Boron p-type doped silicon for incident laser peak intensities between 23 and 93 $\mathrm{GW/cm^2}$. All curves are recorded starting with a virgin sample spot on the respective wafer. Fig. 4.7 (a) displays the results obtained from a wafer of resistivity 0.7 - 2 $\Omega\mathrm{cm}$, which corresponds to a Boron doping level of ($6.3{\cdot}10^{15}$ - $2.1{\cdot}10^{16}$) cm^{-3}. Samples of resistivities higher than the above values ($>$ 2 $\Omega\mathrm{cm}$) show a very similar SH response as seen in Fig. 4.7 (a), which is comparable to that in Fig. 4.2. Hence, a consistent and reproducible SH response is found for low Boron doping concentrations (resistivities $>$ 2 $\Omega\mathrm{cm}$). In contrast to this, Figs. 4.7 (b) and (c) show the time dependent SH response of wafers with substantially higher Boron doping concentrations of $7.5 \cdot 10^{17}$ - $8.5 \cdot 10^{18}$ cm^{-3} (resistivity 0.01 - 0.05 $\Omega\mathrm{cm}$) and $> 8.5{\cdot}10^{18}$ cm^{-3} (resistivity < 0.01 $\Omega\mathrm{cm}$), respectively. The solid lines in Fig. 4.7 (c) are fitting curves according to Eq. 5.4. In contrast to Fig. 4.7 (a) two decisively different observations can be identified in Figs. 4.7 (b) and (c).

On the one hand, the SH decrease on a time scale of many minutes observed after the SH signal maximum at intensities $>$ 45 $\mathrm{GW/cm^2}$ becomes less pronounced the higher the Boron doping level (the lower the resistivity). In contrast to an approximate decrease by 20 % at 93 $\mathrm{GW/cm^2}$ after 960 s in Fig. 4.7 (a) (consistent with Fig. 4.2), declines of only 4.3 % and 3.4 % are found at 93 $\mathrm{GW/cm^2}$ after 960 s in (b) and (c), respectively. On the

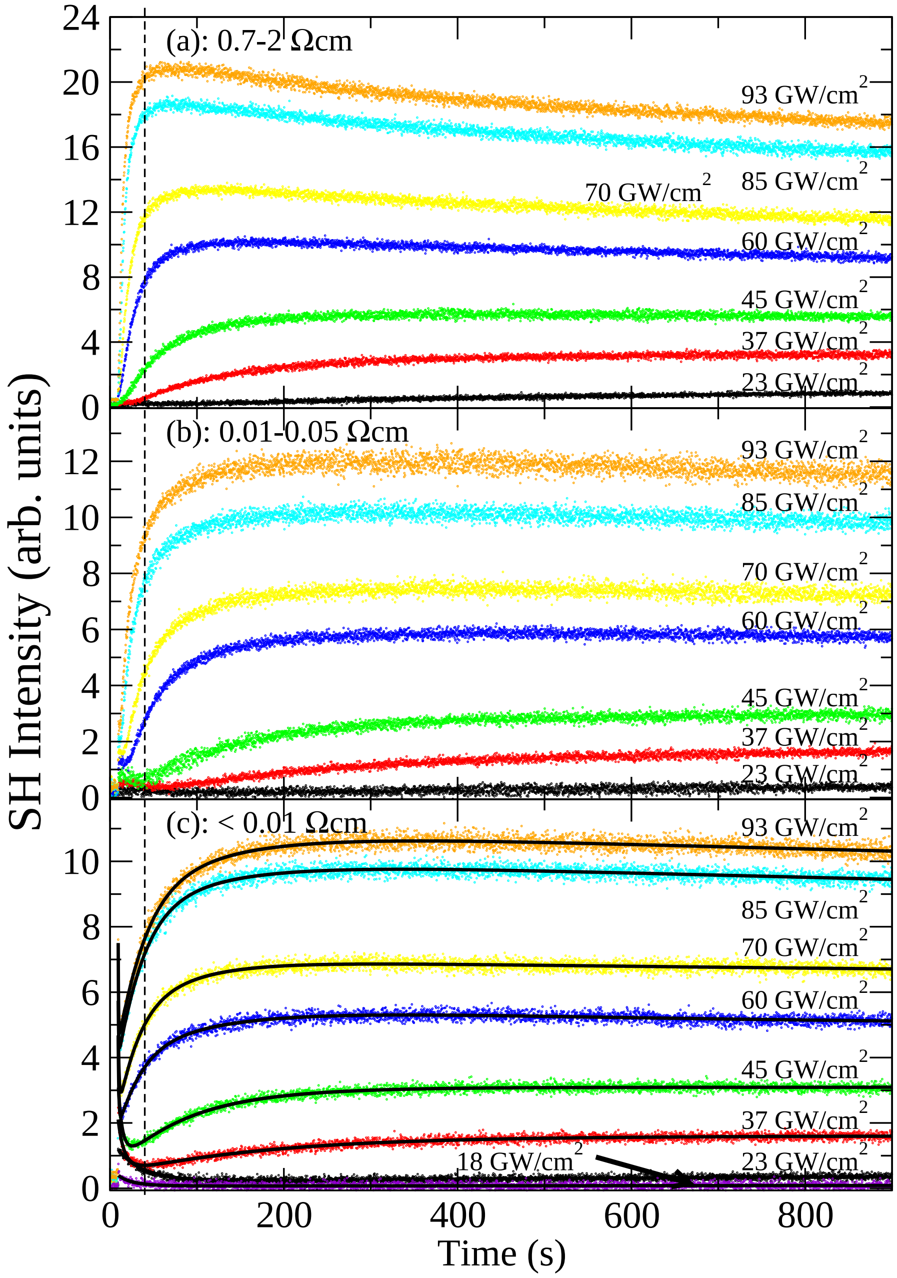

FIGURE 4.7: Temporal SH response of natively oxidized p-type Boron doped Si(100) of different resistivities (doping concentrations): (a) 0.7 - 2 Ωcm ($6.3 \cdot 10^{15}$ - $2.1 \cdot 10^{16}$ cm^{-3}), (b) 0.01-0.05 Ωcm ($7.5 \cdot 10^{17}$ - $8.5 \cdot 10^{18}$ cm^{-3}) and (c) < 0.01 Ωcm ($> 8.5 \cdot 10^{18}$ cm^{-3}); the solid lines in (c) are fitting curves following Eq. 5.4 (see chapter 5)

other hand, the SH signal height after saturation (960 s) drops substantially the higher the Boron doping concentration. In Fig. 4.7 (b) the SH signal height after 960 s amounts to 66 % of the equivalent SH signal in Fig. 4.7 (a). For even higher Boron doping levels as seen in Fig. 4.7 (c), the saturation SH signal after 960 s drops to 59 % of the respective SH signal in Fig. 4.7 (a). Looking carefully at the SH response of strongly Boron doped native $\mathrm{Si/SiO_2}$, a further dramatic effect occurs for resistivities $< 0.05\ \Omega\mathrm{cm}$.

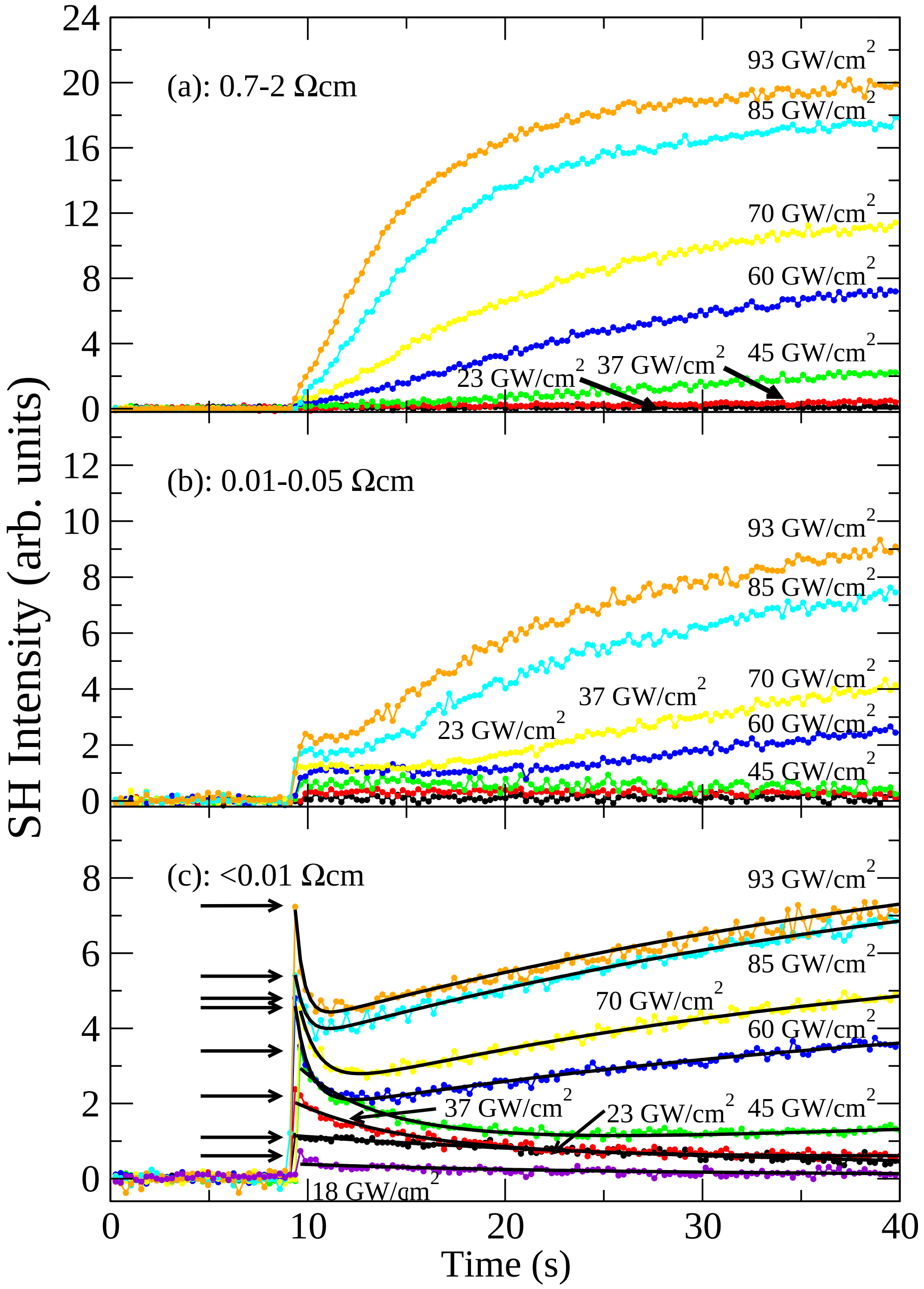

FIGURE 4.8: Temporal SH response of natively oxidized p-type Boron doped Si(100) for early times ($\leq$ 40 s): (a) 0.7-2 Ωcm ($6.3 \cdot 10^{15}$ - $2.1 \cdot 10^{16}$ cm^{-3}), (b) 0.01-0.05 Ωcm ($7.5 \cdot 10^{17}$ - $8.5 \cdot 10^{18}$ cm^{-3}), (c) $<$ 0.01 Ωcm ($> 8.5 \cdot 10^{18}$ cm^{-3}); the solid lines in (c) are fitting curves following Eq. 5.4.

Fig. 4.8 displays the data curves of Fig. 4.7 up to an irradiation time of 40 s (dashed line in Fig. 4.7) at a higher temporal resolution. The solid lines in Fig. 4.8 (c) are fitting curves according to Eq. 5.4. Whereas Fig. 4.8 (a) shows the expected temporal SH development also seen in Figs. 4.2 and 4.3, a non-vanishing instantaneous SH signal is observed in Figs. 4.8 (b) and (c). The height of this instantaneous SH signal increases with the incident laser peak intensity and becomes more pronounced the higher the Boron doping level (the lower the resistivity). As clearly seen in Fig. 4.8 (c), but also indicated in the intermediate doping regime in Fig. 4.8 (b), the instantaneous SH signal is followed by a decrease leading to a minimum. Only after this minimum the well known increase on a time scale of minutes is observed. The instantaneous SH signal found in strongly Boron doped $\mathrm{Si}/\mathrm{SiO}_2$, hence, counteracts the temporal evolution found in weakly doped $\mathrm{Si}/\mathrm{SiO}_2$.

Fig. 4.9 shows the temporal SH evolution of natively oxidized n-type Phosphorous (P) and Arsenic (As) doped Si(100) of various resistivities recorded at 28 $\mathrm{GW}/\mathrm{cm}^2$ incident laser peak intensity.

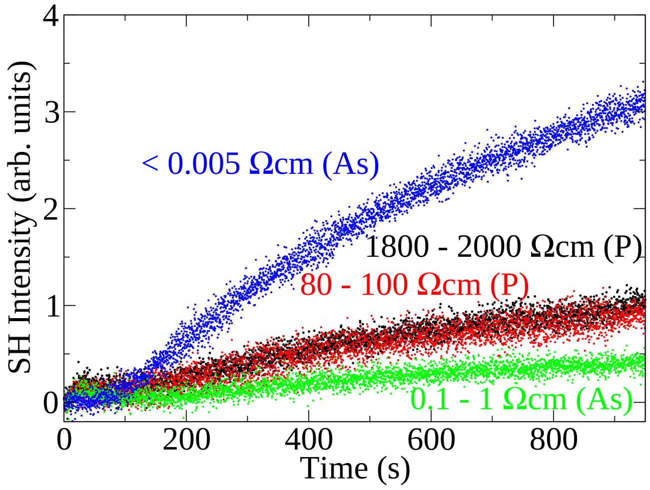

FIGURE 4.9: SH response of natively oxidized Phosporous (P) and Arsenic (As) doped Si(100) of various resistivities recorded at 28 $\mathrm{GW}/\mathrm{cm}^2$ incident laser peak intensity.

The curves recorded with $\mathrm{Si}/\mathrm{SiO}_2$ samples of resistivities (doping concentrations) of 1800-2000 $\Omega\mathrm{cm}$ ($\sim 10^{12}\mathrm{cm}^{-3}$) (P) and 80-100 $\Omega\mathrm{cm}$ $[(4.1-5.3)\cdot 10^{13}\mathrm{cm}^{-3}]$ (P) are very similar and show the well known SH increase with subsequent saturation. At 0.1-1 $\Omega\mathrm{cm}$ ($4.3\cdot 10^{15}\mathrm{cm}^{-3} - 7\cdot 10^{16}\mathrm{cm}^{-3}$) (As) a slightly smaller equlibrium SH signal is observed, whereas the curve recorded for a resistivity < 0.005 $\Omega\mathrm{cm}$ (As), which corresponds to doping concentrations $> 1.1\cdot 10^{19}\mathrm{cm}^{-3}$ shows a distinctly faster SH increase with a substantially higher equilibrium level. It is noted that none of the SH response curves of n-type doped $\mathrm{Si}/\mathrm{SiO}_2$ in Fig. 4.9 shows a dramatic instantaneous SH signal as observed in highly p-type Boron doped samples (Fig. 4.8).

4.4 SHG in UV Laser Pre-Irradiated Si/SiO$_2$

The aim of the experiments presented in this section is to separate the sample modification process from the SHG probing technique. In the first step, as described in section 3.4, an excimer laser source is used to irradiate native $\mathrm{Si/SiO_2}$ interfaces. In the second step, the UV irradiated sample spots are investigated by SHG employing femtosecond laser pulses. Time dependent SH measurements as well as SH imaging are employed. Lightly Boron doped samples (resistivity > 1000 $\Omega\mathrm{cm}$, Crystec, Berlin, Germany) are selected.

4.4.1 Time Dependent SH Response of UV Laser Pre-Irradiated Si/SiO$_2$

The temporal SH response of $\mathrm{Si/SiO_2}$ sample spots pre-exposed to UV excimer irradiation as described in section 3.4 is shown in Fig. 4.10 in comparison to the temporal SH evolution of virgin samples. The sample spots are pre-irradiated with a single excimer laser shot of 20 mJ pulse energy and the temporal SH response is recorded in the low intensity regime at 41 $\mathrm{GW/cm^2}$ in Fig. 4.10 (a) as well as the high intensity regime at 86 $\mathrm{GW/cm^2}$ in Fig. 4.10 (b).

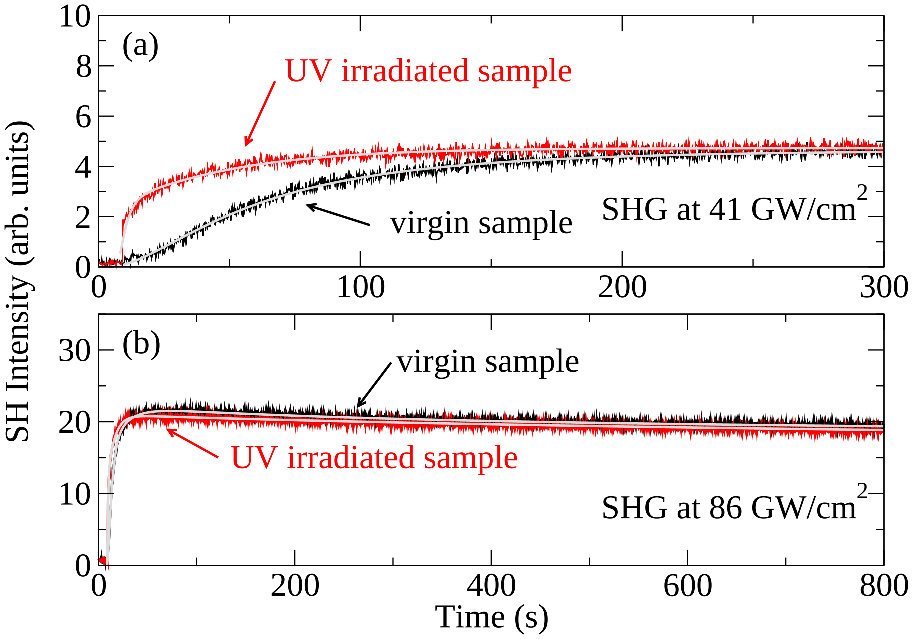

FIGURE 4.10: Temporal SH evolution of sample areas pre-irradiated with a single excimer laser UV pulse (16 ns, 308 nm, 20 mJ) in comparison to that of a related virgin sample. SH response curves are recorded at 41 $\mathrm{GW/cm^2}$ (a) and 86 $\mathrm{GW/cm^2}$ (b); the solid lines are fitting curves following Eq. 5.1 (a) and Eq. 5.2 (b).

As clearly seen in Fig. 4.10 (a) the EFISH related temporal SH increase of the sample area pre-exposed to UV light appears to be accelerated in a similar fashion as in the case of pre-irradiation with NIR femtosecond laser pulses (Fig. 4.3). In contrast to this, Fig. 4.10 (b) indicates that the slow SH decrease over a time scale of minutes recorded at 86 $\mathrm{GW/cm^2}$ is comparable in virgin and UV pre-irradiated samples. Furthermore no SH signal enhancement is observed upon UV pre-irradiation opposite to the enhancement in the case of femtosecond pre-irradiation $> 45\ \mathrm{GW/cm^2}$.

It is noted that differences in the equilibrium SH signals of UV irradiated $\mathrm{Si/SiO_2}$ in comparison to the respective virgin samples are found. The SH response curves in Fig. 4.11 recorded at 41 $\mathrm{GW/cm^2}$ in different samples show in some cases both, larger (Fig. 4.11 (a)) as well as smaller equilibrium SH signals (Fig. 4.11 (b)) within the UV pre-irradiated areas as compared to the saturation SH signal of the respective virgin sample. The temporal SH evolution remains, however, accelerated relative to that of the virgin samples as seen from the curves in Figs. 4.11 (a) and (b).

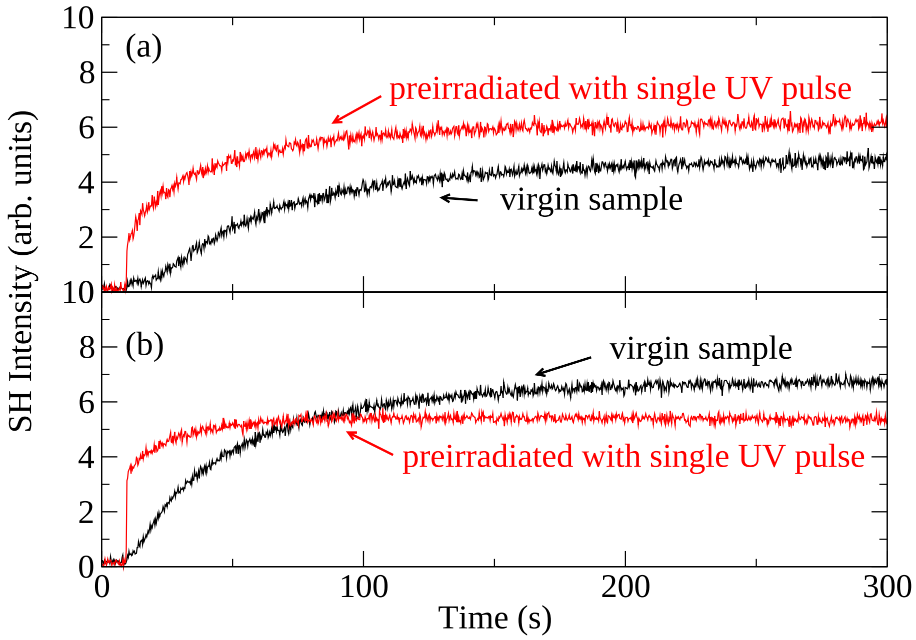

FIGURE 4.11: Temporal SH response of UV pre-irradiated sample areas recorded at 41 $\mathrm{GW/cm^2}$ showing larger (a) and smaller (b) equilibrium SH signal amplitudes as compared to the respective virgin sample.

Hence, it is found that excimer UV laser pre-irradiation leads to an accelerated SH signal increase in native $\mathrm{Si/SiO_2}$ interfaces for SHG at relatively low peak intensity. The SH decrease observed in the high intensity regime $> 45\ \mathrm{GW/cm^2}$ essentially remains unaffected by UV laser pre-irradiation.

4.4.2 SH Imaging of UV Laser Pre-Irradiated Spots

In the following, lateral SH imaging is used to visualize the UV pre-irradiated areas in native $\mathrm{Si/SiO_2}$. The spatial step resolution of all SH images is 60 μm in the X- and Y-directions. Dwell times of 0.2 s are employed at a peak intensity of 93 $\mathrm{GW/cm^2}$. In all experiments the spatial energy distribution of the applied UV pulses is satisfactorily approximated by the elliptic Gauss profile described by Eq. 3.12 with a 1/e-width of 1.1 mm.

In a first set of experiments the observed UV photoinduced sample modification process is investigated as a function of the applied excimer laser pulse energy. Fig. 4.12 shows 3D plots of sample areas in native $\mathrm{Si/SiO_2}$ pre-exposed to single excimer laser pulses of 3.6 mJ (a) to 20 mJ (h). The approximately elliptic energy distribution of the applied UV pulses is reflected in the shape of the pre-irradiated sample areas.

The series of SH images in Fig. 4.12 shows two decisive features. Firstly, the observed maximum signal heights in Figs. 4.12 (a) - (h) are essentially equal irrespective of the applied UV pulse energy and the SH images show a flat top shape with a plateau of an approximately constant average SH signal height of 6-7 arb. units. Secondly, it is found that the widths of the UV modified sample areas increase with the applied excimer laser pulse energy. For values from 3.6 mJ up to 8.4 mJ (Fig. 4.12 (a) - (e)) the increase is clearly visible. The widths are extracted across the long axis of the elliptic shape of the UV modified area and grow from 0.31 mm (a) over 0.50 mm (b), 0.59 mm (c) and 0.86 (d) up to the measured 1/e-width of the excimer laser pulse of 1.1 mm (e). For even higher UV pulse energies of 10 mJ (f), 16 mJ (g) and 20 mJ (h) the width increase of the UV modified areas from 1.15 mm (f) to 1.26 mm (g) and 1.32 mm (h) is less significant.

In a second set of experiments $\mathrm{Si/SiO_2}$ samples are repetitively exposed to excimer laser pulses of constant energy. The four SH images presented in the 3D plots in Fig. 4.13 show sample areas modified using a single excimer laser pulse of 3.2 mJ energy (a), 3 pulses (b), 5 pulses (c), and 10 pulses (d). Again two features are clearly observed in the series of SH images in Fig. 4.13. Firstly, the maximum SH signal height increases with the number of excimer laser pulses of 3.2 mJ energy applied for UV photoinduced sample modification. Secondly, the width of the UV modified area grows with the multiple application of excimer laser pulses (1 - 10 pulses).

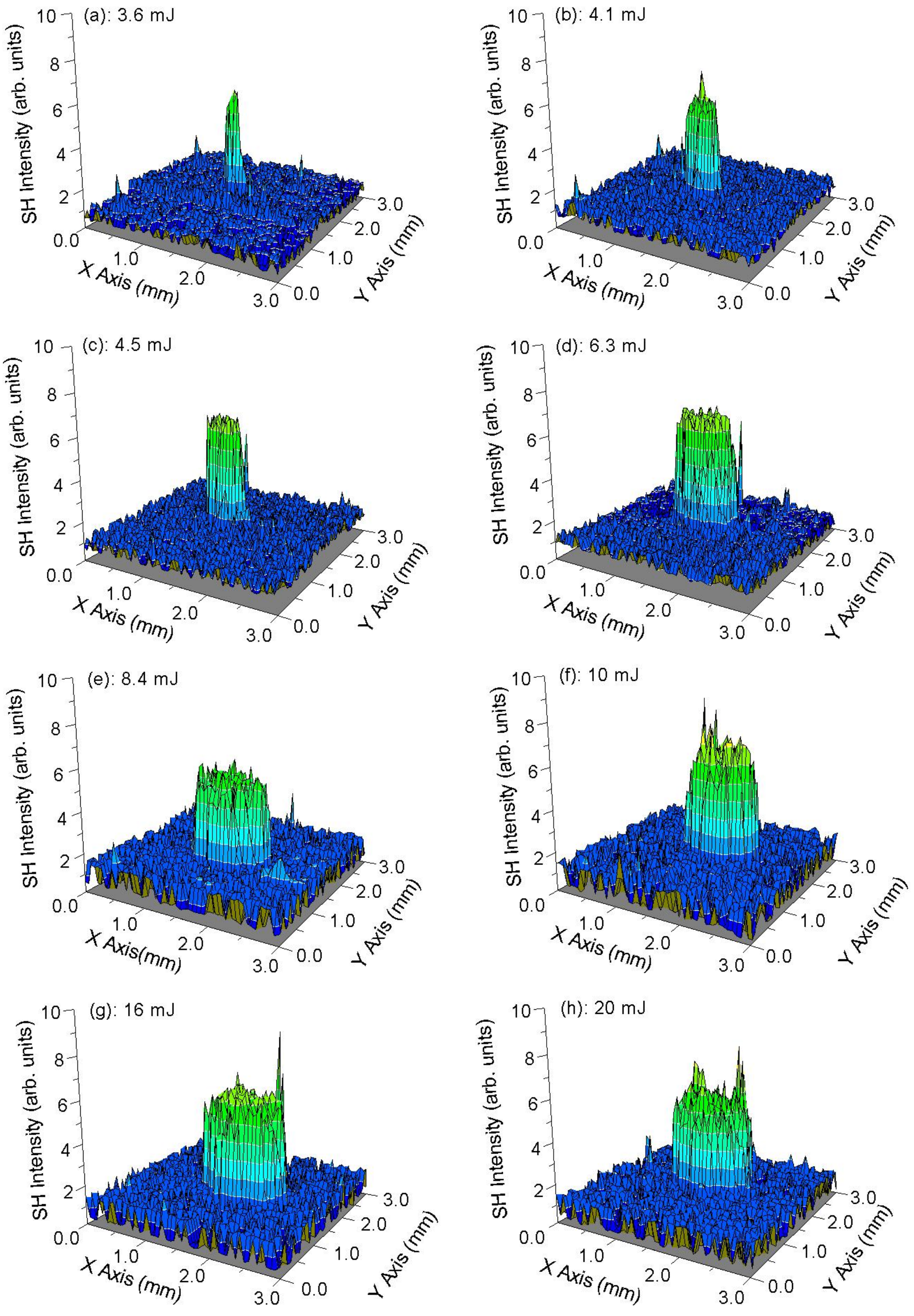

FIGURE 4.12: 3D SH images of sample areas in native Si/SiO$_2$ pre-irradiated with single UV laser pulses (pulse duration: 16 ns, wavelength: 308 nm, 1/e-width in X-direction: 1.1 mm) of energies: (a): 3.6 mJ, (b): 4.1 mJ, (c): 4.5 mJ, (d): 6.3 mJ, (e): 8.4 mJ, (f): 10 mJ, (g): 16 mJ, (h): 20 mJ.

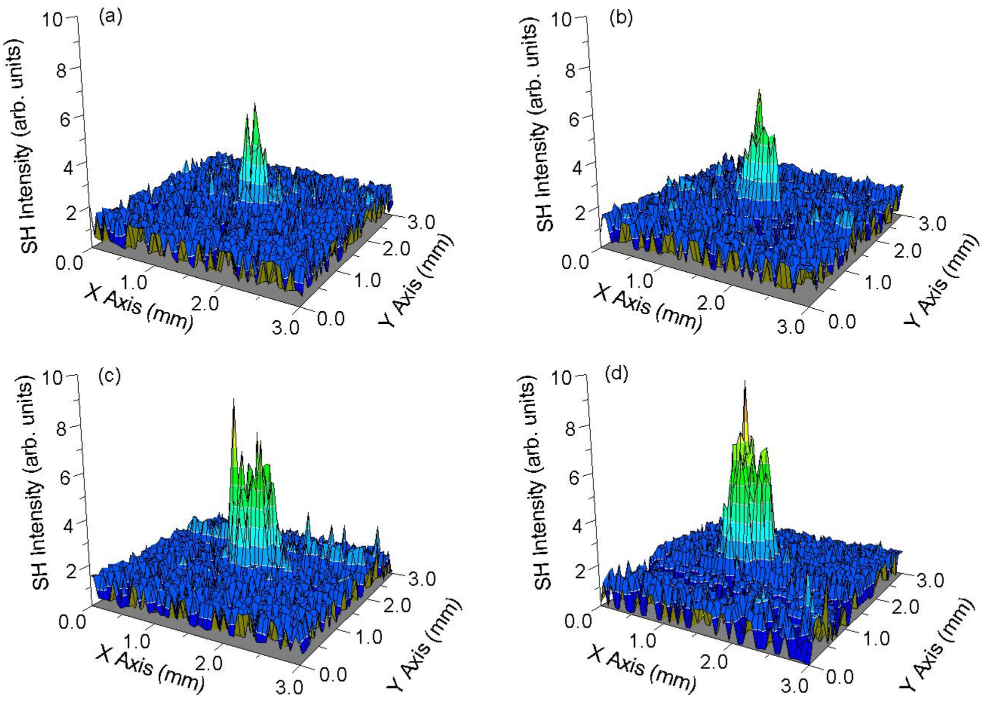

FIGURE 4.13: SH images of defect areas in native Si/SiO$_2$ generated by repetitive UV pulses (16 ns, 308 nm, 3.2 mJ): (a) single pulse, (b) 3 pulses, (c) 5 pulses and (d) 10 pulses.

Chapter 5

Discussion

In the following chapter the experimental findings are discussed. Microscopic physical mechanisms are proposed in order to consistently explain the experimental observations. Numerical models are developped to quantitatively reproduce the experimental data and support the proposed physical interpretation.

5.1 SH Signal Evolution in Virgin Si/SiO_2

The SH response curves of the $\mathrm{Si/SiO_2}$ interface recorded at 18 and 23 $\mathrm{GW/cm^2}$ as shown in Figs. 4.2 (b) and 4.3 reproduce the results previously reported by other authors [77, 78, 94] in spite of inevitable differences in sample preparation and laser irradiation. They are interpreted in a well established picture based on results obtained by SHG as well as other methods such as tunneling microscopy [77–80, 92, 94, 95]. Figure 5.1 (a) compares a simplified schematic energy diagram of the non-irradiated $\mathrm{Si/SiO_2}$ interface [80] with that under NIR femtosecond laser irradiation. Direct electronic excitation of the $\mathrm{SiO_2}$ layer is neglegible due to its large electronic band gap of 8.9 eV [80]. In bulk silicon hot electrons are generated by three-photon excitation or cascaded one- and two-photon processes (red arrows in Fig. 5.1 (b)). Their kinetic energy is sufficient to surmount the band offset of 4.3 eV [80] between the Si valence and the $\mathrm{SiO_2}$ conduction bands and electron injection into the $\mathrm{SiO_2}$ layer takes place. If the incident wavelength is in two-photon resonance with the interband transitions of the near interface or bulk silicon, such as the $\mathrm{E_1}$ critical point (3.3 eV), particularly efficient electron-hole pair creation takes place and the electron injection process observed by SHG is resonantly enhanced [63, 64, 89]. Electron trapping occurs with oxygen assistance at the $\mathrm{SiO_2/air}$ interface (A) [78], in the bulk $\mathrm{SiO_2}$ (B) and at the $\mathrm{Si/SiO_2}$ interface (C) [80]. The resultant charge separation leads to an internal electric field $\mathrm{E_{int}}$ (blue arrow in Fig. 5.1) across the $\mathrm{Si/SiO_2}$ interface, band bending at the interface and a space charge region (SCR). The interfacial electric field $\mathrm{E_{int}}$ exceeds 10^4 V/cm in ultrathin oxides for surface charge densities (Eq. 2.53)

$> 10^{12}\ \mathrm{cm}^{-2}$, which are realistic for the intensities employed here [80]. This is sufficient to yield measurable electric field induced changes in the observed SH signal [76–78]. The temporal evolution of the SH signal hence reflects the charge separation process.

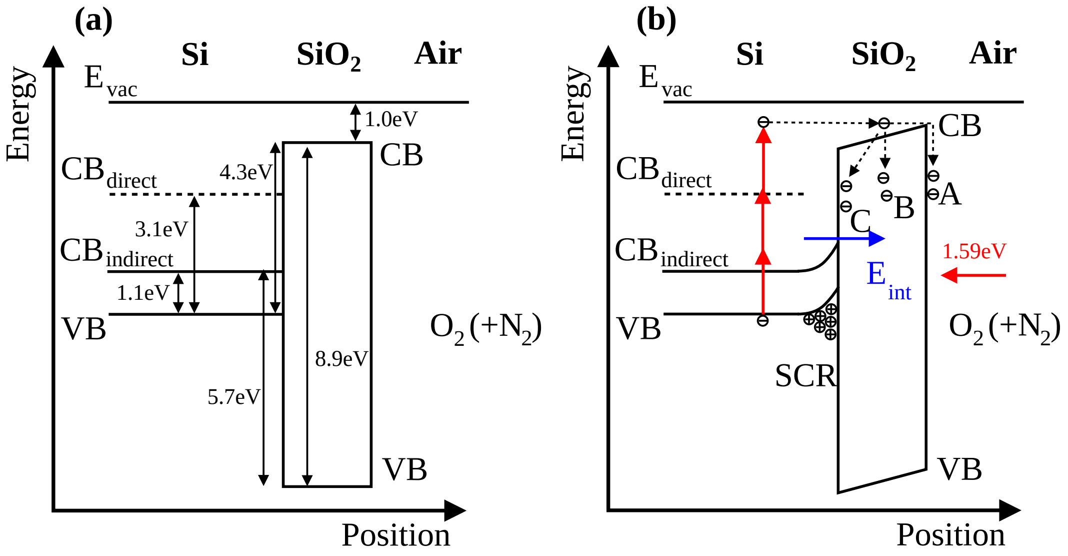

FIGURE 5.1: Schematic energy band diagram of the Si/SiO$_2$ interface without (a) and with (b) laser irradiation of $\leq$ 45 GW/cm^2; CB: conduction band, VB: valence band, E$_{\mathrm{vac}}$: vacuum energy level [80]; electron injection into SiO$_2$ by three-photon and cascaded one- and two-photon processes; electron trapping at SiO$_2$/air interface (A), in the bulk SiO$_2$ (B) and at the Si/SiO$_2$ interface (C); photoinduced internal electric field E$_{\mathrm{int}}$; band bending at the Si/SiO$_2$ interface and establishment of space charge region (SCR).

For intensities $\leq$ 45 GW/cm^2 the temporal evolution of the SH signal upon irradiation can be reproduced by fit curves (Fig. 4.2 (b)) using a biexponential relation (Eq. 5.1) proposed by Mihaychuk *et al.* [77, 80] involving the two-trap model

$$I^{(2\omega)}(t) \propto (1 + a_1 \exp(-t/\tau_1) + a_2 \exp(-t/\tau_2))^2 \tag{5.1}$$

with $a_i < 0$ and $\tau_i > 0$. The time constants τ_1 and τ_2 are dependent on the incident laser peak intensity $I_{l,p}$ following the power law $1/\tau_i(I_{l,p}) \propto I_{l,p}^{n_i}$, with $n_1 = 2.9$ and $n_2 = 2.5$ as shown in Fig. 5.3. These are in good agreement with the literature values of $n_1 = (2.8 \pm 0.2)$ and $n_2 = (2.5 \pm 0.3)$[77]. The deviations from a pure third order intensity dependence expected for three-photon excitation processes is explained by cascaded one- and two-photon electron excitation processes taking place in silicon, since the recombination times for electron hole pairs in silicon by far exceed the time between two laser pulses of 12.5 ns at 80 MHz repetition rate.

For peak intensities $> 45\ \mathrm{GW/cm^2}$ and exposure times of several minutes as shown in Fig. 4.2 (a) the temporal evolution of the SH response cannot solely be reproduced by the above mentioned two-trap model. Two additional processes involving hole dynamics are proposed and discussed in the following. It is suggested that hole injection affects the SH response of the native Si/SiO$_2$ interface. The experimental data curves shown in Fig. 4.2 (a) are interpreted within the physical picture illustrated in Fig. 5.2.

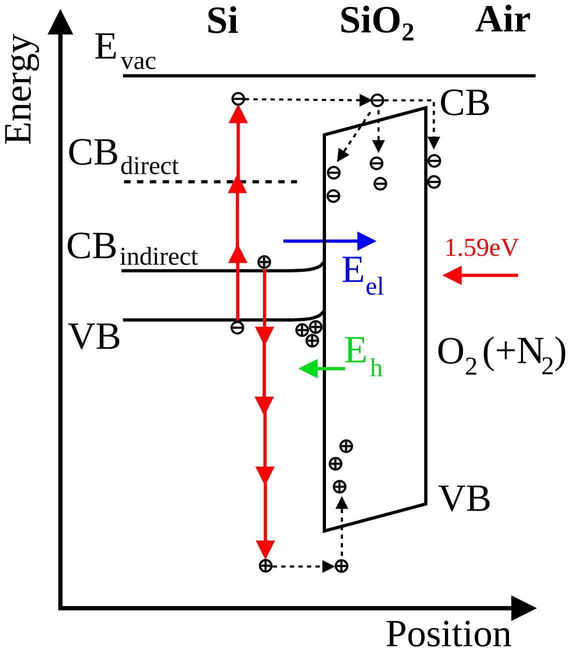

FIGURE 5.2: Schematic energy band diagram of the Si/SiO$_2$ interface under laser irradiation $> 45\ \mathrm{GW/cm^2}$ showing electron injection as in Fig. 5.1 (b) and in addition hole injection into SiO$_2$ by four-photon and cascaded one-, two- and three-photon processes; superposing electric fields from electrons (E_{el}) and holes (E_h) yield the transient net interfacial electric field reflected by the temporal SH evolution (Fig. 4.2 (a))

Hole injection has an energy barrier of 5.7 eV [80] (Fig. 5.1 (a)) and hence requires a four-photon excitation process, which supposedly becomes significant at high intensities as illustrated in Fig. 5.2. For a given incident peak intensity $> 45\ \mathrm{GW/cm^2}$ at first the electron effects are dominant in building up the interfacial electric field (increase in SH signal due to E_{el} in Fig. 5.2). The contribution of holes to the interfacial electric field (E_h in Fig. 5.2) is delayed due to the less efficient four-photon excitation and the low hole mobility. As a result, the SH signal representing the transient net surface charge density (superposition of electrons and holes) at the interface (Eq. 2.53) reaches a maximum after the initial increase and subsequently decreases very slowly (Figs. 4.2 (a), 4.3 and 5.6) due to the hole effects.

In order to numerically reproduce the observed SH response curves in Fig. 4.2 (a), the following empirical model (Eq. 5.2) is suggested using two additional exponential functions representing the hole induced effects in close analogy to the above two-trap electron model:

$$I^{(2\omega)} \propto \left(1 + \sum_{i=1}^{4} a_i \exp(-t/\tau_i)\right)^2 \tag{5.2}$$

This quantitative model (Eq. 5.2) represents a simple straight forward extension of the model by Mihaychuk *et al.* (Eq. 5.1) to numerically fit the recorded data, with $a_1, a_2 < 0$ and $a_3, a_4 > 0$. Fig. 5.3 shows the time constants τ_i as a function of the laser peak intensity in a double logarithmic plot.

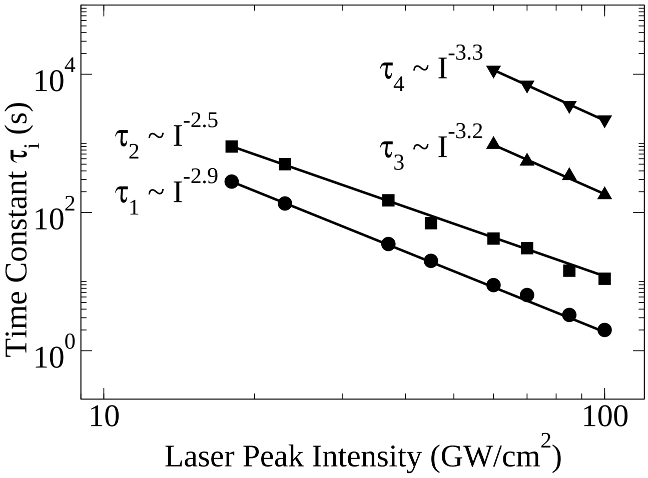

FIGURE 5.3: Time constants τ_1 to τ_4 as extracted from the numerical data fits in Fig. 4.2, according to Eqs. 5.1 and 5.2, respectively.

It is found that τ_1 and τ_2 follow the above $I_{l,p}^{n}$ intensity dependence up to 100 $\mathrm{GW/cm^2}$. τ_3 and τ_4 also follow a power law $1/\tau_i(I_{l,p}) \propto I_{l,p}^{n_i}$ with $n_3 = 3.2$ and $n_4 = 3.3$ indicating four-photon processes. The broken exponents deviating from pure fourth order intensity dependences are attributed to cascaded multiple one-, two- and three-photon hole excitation processes in analogy to the above described electron effects. The time constants related to the electron contributions of the SH signal evolution (τ_1 and τ_2) are found to be approximately two orders of magnitude smaller than τ_3 and τ_4 related to hole effects. Table 5.1 summarizes the extracted time constants τ_i for virgin $\mathrm{Si/SiO_2}$ samples.

Qualitatively similar results were reported recently by other authors [100] for zirconium modified $\mathrm{Si/(ZrO_2)_x(SiO_2)_{1-x}}$ interfaces. In that study hole contributions are found to affect the SH response of $\mathrm{Si/(ZrO_2)_x(SiO_2)_{1-x}}$ under NIR femtosecond laser irradiation at peak intensities $\geq 25\ \mathrm{GW/cm^2}$, whereas the SH response of native $\mathrm{Si/SiO_2}$ is solely governed by electron effects at these intensities. This observation is rationalized by taking into account the significantly lower conduction and valence band energy offsets in $\mathrm{Si/(ZrO_2)_x(SiO_2)_{1-x}}$ interfaces as compared to native $\mathrm{Si/SiO_2}$. Hence, two-photon and three-photon excitation processes are sufficient for electron and hole injection into the mixed oxide, respectively.

TABLE 5.1: Time constants τ_i for the SH signal evolution as a function of the incident laser peak intensity $I_{l,p}$ extracted from the numerical data fits (Figs. 4.2) for virgin $\mathrm{Si/SiO_2}$ (cf. text).

$I_{l,p}$ ($\mathrm{GW/cm^2}$)	τ_1 (s)	τ_2 (s)	τ_3 (s)	τ_4 (s)
18	330 ± 50	900 ± 100	-	-
23	130 ± 20	500 ± 50	-	-
37	35 ± 5	150 ± 20	-	-
45	20 ± 3	70 ± 7	-	-
60	9 ± 2	42 ± 6	$\sim$ 900	$\sim$ 11500
70	6.4 ± 1.0	31 ± 5	$\sim$ 580	$\sim$ 7000
85	3.3 ± 0.6	14.4 ± 3	$\sim$ 340	$\sim$ 3600
100	2.0 ± 0.5	11 ± 3	$\sim$ 180	$\sim$ 2200

Looking at the precise fitting curves in Fig. 4.2 and the time constants τ_1 to τ_4 in Table 5.1, a consistent picture of the EFISH evolution as a function of the applied laser peak intensity has been achieved. Beyond the previously reported results at low laser intensity ($\leq$ 45 $\mathrm{GW/cm^2}$) a new phenomenon is observed in $\mathrm{Si/SiO_2}$ at high intensities, which can be rationalized by hole induced EFISH contributions involving four-photon excitation. These processes are simulated in close analogy to the established two-trap model for the electron effects. The intensity dependences of the time constants τ_i indicate three- and four-photon induced excitation of electrons and holes in silicon, respectively, in agreement with the energy band diagrams of the $\mathrm{Si/SiO_2}$ system.

5.2 SH Signal Evolution in Pre-Irradiated Si/SiO$_2$

In comparison with virgin samples, the temporal SH evolution of pre-irradiated $\mathrm{Si/SiO_2}$ shows an accelerated dynamic behaviour upon re-irradiation after dark periods A to G in Fig. 4.3. In the low intensity regime < 37 $\mathrm{GW/cm^2}$, the SH signal recovers within seconds to its previous equilibrium level and confirms former results reported by other authors [94]. For high intensities > 45 $\mathrm{GW/cm^2}$ the SH signal increases within $\leq$ 0.2 s (time resolution of experimental setup) and reaches a maximum SH signal amplitude greater than the previous equilibrium level. The magnitude of this enhanced SH signal amplitude (empty circles in Figs. 4.3 and 5.6) increases with the duration of the dark period until about 600 s. Longer irradiation interrupts have no additional effect. The subsequent SH signal decrease to its equilibrium level takes place on a drastically shortened time scale as compared to the related signal decrease of virgin samples.

As a straight forward approach, the temporal SH response curves for pre-irradiated samples are simulated using the above successful numerical model involving a superposition of electron and hole effects. The experimental SH signals obtained for pre-irradiated samples can be reproduced by this model as shown by the fitting curves in Fig. 4.3 after dark period G. Eq. 5.1 is used in the low intensity regime < 37 $\mathrm{GW/cm^2}$ and Eq. 5.2 for the intermediate intensities up to 45 $\mathrm{GW/cm^2}$. In the high intensity regime > 45 $\mathrm{GW/cm^2}$ Eq. 5.2 with a_1 = a_2 = 0 is applied, since the electron dynamics are faster than the experimental time resolution of 0.2 s. Table 5.2 summarizes the extracted time constants τ_i^p for the pre-irradiated samples.

TABLE 5.2: Summary of the time constants τ_i^p as a function of the laser peak intensity $I_{l,p}$ extracted from numerical data fits (Fig. 4.3) for pre-irradiated $\mathrm{Si/SiO_2}$ samples.

$I_{l,p}$ ($\mathrm{GW/cm^2}$)	τ_1^p (s)	τ_2^p (s)	τ_3^p (s)	τ_4^p (s)
18	1.0 ± 0.7	7 ± 4	-	-
23	1.0 ± 0.7	8 ± 5	-	-
37	0.3 ± 0.2	2.5 ± 1	-	-
45	≈ 0.2	1.3 ± 1	~ 40	~ 120
60	< 0.2	< 0.2	~ 26	~ 200
70	< 0.2	< 0.2	~ 15.4	~ 81
85	< 0.2	< 0.2	~ 19	~ 195
100	< 0.2	< 0.2	~ 13.6	~ 104

All four time constants τ_i^p ($i = 1..4$) are much smaller in pre-irradiated samples than in virgin $\mathrm{Si/SiO_2}$. Fig. 5.4 shows the time constants τ_i^p for pre-irradiated samples as a function of the incident laser peak intensity in a double logarithmic plot. The ratios τ_i/τ_i^p between the respective time constants for virgin and pre-irradiated samples amount to about $10^2 - 10^3$ showing the strongly accelerated charge carrier dynamics in pre-irradiated $\mathrm{Si/SiO_2}$ as compared to virgin samples.

However, these time constants τ_i^p obtained for pre-irradiated samples show complex non-monotonic intensity dependences (Fig. 5.4), which cannot be attributed to well defined multiphoton excitation processes. This fact clearly points out that the simple two-trap model for electrons as well as holes (Eq. 5.2) introduced for virgin samples is not applicable to pre-irradiated samples.

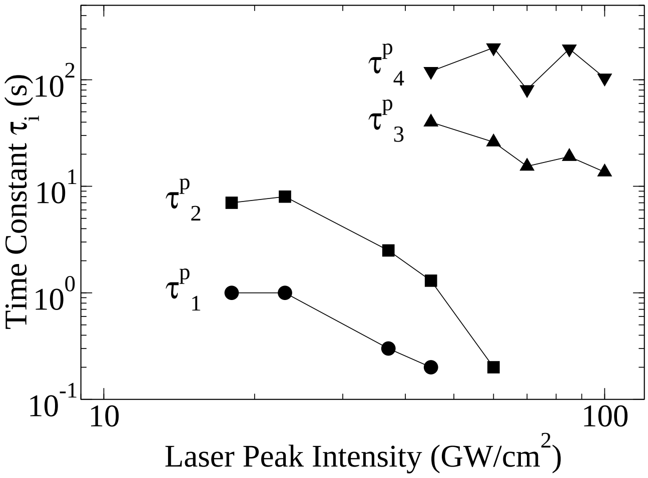

FIGURE 5.4: Time constants τ_1^p to τ_4^p for pre-irradiated Si/SiO$_2$ samples as extracted from the numerical data fits in Fig. 4.3, according to Eqs. 5.1 and 5.2, respectively.

The accelerated electron and hole dynamics observed in pre-irradiated Si/SiO$_2$ samples are explained by the photoinduced generation of electron and hole trap sites at the Si/SiO$_2$ interface taking place under NIR femtosecond laser irradiation. Fig. 5.5 shows a schematic energy band diagram including photogenerated electron as well as hole traps characteristic for pre-irradiated Si/SiO$_2$ samples.

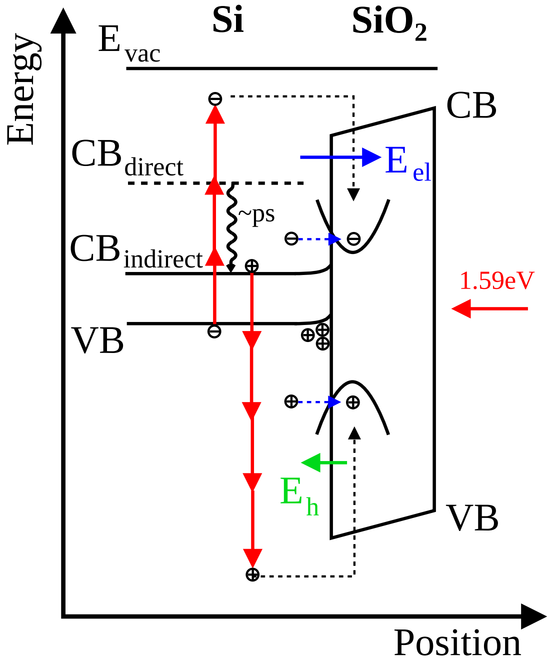

FIGURE 5.5: Schematic energy band diagram for pre-irradiated Si/SiO$_2$ samples, involving photogenerated electron as well as hole traps located close to the Si/SiO$_2$ inteface. Blue dashed arrows indicate proposed direct population mechanisms.

The photoinduced trap generation mechanisms are presumably initiated by hot electrons as well as holes, which upon injection into the SiO$_2$ layer have kinetic excess energies of $\sim$ 0.5 and $\sim$ 0.7 eV, respectively. Photoinduced traps are assumed to show essentially different characteristics than existing traps present in Si/SiO$_2$ natively oxidized at room

temperature (thermal energy $kT \sim$ 25 meV). They are assumed to be located close to the $\mathrm{Si/SiO_2}$ interface at relatively low energetic levels. It is argued that photogenerated traps have different cross sections for charge carrier capture as well as other detrapping times than natively created trap sites in $\mathrm{Si/SiO_2}$.
This qualitative physical picture (Fig. 5.5) suits to rationalize the accelerated electron and hole separation processes observed in pre-irradiated samples. A large density of photoinduced electron and hole traps is present in the $\mathrm{Si/SiO_2}$ sample after pre-irradiation leading to accelerated charge carrier separation processes as reflected by the time constants τ_i^p in Fig. 5.4 and Table 5.2. The breakdown of the defined power law dependences of the τ_i^p (Fig. 5.4) is viewed as an indication that direct photoinduced population mechanisms (blue dashed arrows in Fig. 5.5) are possible for photogenerated traps, which do not require multiphoton processes and dominate the temporal EFISH development in pre-irradiated $\mathrm{Si/SiO_2}$ samples. This seems plausible considering the presumed energetic levels of photogenerated traps as well as their vicinity to the $\mathrm{Si/SiO_2}$ interface.

5.3 Deconvolution of e$^-$ and h$^+$ EFISH Contributions

The results discussed in the previous section 5.2 show that electron injection and trapping in pre-irradiated $\mathrm{Si/SiO_2}$ at incident laser peak intensities > 45 $\mathrm{GW/cm^2}$ occurs on a time scale in the order of the experimental time resolution of 0.2 s. Hole injection and trapping is at least one order of magnitude slower (Table 5.2). This finding allows to separate electron and hole EFISH contributions. The SH signal amplitude observed upon re-irradiation after dark period G (empty circles in Fig. 4.3) is attributed to the pure electron effect representing the status with saturated interfacial electron trap population and neglegible hole trap population. The subsequent SH signal decrease to the equilibrium level is attributed to the pure hole contribution. These contributions are illustrated in Fig. 5.6 by vertical arrows indicating the pure $\mathrm{e^-}$ and $\mathrm{h^+}$ effects. The SH response curve shown in Fig. 5.6 represents that signal in Fig. 4.3 which was recorded at 100 $\mathrm{GW/cm^2}$.

Following these considerations, the steady state electron and hole densities can be deconvoluted (Fig. 5.6). According to Eq. 2.53 the interfacial charge carrier density is proportional to the square root (SQRT) of the observed SH intensity. The inset in Fig. 5.6 shows the square root of the pure electron SH contribution SQRT SH($\mathrm{e^-}$) as well as the pure hole contribution SQRT SH($\mathrm{h^+}$) versus the laser peak intensity. Both, SQRT SH($\mathrm{e^-}$) and SQRT SH($\mathrm{h^+}$), being a measure for the interfacial electron and hole densities are proportional to the laser peak intensity (inset of Fig. 5.6) following Eqs. 2.52 and 2.53.

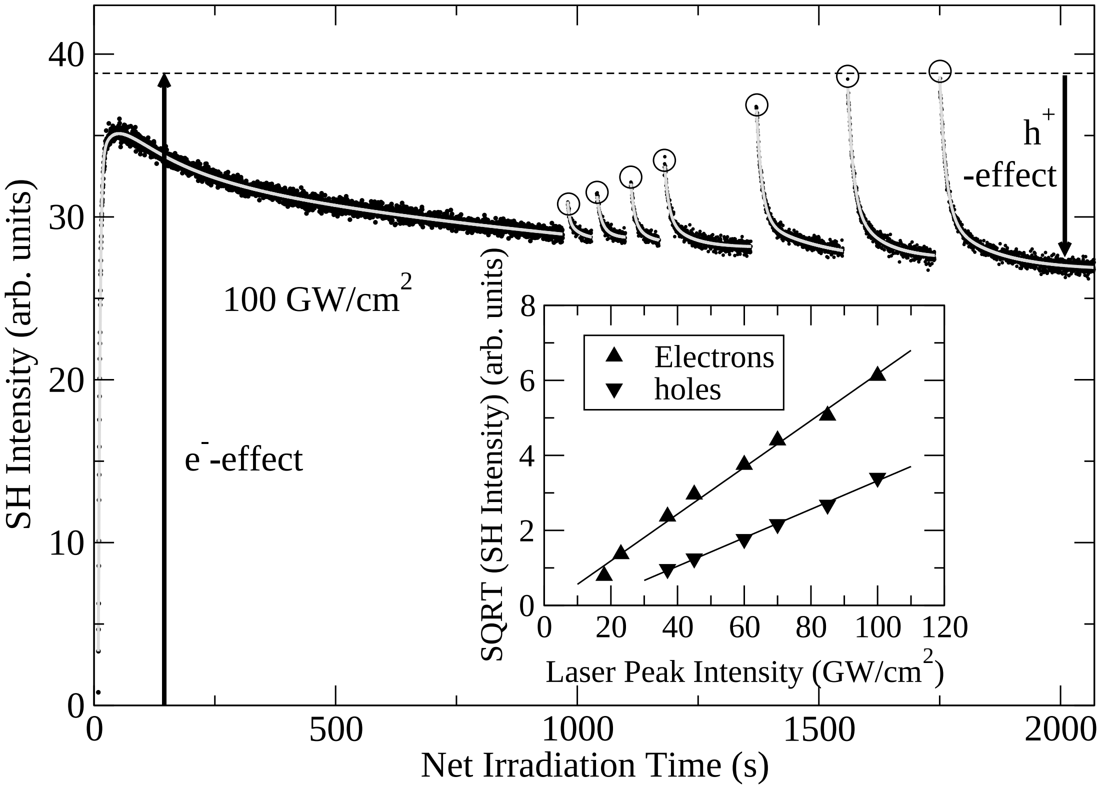

FIGURE 5.6: Deconvolution of temporal SH signal development at 100 GW/cm^2 irradiation (curve from Fig. 4.3) with respect to electron and hole induced effects; the solid lines are fitting curves according to Eq. 5.2; the inset shows the equilibrium electron and hole densities (square root (SQRT) of SH signal amplitudes, cf. Eq. 2.53) as a function of the laser peak intensity.

The different slopes show that the efficiency of the photoinduced charge transfer process into SiO_2 is higher for electrons than for holes.

5.4 Relaxation during Dark Periods

As discussed in the previous sections 5.1 - 5.3 and illustrated in Fig. 5.6, the SH signal increase during irradiation is attributed to electron induced effects, whereas the SH signal decrease is attributed to hole effects. The equilibrium SH signal is a superposition of two opposing contributions (electrons and holes) to the interfacial electric field. During the dark periods electrons as well as holes diffuse out of their traps. Electron detrapping occurs within 80-100 s [77, 94] and hole detrapping is probably slower (minor mobility). The experimental finding in Fig. 4.4 rules out the presence of a residual interfacial elec-

tric field in $\mathrm{Si/SiO_2}$ for dark period durations $\geq$ 600 s. This implies that the sample can be assumed to be electrically neutral after relaxation times of 600 s or longer. The SH signal evolution within dark periods of durations $\leq$ 600 s, however, represents the charge carrier relaxation dynamics. For a given dark period < 600s a time dependent distribution of electrically neutral and charged traps for electrons and holes is present in $\mathrm{Si/SiO_2}$.
As described above, photoinduced electron injection into $\mathrm{SiO_2}$ in pre-irradiated samples at high laser intensity (> 45 $\mathrm{GW/cm^2}$) is fast relative to the time resolution of the experiments described here. Therefore, the SH signal maxima achieved upon re-irradiation (empty circles in Figs. 4.3 and 5.6) represent the status with all previously filled electron traps being refilled by laser injected electrons. Hole injection into $\mathrm{SiO_2}$, on the other hand, is significantly slower (Table 5.2 and Fig. 5.4). Therefore it is argued that irrespective of the duration of the preceeding irradiation interrupts A to G in Fig. 4.3 the SH signal maximum achieved upon re-irradiation always represents the status of saturated interfacial electron trap population. Hence the height of the SH enhancement upon re-irradiation is a measure for the residual interfacial field due to residual holes trapped at the $\mathrm{Si/SiO_2}$ interface. It hence reflects the effect of hole diffusion out of their traps during the preceeding dark period. The systematic investigation of the SH enhancement as a function of the dark period duration thus yields the characteristic time constant for hole detrapping.

Fig. 5.7 (a) shows the square root (SQRT) of the SH signal amplitude achieved immediately after unblocking the laser beam (empty circles in Figs. 4.3 and 5.6) versus the dark period duration for the curves recorded at 70, 85 and 100 $\mathrm{GW/cm^2}$. According to Eq. 2.53 the SQRT of the SH signal is proportional to the interfacial charge density. Hence, the data in Fig. 5.7 represent the dark period dependent change of the interfacial density of populated hole traps and are reproduced by the simple exponential function

$$\sqrt{I^{(2\omega)}(t)} \propto n_c(t) = const + I_0^{(2\omega)} \cdot (1 - exp(-t/\tau_{h-detrap})) \qquad (5.3)$$

as shown by the solid lines in Fig. 5.7 (a). Fig. 5.7 (b) shows a single logarithmic plot of the exponential term in Eq. 5.3 based on the same data. The temporal evolution of the interfacial hole density hence follows a simple exponential decay and the detrapping time constant $\tau_{\mathrm{h-detrap}}$ = (110 ± 15) s for holes is equal for all three laser peak intensities. This confirms the above argumentation, since detrapping under dark conditions is expected to be independent of the initial density of populated traps determined by the laser intensity.

Very recently experiments on electron and hole injection into the $\mathrm{SiO_2}$ layers were reported using a low pressure Hg/Ar UV lamp of wavelengths 254 nm (4.9 eV) and 185 nm (6.7 eV) [126]. In those experiments SHG using NIR femtosecond laser pulses is employed to probe the UV induced charge carrier separation processes across the $\mathrm{Si/SiO_2}$

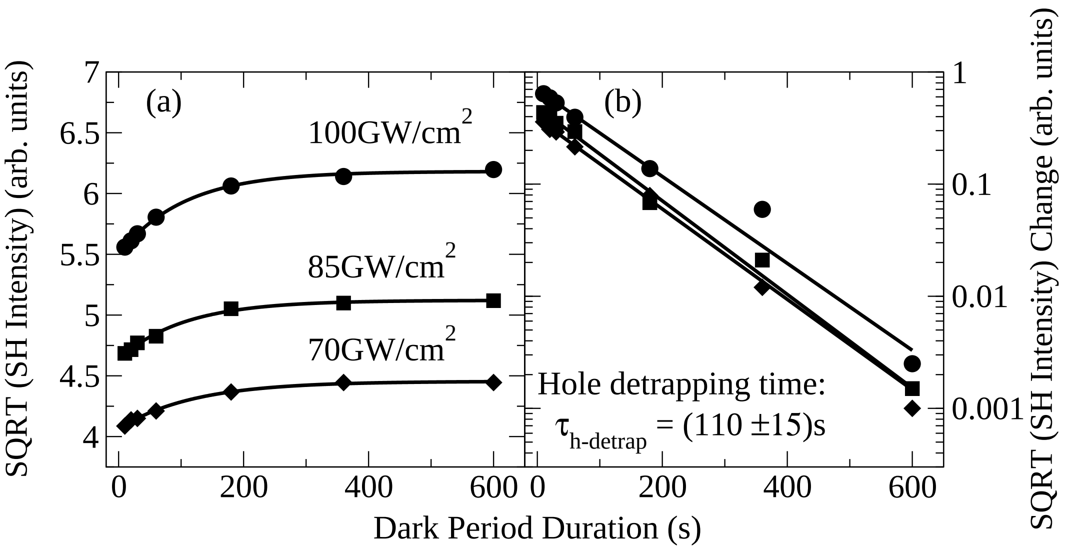

FIGURE 5.7: (a): SH intensity immediately after restart of laser irradiation taken from the curves recorded for 70, 85 and 100 GW/cm^2 (indicated by circles in Figs. 4.3 and 5.6) versus dark period duration; the solid lines represent an exponential fit (Eq. 5.3). (b): Single logarithmic plot of the exponential term in Eq. 5.3 based on the same data as in (a); the fit curves (solid lines) yield equal slopes for the different laser intensities corresponding to the detrapping time for holes of 110 ± 15 s.

interface. The applied laser peak intensities for SHG are two orders of magnitude lower ($\sim$ 1 GW/cm^2) than the intensities used in this study. Hole injection and hole trap generation by femtosecond laser irradiation is hence not expected. The authors report on the UV induced population of hole traps in the SiO_2 layer, which show very long hole relaxation times of tens of hours. It is assumed that the traps populated in those experiments are natively created hole traps in Si/SiO_2, whereas the experiments performed here involve hole traps photogenerated under high intensity femtosecond laser irradiation of up to 100 GW/cm^2. As mentioned in section 5.2, photogenerated traps presumably show very different characteristics than native traps. This explains the drastic differences in relaxation times. It is particularly pointed out, that despite the similarity of the SH temporal evolutions observed in Ref. [126] for UV irradiated Si/SiO_2 samples and the curves shown in Fig. 4.3 after dark period G, the experimental finding shown in Fig. 4.4 rules out the existence of a residual interfacial electric field due to residual populated hole traps in pre-irradiated Si/SiO_2 for dark periods $>$ 600 s. This confirms the assumption that hole traps photoinduced in Si/SiO_2 by high intensity NIR femtosecond irradiation ($>$ 45 GW/cm^2) show a different relaxation behaviour than existing hole traps ionized by 6.7 eV UV irradiation.

5.5 SH Signal Evolution in Highly Doped Si/SiO$_2$

In the following, a self-consistent interpretation is proposed in order to explain the time dependent SH response curves obtained for p^+- Si/SiO_2, which are displayed in Figs. 4.7 and 4.8. This interpretation employs the above described superposition of electron and hole effects and, in addition, includes the doping related ionization of interface defect states resulting in near-interface band bending and, hence, in a built-in electric field across the native Si/SiO_2 interface.

5.5.1 Doping Related Ionization of Interface Defect States

At first the atomically clean silicon surface is considered. Fig. 5.8 shows a simplified schematic energy band diagram of substantially p-type doped silicon (p^+-Si) [123].

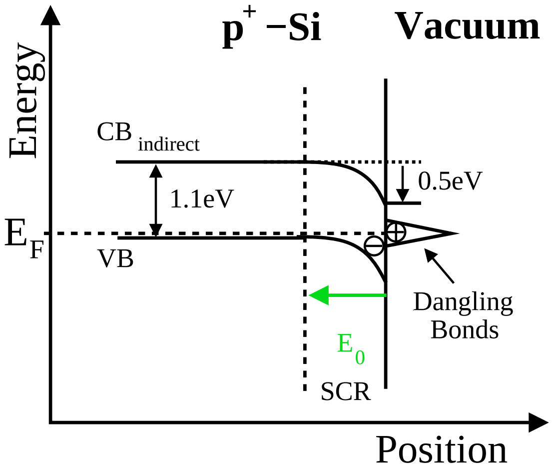

FIGURE 5.8: Schematic band diagram of the atomically clean p^+-doped silicon surface; near-surface band bending due to positively ionized dangling bond states. Fermi level (E_F) pinning at midgap, SCR: space charge region, E_0: internal electric field.

Surface dangling bonds are energetically placed in the band gap in many cases of surface reconstruction [128]. It is well known that atomically clean silicon surfaces support electrically charged defects. Interstitials, for instance, are absorbed very efficiently in surface defect states inducing Fermi level pinning and near-surface band bending [123, 124, 128]. As a result a narrow space charge region (SCR) is established and an internal electric field E_0 points into the bulk semiconductor (Fig. 5.8). In order to globally pin the Fermi level at midgap, surface defect state densities in the order of 10^{10}-10^{11} cm^{-2} are required [128]. For substantial p-type doping concentrations the Fermi level lies close to the silicon valence band (VB) edge. Hence band bending in the order of 0.5 eV occurs at the surface (Fig. 5.8) [117, 123, 124] yielding an internal electric field E_0 high enough to change even the linear optical properties of the surface [117, 129]. Such internal electric fields should be readily observed by SHG.

Si/SiO$_2$ interfaces can be prepared remarkably free of electrically active defects by thermal growth techniques [117], which would imply a flat band condition at the interface as shown in Fig. 5.1 (a). Very recent experimental work showed that ion bombardment can induce controlled amounts of bond rupture at the Si/SiO$_2$ interface in the case of substantial Boron doping concentrations (10^{18} cm^{-3}) leading to band bending of a magnitude comparable to that of the atomically clean silicon surface [116, 117, 123, 124].

The natively oxidized Si/SiO$_2$ samples used for this study presumably show a significant density of incompletely saturated interfacial bonding configurations, which form interface defect states situated in the silicon band gap. Therefore, it is suggested that the energy band diagram of the p$^+$- Si/SiO$_2$ interface resembles the one representing the atomically clean p$^+$-silicon surface. The amount of band bending, however, depends on the density of ionized interface defect states and remains open to discussion. The proposed schematic energy band diagram of the p$^+$-doped Si/SiO$_2$ interface is shown in Fig. 5.9.

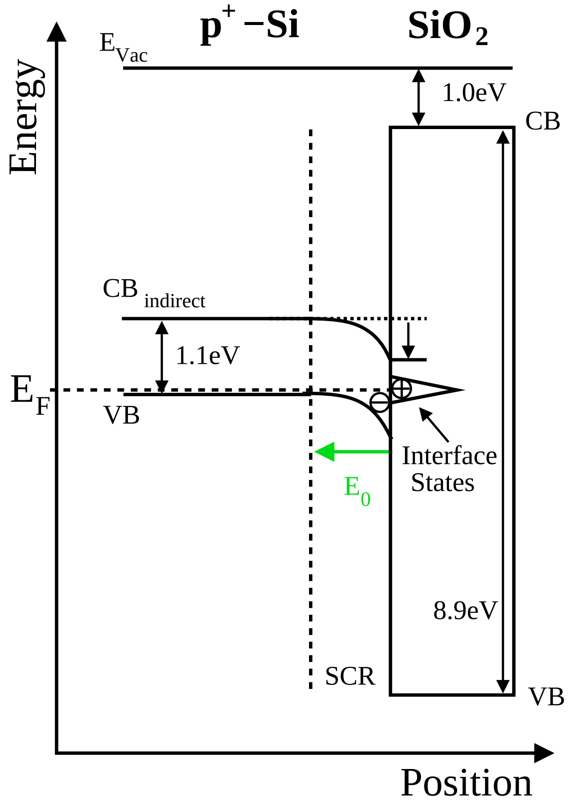

FIGURE 5.9: Schematic band diagram of p$^+$-Si/SiO$_2$; positive ionization of interface defect states, Fermi level (E$_F$) pinning; near-interface band bending; SCR: space charge region, built-in interfacial electric field E$_0$

Interfacial charge densities in the order of 10^{11} cm^{-2} corresponding to interfacial electric fields $> 10^4$ V/m are required to induce measurable changes in the interfacial SH response [76]. This implies that fractional interfacial defect coverages between 10^{-4} and 10^{-3} are necessary to achieve interfacial electric fields detectable by SHG under the applied conditions. Such fractional defect coverages appear reasonable for native Si/SiO$_2$.

Following the above considerations, the time dependent SH response curves observed in native p$^+$-Si/SiO$_2$ (Figs. 4.7 and 4.8) can be explained consistently employing the above proposed superposition of electron and hole effects (section 5.1) and taking into account the doping related built-in electric field E$_0$. Fig. 5.10 shows the schematic energy band diagram of the native p$^+$-Si/SiO$_2$ interface under NIR femtosecond laser irradiation.

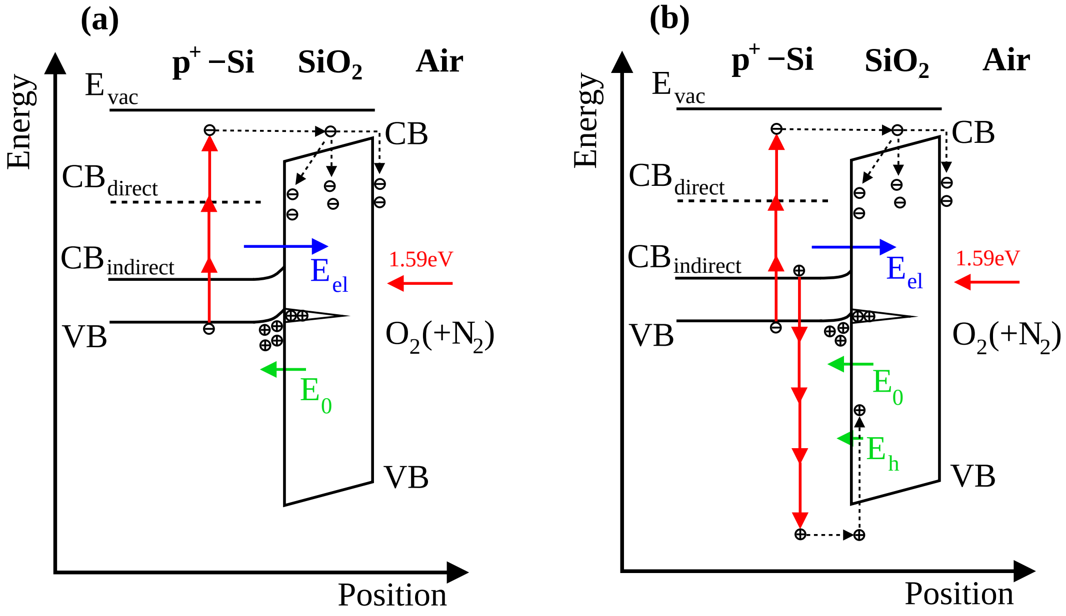

FIGURE 5.10: Schematic band diagram of the native p$^+$-Si/SiO$_2$ interface under NIR femtosecond laser irradation: (a): superposition of doping related built-in electric field E$_0$ and photoinduced interfacial electric field component E$_{el}$ due to electron injection and trapping. (b): additional weak contribution of photoinduced hole effects shown as interfacial electric field E$_h$; the observed transient SH signal probes the sum of all electric fields E$_0$, E$_{el}$ and E$_h$ (Eq. 2.52).

Fig. 5.10 (a) illustrates the superposition of the interfacial electric field component E$_{el}$ caused by the photoinduced electron effects and the opposing doping related built-in electric field component E$_0$. In addition, Fig. 5.10 (b) includes the photoinduced hole contributions yielding the interfacial field component E$_h$ under high intensity ($>$ 45 GW/cm^2) laser irradiation. The experimentally observed transient SH signal reflects the superposition of all interfacial electric fields E$_0$, E$_{el}$ and E$_h$, according to Eq. 2.52.

The temporal SH signal evolution of the natively oxidized silicon wafer of resistivity ρ = 0.7..2 Ωcm (Boron concentrations $n_B = 6.3 \cdot 10^{15}..2.1 \cdot 10^{16}$ cm^{-3}) displayed in Fig. 4.8 (a) shows no measurable instantaneous SH signal. Hence, it is assumed that band bending and the magnitude of the related built-in electric field E$_0$ are below the experimental SHG detection limit. In contrast to this, a clear instantaneous SH signal is observed in the case of ρ = 0.01..0.05 Ωcm (n_B = $7.5 \cdot 10^{17}$..$8.5 \cdot 10^{18}$ cm^{-3}) in Fig. 4.8 (b), which is even more pronounced for $\rho < 0.01$ Ωcm ($n_B > 8.5 \cdot 10^{18}$ cm^{-3}) in Fig. 4.8 (c). This instantaneous SH signal is observed in virgin samples and, therefore, cannot be related to the fast filling of photogenerated electron trap sites. Following the above argumentation the observed instantaneous SH signal is attributed to the doping related built-in electric field E_0 at the native Si/SiO$_2$ interface (Eq. 2.52). It appears that the interfacial SH response of native Si/SiO$_2$ begins to experience significant changes due the doping related built-in electric field E_0 for $n_B > 7.5 \cdot 10^{17}$ cm^{-3}.

With the built-in electric field E_0 present in native p$^+$-Si/SiO$_2$ as a starting condition, the temporal SH evolution observed in substantially Boron doped native Si/SiO$_2$ (Figs. 4.8 (b) and (c)) is explained by using the above introduced superposition of electron and hole effects. E_0 being due to the positive ionization of interface defect states points into the bulk silicon and opposes the interfacial electric field component induced by electron injection into the SiO$_2$ layers.

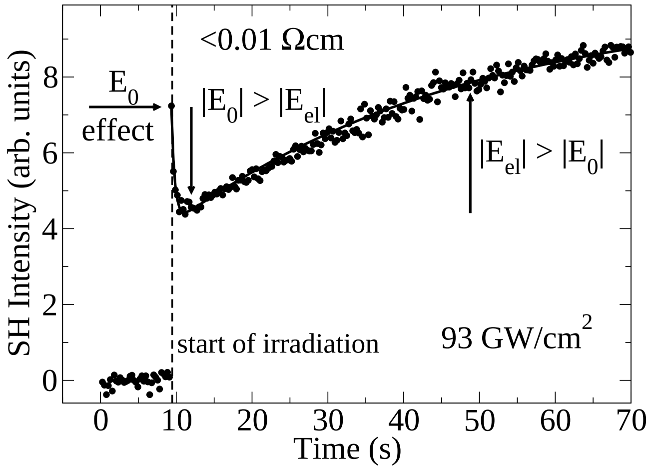

FIGURE 5.11: Temporal SH response curve of p$^+$-Si/SiO$_2$ taken from Fig. 4.8 (c); instantaneous SH signal due to doping related built-in electric field E_0; superposition with electric field E_{el} induced by electron transfer into SiO$_2$.

As an example for the SH response curves of p$^+$-Si/SiO$_2$ with $n_B > 8.5 \cdot 10^{18}$ cm^{-3}, Fig. 5.11 shows the temporal SH signal evolution recorded at 93 GW/cm^2 taken from Fig. 4.8 (c). Upon laser irradiation the instantaneously observed SH signal is followed by a SH signal decrease to a local minimum. This decrease is, hence, attributed to the photoinduced interfacial electron effects opposing the built-in field E_0. At the local minimum E_0 is compensated by the interfacial electric field E_{el} due to photoinduced electron effects. The finding that the SH signal does not vanish for $|E_0| = |E_{el}|$ can be explained by considering a phase shift between the approximately constant doping related field E_0 and the time dependent electron induced field E_{el} [95]. Further electron injection into the SiO$_2$ layers under continued laser irradiation leads to the subsequent SH increase after the local minimum up to SH signal saturation (Figs. 5.11 and 4.8 (c)).

The time dependent SH response curves recorded for longer time scales up to 960 s show a substantially decreased equilibrium SH signal height (after 960 s) for $n_B > 7.5 \cdot 10^{17}$ cm^{-3} in Fig. 4.7 (b) and (c) as compared to lower doping levels in Fig. 4.7 (a). This drop in the equilibrium SH signal amplitude observed for all applied peak intensities is attributed to the built-in electric field E_0. Figure 5.12 illustrates this argumentation by displaying the temporal SH response curves of the Si/SiO$_2$ samples with ρ = 0.7..2 Ωcm and ρ < 0.01 Ωcm recorded at 93 GW/cm^2 taken as examples from Figs. 4.7 (a) and (c), respectively. It is argued that in a first approximation E_0 remains unaffected by the laser irradiation. It opposes the photoinduced electron effects and consequently reduces the equilibrium SH signal height.

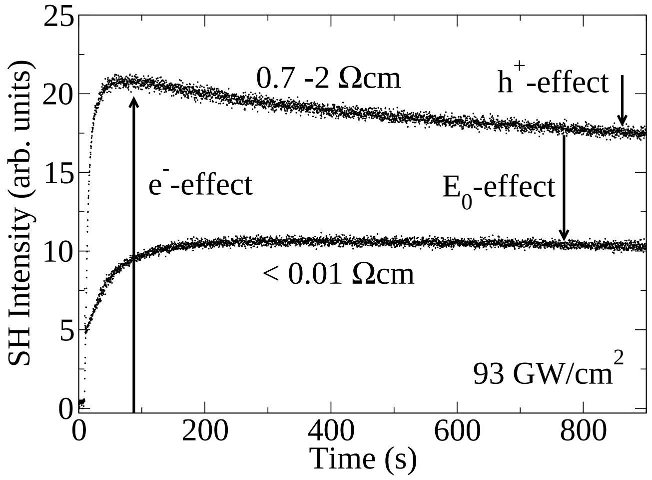

FIGURE 5.12: Temporal SH response curves of Si/SiO$_2$ taken from Figs. 4.7 (a) and (c); decreased equilibrium SH signal and less pronounced h^+ contribution in p^+-Si/SiO$_2$ due to the built-in electric field E_0;

The SH decrease on a time scale of many minutes in the high intensity regime > 45 GW/cm^2 is less pronounced in p^+- Si/SiO$_2$ as seen in Figs. 5.12, 4.7 (b) and (c) as compared to weakly doped samples in Figs. 5.12 and 4.7 (a). This leads to the assumption that the laser induced hole effects are significantly reduced by the positive ionization of the interface defect states. As argued above, a substantial density (> 10^{11} cm^{-2}) of interface defect states is positively ionized in native p^+-Si/SiO$_2$ interfaces before the laser irradiation. It seems plausible that laser induced hole trapping at the interface is hence significantly hampered, because a substantial density of hole trap sites is pre-ionized due to doping. Therefore, the SH signal decrease for incident peak intensities > 45 GW/cm^2 is significantly less pronounced in p^+-Si/SiO$_2$ (Figs. 5.12 and 4.7). This may be rationalized by assuming that photoinduced hole injection and trapping on the one hand and the doping related ionization of interfacial defects on the other hand are competing processes and both involve trap sites, which are located in close vicinity of the Si/SiO$_2$ interface.

The temporal SH response curves recorded in n-type doped native Si/SiO$_2$ interfaces for a peak intensity of 28 GW/cm^2 presented in Fig. 4.9 show no measurable instantaneous

SH signal and follow the well known SH increase with subsequent saturation. The curve recorded for the highest n-type doping concentration $> 1.1 \cdot 10^{19}$ cm^{-3} shows a faster SH increase and a higher equilibrium SH signal than that related to the lower n-type doping levels. This suggests that substantial n-type doping accelerates the interfacial electron dynamics in native $\mathrm{Si/SiO_2}$ under femtosecond laser irradiation. In n-type $\mathrm{Si/SiO_2}$ band bending would occur in the opposite direction as for p-type doping shown in Fig. 5.9. The observation that no significant instantaneous SH signal is observed in n$^+$-$\mathrm{Si/SiO_2}$ leads to the assumption that either no interface defect states are energetically available for the doping related trapping of electrons under Fermi level pinning at the interface or that the density of negatively ionized defect states is below the detection limit for SHG under the here applied conditions and doping concentrations.

In the following, the time dependent SH response curves of p$^+$-$\mathrm{Si/SiO_2}$ shown in Figs. 4.7 (c) and 4.8 (c) are numerically reproduced on the basis of the empirical model introduced in Eq. 5.2. The following relation extends Eq. 5.2 by a constant parameter $\mathrm{a_0} > 0$, which accounts for the built-in interfacial electric field $\mathrm{E_0}$:

$$I^{(2\omega)} \propto \left(a_0 + \sum_{i=1}^{4} a_i exp(-t/\tau_i^+) \right)^2 \tag{5.4}$$

Using this relation (Eq. 5.4) with $\mathrm{a_1}$, $\mathrm{a_4} > 0$ and $\mathrm{a_2}$, $\mathrm{a_3} < 0$, the SH measurements performed in p$^+$-$\mathrm{Si/SiO_2}$ in Figs. 4.7 (c) and 4.8 (c) are reproduced in good agreement. Figure 5.13 shows the time constants τ_i^+ for p$^+$-$\mathrm{Si/SiO_2}$ as extracted from the data fits versus the incident laser peak intensity in a double logarithmic plot. The time constant τ_1^+ in the case of p$^+$-$\mathrm{Si/SiO_2}$ describes the SH signal decrease ($a_1 > 0$) after the instantaneous SH signal in Fig. 4.8 (c) following the power law $1/\tau_1^+ \propto I_{l,p}^{n_1^+}$. The exponent $n_1^+ = 2.9$ appears to be equal to the related exponent n_1 for weakly doped virgin samples (Fig. 5.3) indicating a three-photon excitation process. This supports the argument that the SH signal decrease following the instantaneous SH signal in p$^+$-$\mathrm{Si/SiO_2}$ (Fig. 4.8 (c)) can be attributed to electron injection and trapping in the $\mathrm{SiO_2}$ layer opposing and compensating the doping related built-in electric field $\mathrm{E_0}$. In addition, the fact that the magnitudes of τ_1^+ in p$^+$-$\mathrm{Si/SiO_2}$ are comparable to the ones of τ_1 further strengthens this argument.

The time constant τ_4^+ describes the slow SH signal decrease ($a_4 > 0$) over a time scale of many minutes at high peak intensities in Fig. 4.7 (c), which is less pronounced in p$^+$-$\mathrm{Si/SiO_2}$ (Fig. 4.7 (b) and (c)) than in weakly doped virgin $\mathrm{Si/SiO_2}$ (Figs. 4.2 (a) and 4.7 (a)). τ_4^+ follows the power law $1/\tau_4^+ \propto I_{l,p}^{n_4^+}$ (Fig. 5.13). The exponent $n_4^+ = 3.2$ is similar to n_4 in weakly doped samples (Fig. 5.3) pointing to four-photon processes and

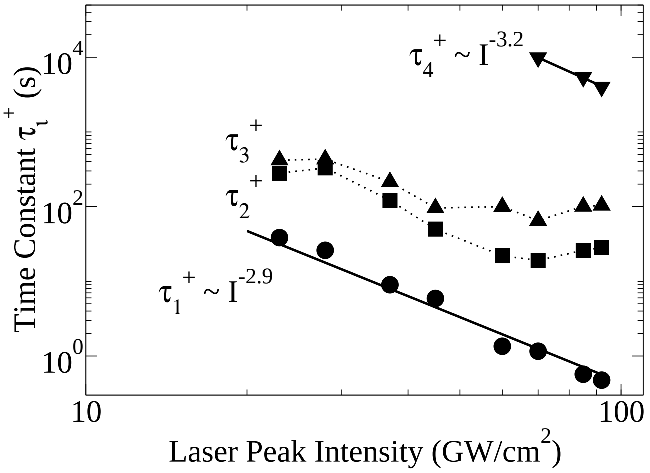

FIGURE 5.13: Time constant τ_i^+ as extracted from the numerical data fits in Figs. 4.7 (c) and 4.8 (c) according to Eq. 5.4; the dotted lines are guides to the eye.

hence hole injection into SiO_2. The magnitudes of τ_4^+ in Fig. 5.13 and τ_4 in Fig. 5.3 are comparable supporting the argument that the slow and less pronounced SH decrease over many minutes in p^+-Si/SiO_2 (Fig. 4.7 (c)) is due to hole injection and trapping in the oxide layers.

Evidently, the complicated intensity dependences of τ_2^+ and τ_3^+ in Fig. 5.13 and the inability to attribute τ_2^+ and τ_3^+ to defined charge carrier excitation processes point out the limits of the proposed empirical model and its applicability to p^+-Si/SiO_2. However, it reproduces the temporal SH response curves observed for p^+-Si/SiO_2 (Figs. 4.7 and 4.8) in good agreement and supports the main points of the proposed physical picture (Fig. 5.10) which is based on the doping related positive ionization of interface defect states yielding a built-in electric field E_0.

5.5.2 Photoinduced Charge Carrier Screening

Fig. 5.14 shows the instantaneous SH signal as highlighted by the arrows in Fig. 4.8 (c) as a function of the incident laser peak intensity in a double logarithmic plot. According to Eqs. 2.52 and 2.53 a quadratic dependence of the instantaneous SH signal on the incident fundamental intensity is expected as similarly seen in the deconvolution of electron and hole effects performed in Fig. 5.6. In the low intensity regime $\leq$ 45 GW/cm^2 the instantaneous SH signal amplitude follows a power law $I^{2\omega} \propto (I^{\omega})^n$ with $n = 1.7$ being close to the expected quadratic relation. The instantaneous SH signals observed for incident intensities higher than 45 GW/cm^2 unambiguously show a nonmonotonic deviation from the quadratic intensity dependence. Special care was taken to ensure that the time resolution of the experimental setup was suffient to record the instantaneous SH signal within an error margin of 5% even at high intensities > 45 GW/cm^2.

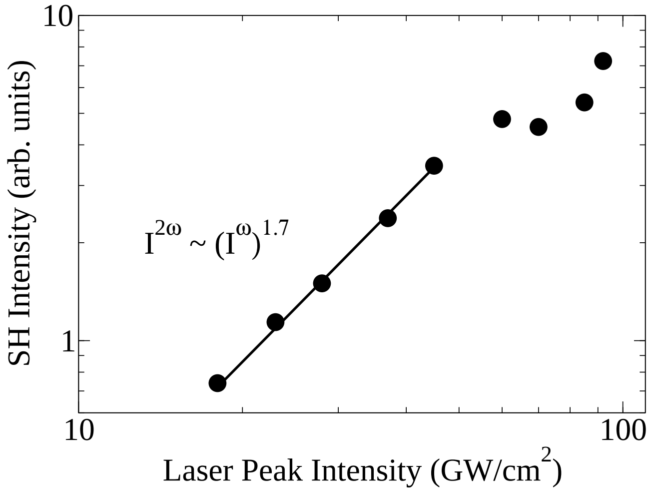

FIGURE 5.14: Instantaneous SH signal amplitude in p^+-Si/SiO_2 as indicated by arrows in Fig. 4.8 (c) versus incident laser peak intensity.

It is suggested that the observed deviation from the quadratic intensity dependence in Fig. 5.14 is due to photoinduced carrier screening [84] of the doping related built-in electric field E_0. The two-photon energy $2h\nu$ of the incident laser irradiation employed here lies close to the E_1 direct interband transition of silicon [63, 89]. Two-photon absorption is therefore resonantly enhanced. Upon laser irradiation a large density ($> 10^{17}$ cm^{-3}) of electron-hole pairs is photogenerated in silicon over an absorption depth of ~ 11 μm at the applied NIR frequency. Under the influence of the built-in electric field E_0 electrons begin to separate from holes, electrons being attracted to and holes being repelled from the interface. The result is a photoinduced screening of the built-in electric field E_0. Screening occurs on a time scale inversely proportional to ω_p, the plasma frequency of the electron-hole plasma [84]. It is hence an ultrafast effect and physically distinct from the multisecond and multiminute EFISH effects caused by charge carrier injection and trapping in SiO_2. Photoinduced screening is by orders of magnitude faster than the experimental time resolution of the SHG experiments presented here (0.2 s). Therefore the observed instantaneous SH signal (Fig.4.8 (c)) represents the screened built-in electric field. Screening physically changes the distance over which the interfacial electric field acts and hence changes the volume that contributes to EFISH. The amount of screening depends on the density of photogenerated electron-hole pairs and is hence a function of the incident laser peak intensity. It nonlinearly modulates the interfacial SH response caused by internal electric fields. The influence of screening increases with the incident laser peak intensity. The nonmonotonic intensity dependence observed at high peak intensities are therefore attributed to photoinduced carrier screening of the doping related built-in electric field E_0.

In a very recent study, Fomenko *et al.* observed a nonquadratic SH signal dependence on the incident intensity in the buried interface between $Si_{0.9}Ge_{0.1}$ and its oxide [127]. This effect is not doping related but supports the interpretation that carrier induced screening can severely perturb the quadratic intensity dependence of the observed SH signal, particularly, if electron-hole pair creation by two-photon absorption is resonantly enhanced.

The neutralization of positively charged interface defect states by photoexcited electrons upon laser irradiation, which would also affect the built-in electric field E_0, is believed to play a minor or neglegible role. E_0 is found to affect the photoinduced hole effects on a time scale of many minutes. This implies that E_0 stays constant. Thus a photoinduced recombination process affecting E_0 seems unlikely.

5.6 UV Laser Induced Sample Modifications

The photoinduced trap generation processes described in section 5.2 are due to NIR femtosecond laser irradiation. In order to gain additional information about light induced defect formation mechanisms in $\mathrm{Si/SiO_2}$, samples are exposed to pulsed UV light (308 nm, 4.03 eV, 16 ns) provided by an excimer laser source (section 3.4). It is assumed that single UV photon absorption in Si dominates at the applied peak intensities $\leq 175\ \mathrm{MW/cm^2}$ and absorption in $\mathrm{SiO_2}$ is neglegible due to its large band gap of 8.9 eV. Sample heating and melting of the near-interface silicon layer is expected in the applied fluence range from 0.45 to 2.8 $\mathrm{mJ/cm^2}$ [122]. The microscopic modification of $\mathrm{Si/SiO_2}$ in most cases appears to be due to melting and recrystallization of the silicon layers located underneath the ultrathin oxide. The following sections deal with the SHG analysis of the UV laser irradiated $\mathrm{Si/SiO_2}$ samples employing both, time dependent SHG and 2D SH imaging.

5.6.1 Time Dependent SHG in UV Laser Pre-Irradiated Si/SiO$_2$

Fig. 4.10 shows the comparison between the time dependent SH response curves of a $\mathrm{Si/SiO_2}$ sample area pre-irradiated by a single UV pulse (16 ns, 4.03 eV, 2.8 $\mathrm{mJ/cm^2}$) and the related SH response curves of virgin $\mathrm{Si/SiO_2}$ recorded in the low intensity regime at 41 $\mathrm{GW/cm^2}$ (a) and the high intensity regime at 86 $\mathrm{GW/cm^2}$ (b). Clearly, a time dependent EFISH response is observed in the UV irradiated sample indicating the presence of an $\mathrm{SiO_x}$ layer supporting photoinduced interfacial electron and hole transfer processes. In Fig. 4.10 (a) at 41 $\mathrm{GW/cm^2}$, the temporal SH response of the UV irradiated sample shows an accelerated SH signal rise as compared to the virgin sample. This observation is very similar to the findings in native $\mathrm{Si/SiO_2}$ pre-irradiated by NIR femtosecond pulses and indicates accelerated interfacial electron transfer processes. Eq. 5.1 is used to numerically fit the temporal SH reponse curves in Fig. 4.10 (a). The values of the time constants

τ_1^{UV} and τ_2^{UV} for UV irradiated $\mathrm{Si/SiO_2}$ are decreased by factors of ~15 and ~2 in comparison to those of virgin samples, respectively, and amount to $\tau_1^{UV} = (1.5 \pm 0.5)$ s and $\tau_2^{UV} = (37 \pm 5)$ s.

In order to explain these observations, the following arguments are discussed. Melting of near-interface silicon layers under UV laser irradiation undoubtedly leads to bond rupture at the interface. After the subsequent fast recrystallization the interfacial region appears to be microscopically modified. The defect density in the recrystallized silicon layers may be enhanced and supposedly a large fraction of unsaturated bonds is present at the interface. The melting point of silicon lies at $\sim$ 1400°C, i.e. a temperature high enough to initiate chemical reactions at the interface. It is well known that SiO is formed at $\mathrm{SiO_2}$-glass/silicon boundaries during the Czochralski growth of silicon [130, 131] from the melt. It hence seems probable that under pulsed UV irradiation $\mathrm{SiO_2}$ partly reduces to $\mathrm{SiO_x}$ having an altered interfacial stoichiometry. Consequently, the structure and composition of the interfacial suboxide layer are changed under pulsed UV irradiation and an enhanced interfacial electron trap density is reflected by the accelerated temporal SH response of the UV pre-irradiated $\mathrm{Si/SiO_2}$ sample shown in Fig. 4.10 (a). Looking at the equilibrium SH signal, on the other hand, only moderate changes are found upon UV laser irradiation (Fig. 4.11). Presumably the thickness of the oxide layer has not changed drastically [78].

Fig. 4.10 (b) recorded in the high intensity regime at 86 $\mathrm{GW/cm^2}$ shows that the slow SH decrease over many minutes related to photoinduced hole dynamics is not measurably affected by the preceeding exposure to UV irradiation. This is also reflected by the fitting curves using Eq. 5.2 (solid lines in Fig. 4.10 (b)) yielding time constants τ_3^{UV} and τ_4^{UV} for UV irradiated samples comparable to those of the virgin samples given in Table 5.1. This observation implies that in contrast to the findings for electrons the UV induced microscopic changes at the interface do not support accelerated hole trapping indicating essentially unchanged hole trap densities.

5.6.2 SH Imaging of UV Laser Pre-Irradiated Spots

Two different sets of SH imaging experiments are performed with UV irradiated $\mathrm{Si/SiO_2}$. In the first set the UV laser induced sample modification is investigated as a function of the applied UV pulse fluence. The second set involves SH imaging of UV laser modified areas generated by the repeated exposure to UV pulses of constant fluence.

5.6.2.1 Fluence Dependence of the UV Modification Process

The SH images of the UV pre-irradiated sample areas in Figs. 4.12 (a) - (h) are recorded using constant dwell times of 0.2 s and equal peak intensities of 93 $\mathrm{GW/cm^2}$. The observed SH signal heights are hence comparable and an approximate measure for the electron trap density apparent in the related $\mathrm{Si/SiO_2}$ sample area (Eqs. 2.52 and 2.53).

The first feature clearly seen in Fig. 4.12 refers to the approximately equal maximum SH signal heights within the UV modified sample areas (a) - (h). This finding is viewed as an indication that the electron trap densities do not vary significantly as a function of the UV pulse fluence in the regime between 0.5 and 2.8 $\mathrm{mJ/cm^2}$ (peak value in beam center). Obviously the enhanced electron trap density under UV irradiation saturates in the investigated pulse fluence regime. This observation is consistent with the second feature seen in Fig. 4.12, namely the increasing width of the UV modified sample area as a function of the applied pulse fluence indicating a clear threshold effect.

In the following, an analysis of the width increase of the defect areas (a) - (h) as a function of the UV pulse fluence is performed in order extract the threshold fluence required for saturation of the UV induced enhancement of the electron trap density. Fig. 5.15 shows Gaussian beam profiles representing the lateral fluence distribution across the long axis of the elliptic UV laser beam shape of the pulses (a) - (h) incident on the $\mathrm{Si/SiO_2}$ sample (Fig. 3.9). The maximum fluence in the center ranges from 0.5 $\mathrm{J/cm^2}$ (a) to 2.8 $\mathrm{J/cm^2}$ (h) as determined in section 3.4. The vertical line pairs (x,-x) in Fig. 5.15 indicate the widths (long axis) of the UV laser modified sample areas (a) - (h) as extracted from Fig. 4.12. The intercepts of these lines with the related Gaussian beam profiles are highlighted by empty circles. The fluence values corresponding to these intercepts are approximately equal in all cases (a) - (h) as shown by the horizontal regression line in Fig. 5.15. The fluence threshold value amounts to $\sim$ 0.47 $\mathrm{J/cm^2}$ and, following the above considerations, is interpreted as the melting threshold of near-interface silicon under pulsed UV irradiation of 308 nm wavelength and 16 ns duration. This value is comparable with the literature value of $\sim$ 0.36 $\mathrm{J/cm^2}$ determined by other methods for UV laser pulses of 193 nm wavelength [122]. The temperature of the melt is approximately constant, since, once established, any further deposited energy is converted into latent heat of the phase transition. This argument suits to explain the flat top shape of the SH images in Fig. 4.12 supporting the proposed thermally induced enhancement of the interfacial electron density.

It is noted that coherent artifacts [95] originating from the interference between space or time dependent and constant background contributions to the SH signal can have a disturbing influence on the precise spatially resolved imaging of the interface morphology. An estimated error of $\sim$ 15 % is assumed for the extracted values for the defect area widths

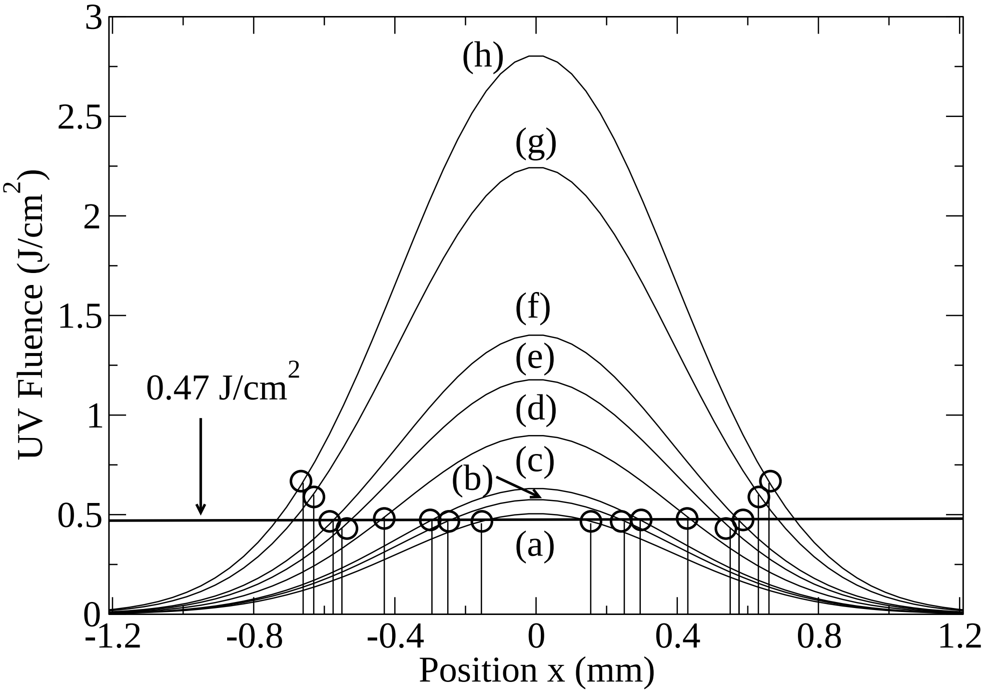

FIGURE 5.15: Gaussian beam profiles representing the one dimensional spatial fluence distribution of the UV laser pulses (a) - (h); vertical solid line pairs (x,-x) indicating the widths (long elliptic axis) of the defect areas (a) - (h) as extracted from Fig. 4.12; extracted fluence threshold $\sim$ 0.47 $\mathrm{J/cm^2}$ for UV laser induced melting of near-interface silicon layer.

as well as the above melting threshold value.

5.6.2.2 Accumulation of UV Modifications at Low Laser Fluence

The SH images displayed as 3D plots in Figs. 4.13 (a) - (d) are recorded under equal conditions as those in Fig. 4.12. They show UV laser modified areas in a $\mathrm{Si/SiO_2}$ sample pre-irradiated by several UV laser pulses. The applied UV pulse fluence of 0.45 $\mathrm{J/cm^2}$ is chosen in the vicinity of the melting threshold.

Both features in Figs. 4.13 (a) - (d), the increase of the maximum SH signal height as well as the growing widths of the defect areas under the repeated application of UV laser pulses, indicate that the multiple exposure to UV laser pulses successively enhances the electron trap density in $\mathrm{Si/SiO_2}$. Hence, an accumulative behaviour of this UV laser induced modification process is observed. This leads to the assumption that the microscopic change of the $\mathrm{Si/SiO_2}$ interface under UV irradiation is a function of the total energy deposited in the sample as long as the applied fluence value is below the melting threshold of the near-interface silicon layer. These considerations favour the argumentation that surface chemistry (e.g. reduction of $\mathrm{SiO_2}$ to SiO) takes place and that the chemical composition and stoichiometry of the suboxide layer change as a function of the deposited energy.

Finally, it is remarked that an optimization of the here-employed SH imaging procedure with regard to the integration and dwell times is required to resolve potential changes in the temporal SH response of $\mathrm{Si/SiO_2}$ samples upon UV irradiation at fluences below the melting threshold. This could possibly yield information whether charge carrier induced modifications of the microscopic interfacial structure occur under excimer UV laser irradiation in addition to the heat related effects.

Summary and Conclusions

This work employs time dependent optical second harmonic generation (SHG) as well as 2D second harmonic (SH) imaging using near infrared (NIR) femtosecond laser pulses (λ = 782.8 nm, (75 $\pm$ 5) fs, 10.5 nJ, 80 MHz) to probe photoinduced charge carrier dynamics as well as defect generation processes at the native $\mathrm{Si/SiO_2}$ interface. Prominent results refer to the dynamics of the interfacial transfer and relaxation of holes in $\mathrm{Si/SiO_2}$, the hole trap generation at the $\mathrm{Si/SiO_2}$ interface, the deconvolution of electron and hole effects as well as the built-in electric field in Boron doped $\mathrm{p^+}$- $\mathrm{Si/SiO_2}$, all of them obtained for the first time.

The temporal evolution of the SH signal generated in virgin $\mathrm{Si(100)/SiO_2}$ samples is investigated in the peak intensity regime 45 - 100 $\mathrm{GW/cm^2}$ for the first time and found to behave distinctly different as compared to the low intensity regime $\leq$ 45 $\mathrm{GW/cm^2}$. The new results are interpreted by photoinduced hole injection and trapping in ultrathin $\mathrm{SiO_2}$ contributing to the electric field induced second harmonic (EFISH) response of $\mathrm{Si/SiO_2}$. At intensities $>$ 45 $\mathrm{GW/cm^2}$ not only electrons are promoted from the silicon into the $\mathrm{SiO_2}$ conduction bands via three-photon excitation, but also holes are transferred across the interface into the $\mathrm{SiO_2}$ valence band following four-photon excitation. The complete temporal SH evolution is self-consistently reproduced by an empirical numerical model involving the superposition of opposing electron and hole contributions to the interfacial SH response. The time constants τ_i ($i = 1..4$) describing the interfacial electron and hole dynamics are extracted from the numerical data fits. The intensity dependences of all τ_i values appear to follow simple power laws $1/\tau_i \propto I^{n_i}$ with $n_1 = 2.9$ and $n_2 = 2.5$ for electrons and $n_3 = 3.2$ and $n_4 = 3.3$ for holes confirming the above order of the related multiphoton excitation processes initiating electron and hole injection into $\mathrm{SiO_2}$.

The time dependent SH measurements recorded in pre-irradiated $\mathrm{Si/SiO_2}$ samples are found to differ essentially from those in virgin $\mathrm{Si/SiO_2}$. Upon re-irradiation with identical parameters both electron as well as hole effects take place on a considerably shortened time scale after dark periods of 10 to 600 s. The numerical fits employing the same empirical model as for virgin samples reveil that the relevant time constants τ_i^p for pre-irradiated samples are approximately two orders of magnitude smaller than the related τ_i values for virgin samples. This observation is attributed to the photoinduced generation of permanent electrically active defects, which affect the injection and trapping of electrons and, as a new result, also of holes in the ultrathin $\mathrm{SiO_2}$ layer. The time constants τ_i^p show complex nonmonotonic intensity dependences and cannot simply be related to well defined multiphoton processes.

Furthermore, the charge carrier relaxation behaviour under dark conditions is investigated systematically. An enhanced maximum SH signal is observed immediately upon re-irradiation, the amplitude of which is for the first time found to depend on the duration of the preceeding dark period and saturates for ≥ 600 s. This enhancement as a function of dark time follows a simple exponential function and is attributed to the depopulation of hole trap sites. The time constant for hole detrapping in pre-irradiated $\mathrm{Si/SiO_2}$ is extracted and amounts to (110 ± 15) s.

Using the information obtained from the SHG experiments in pre-irradiated $\mathrm{Si/SiO_2}$ samples, the electron and hole contributions to the temporal SH response are deconvoluted and show that the photoinduced charge transfer into the ultrathin $\mathrm{SiO_2}$ layer is more efficient for electrons than for holes.

2D SH imaging is used to visualize femtosecond laser induced defects in $\mathrm{Si/SiO_2}$. Defect spots photogenerated by equal total fluence, but at different peak intensities show increasing SH signals and larger diameters with increasing peak intensity used for pre-irradiation. This fact implies that photoinduced defect generation under NIR femtosecond irradiation is a nonlinear function of the incident intensity. The findings observed with SH imaging are consistently reproduced by scanning electron microscopy.

For the first time SHG experiments are performed in native $\mathrm{Si/SiO_2}$ employing substantially doped silicon. In virgin Boron doped $\mathrm{p^+}$-$\mathrm{Si/SiO_2}$ time dependent EFISH measurements reveil the presence of a significant instantaneous SH signal for doping concentrations $> 7.5{\cdot}10^{17}\ \mathrm{cm^{-3}}$. This instantaneous SH signal is interpreted by a built-in interfacial electric field originating from the doping related positive ionization of defect states and band bending at the interface. It opposes to the electron induced effects and can be compensated by electron injection into $\mathrm{SiO_2}$. The dependence of the instantaneous SH signal on the incident laser peak intensity deviates from a purely quadratic relation, particularly for intensities $>$ 45 $\mathrm{GW/cm^2}$. This deviation is attributed to the intensity dependent screening of the built-in electric field by photoexcited electron-hole pairs. Furthermore, photoinduced hole injection and trapping is found to be less pronounced in $\mathrm{p^+}$-$\mathrm{Si/SiO_2}$ ($> 7.5 \cdot 10^{17}\ \mathrm{cm^{-3}}$) as compared to weakly doped samples. This is explained by the lower interfacial density of neutral hole traps, because the available traps are partly populated due to doping. The time dependent SH response curves of $\mathrm{p^+}$-$\mathrm{Si/SiO_2}$ are numerically reproduced by a generalized model, which employs the superposed electron and hole effects as well as the built-in electric field. The model supports the above interpretation in its main points in spite of its limitations in view of showing the underlying processes.

In the case of n-type doped $\mathrm{Si/SiO_2}$ samples no instantaneous SH signal is observed up to doping concentrations of $1.1 \cdot 10^{19}$ cm^{-3}. However, the results indicate that substantial n-type doping might affect the time constants related to electron dynamics as well as the saturation SH level of the time dependent interfacial SH response.

As a novel approach, the last set of experiments performed in this study combines the UV laser induced modification of $\mathrm{Si/SiO_2}$ employing a UV excimer laser source (λ = 308 nm, 16 ns, 0.45 - 2.8 $\mathrm{J/cm^2}$) and SHG as a probe using NIR femtosecond laser pulses. Time dependent EFISH measurements unambiguously show that the electron transfer into the ultrathin oxide is accelerated in UV laser pre-irradiated $\mathrm{Si/SiO_2}$. This result shows that UV laser induced melting and subsequent recrystallization of the near-interface silicon layer leads to an enhanced electron trap density at the $\mathrm{Si/SiO_2}$ interface. Possibly also thermally driven interface chemistry (e.g. reduction of $\mathrm{SiO_2}$ to SiO) takes place and results in a change of the structure and stoichiometry of the interfacial suboxide layer supporting accelerated interfacial electron transfer and trapping. The hole dynamics are found to be essentially unaffected by the UV laser induced sample modification.

2D SH images of $\mathrm{Si/SiO_2}$ sample areas pre-irradiated at different excimer laser pulse energies clearly show a saturation effect of the UV induced sample modification. A threshold fluence $\sim$ 0.47 $\mathrm{J/cm^2}$ is extracted and interpreted as the melting threshold of the near-interface silicon layer in agreement with a literature value of $\sim$ 0.36 $\mathrm{J/cm^2}$ obtained with an ArF excimer laser (λ = 193 nm). For the fluence values below the melting threshold an accumulative behaviour of the UV induced sample modification is observed under repeated exposure to several UV laser pulses. This points to a dose dependent effect supporting the argument that heat driven chemical reactions are responsible for the microscopic change and enhanced electron trap density upon UV laser irradiation of $\mathrm{Si/SiO_2}$.

Overall, the SHG experiments with native $\mathrm{Si/SiO_2}$ presented in this dissertation as well as the interpretation thereof have added some new aspects to a more profound understanding of interfacial charge carrier separation processes as well as defect generation. Particularly, regarding the EFISH contribution of holes, which has been discussed controversely in the literature, interesting novel insight is gained. On the one hand, the results are relevant in the context of technologically important questions regarding the growth and application of ultrathin oxides layers in MOS devices. On the other hand, they are of interest in the field of basic solid state physics dealing with the structural and optical properties of buried interfaces between crystalline and amorphous solids.

Outlook

Based on its results this dissertation brings forward a variety of new questions and ideas for further promising experimental as well as numerical investigations. These refer to the application of the optical probing technique SHG in general and in particular concern the $\mathrm{Si/SiO_2}$ system as an important example for a buried solid-solid interface, which remains subject to intensive research.

The temporal SH response of native $\mathrm{Si/SiO_2}$ interfaces pre-irradiated by NIR femtosecond irradiation is found to behave essentially different as compared to virgin samples. The time dependent SH data curves recorded in pre-irradiated $\mathrm{Si/SiO_2}$ are successfully simulated using the same empirical model as for virgin samples. The physical interpretation of the obtained time constants, however, appears to be problematic. The precise determination of the mechanisms responsible for the temporal SH response of pre-irradiated samples is at its beginning. Further experimental studies as well as an alternative approach for the numerical reproduction of the data are required. Such studies could involve the investigation of the temporal SH response using different polarization combinations between excitation and detection as well as different incident wavelengths. Further information can potentially be gained with pump-probe experiments investigating the defect generation process on ultrashort time scales. The development of an *ab initio* model can be fruitful to gain further insight into the nature of the photoinduced defect generation processes involving interfacial electron and hole dynamics. Furthermore, the comparison of time dependent SH measurements in oxidized silicon of different surface orientations could possibly reveil information about the influence of different interfacial bonding configurations on the defect generation mechanisms.

In order to verify the proposed screening effect of the built-in electric field observed in substantially p-type doped $\mathrm{Si/SiO_2}$, time dependent SH measurements at a SH frequency far away from the silicon interband transitions are suggested. Under such conditions, where the photogeneration of electron-hole pairs is not resonantly enhanced, in contrast to the here performed experiments, the screening effect is expected to be less pronounced. The preliminary SH measurements performed with highly n-type doped $\mathrm{Si/SiO_2}$ are indicative of altered electron dynamics in comparison to weakly doped samples. Further experiments and a quantitative analysis of the electron related time constants are suggested to obtain further information about the influence of populated donor levels on the interfacial SH response. Furthermore, systematic SHG experiments with pre-irradiated highly doped $\mathrm{Si/SiO_2}$ samples are prospective to yield further information about photoinduced defect generation. SHG may be suitable to detect the doping related ionization of laser generated defects at the $\mathrm{Si/SiO_2}$ interface and thus reveil further details about the microscopic structure of photoinduced defects. The results can stimulate the development of a numerical model suitable to describe the data in a physically more consistent form than the here employed model based on simple exponential functions.

The precise and quantitative analysis of time dependent SH response curves of UV laser modified $\mathrm{Si/SiO_2}$ recorded at a wide range of incident intensities (fluences and pulse durations), wavelengths as well as polarizations possibly allows further statements about the UV induced modification processes presumably involving interfacial chemical reactions. Further experiments are required, especially at UV pulse fluences below the melting threshold with optimized SH imaging techniques to establish a profound experimental data basis useful for model calculations.

Overall, the results obtained within this work stimulate a number of promising investigations concerning the $\mathrm{Si/SiO_2}$ system using ultrathin oxides, which become increasingly important in MOS technology. Furthermore, as demonstrated in this dissertation, SHG is a uniquely surface and interface sensitive probe and, hence, has an enormous potential to investigate a wide variety of material systems. Apart from crystalline surfaces and buried solid-solid interfaces, a variety of boundaries is accessible by SHG. For instance, cell membranes and their complex ion transport mechanisms or solid-gas boundaries and their use for catalytic reactions can be studied by SHG opening up new fields of research at the boundary between materials science, physics, chemistry and life science.

Bibliography

[1] M. Göppert-Mayer, Ann. Phys. (Leipzig) **9**, 273, 1931

[2] P. A. Franken, A. E. Hill, C. V. Peters, G. Weinrich, Phys. Rev. Lett. **7**, 118, 1961

[3] J. A. Armstrong, N. Bloembergen, J. Ducuing, P. S. Pershan, Phys. Rev. **127**, 1918, 1962

[4] N. Bloembegen, P. S. Pershan, Phys. Rev. **128**, 606, 1962

[5] G. Lüpke, Surf. Sci. Rep. **35**, 75-161, 1999

[6] C. T. Williams, D. A. Beattie, Surf. Sci. **500**, 545-576, 2002

[7] Y. R. Shen, *The Principles of Nonlinear Optics*, Wiley, New York, 1984

[8] F. Brown, R. E. Parks, A. M. Sleeper, Phys. Rev. Lett. **14**, 1029, 1965

[9] P. S. Winokur, H. E. Boesch Jr., J. M. McGarrity, F. B. McLean, J. Appl. Phys. **50**, 3492, 1979

[10] Z.-Y. Lu, C. J. Nicklaw, D. M. Fleetwood, R. D. Schrimpf, S. T. Pantelides, Phys. Rev. Lett. **89**, 285505, 2002

[11] S. Bergfeld, B. Braunschweig, W. Daum, Phys. Rev. Lett. 93, 097402, 2004

[12] B. S. Mendoza, M. Palummo, G. Onida, R. Del Sole, Phys. Rev. B **63**, 205406, 2001

[13] D. J. DiMaria, J. W. Stasiak, J. Appl. Phys. **65**, 2342, 1989

[14] G. J. Hu, W. C. Johnson, J. Appl. Phys. **54**, 1441, 1982

[15] F. B. McLean, IEEE Trans. Nucl. Sci. **NS-23**, 1651, 1980

[16] N. S. Saks, C. M. Dozier, D. B. Brown, IEEE Trans. Nucl. Sci. **35**, 1168, 1988

[17] P. M. Lenahan, P. V. Dressendorfer, Appl. Phys. Lett. **44**, 96, 1984

[18] P. M. Lenahan, P. V. Dressendorfer, J. Appl. Phys. **55**, 3495, 1984

[19] S. L. Elliot, R. F. Broom, C. J. Humphreys, J. Appl. Phys. **91**, 9116, 2002

[20] B. Kaczer, Z. Meng, J. P. Pelz, Phys. Rev. Lett. **77**, 91, 1996

[21] H. Watanabe, K. Fujita, M. Ichikawa, Appl. Phys. Lett. **72**, 1987, 1998

[22] D. Guidotti, T. A. Driscoll, H. J. Gerritson, Solid State Commun. **46**, 337, 1983

[23] T. A. Driscoll, D. Guidotti, Phys. Rev. B **28**, 1171, 1983

[24] C. V. Shank, R. Yen, C. Hirlimann, Phys. Rev. Lett, **51**, 900, 1983

[25] H. W. K. Tom, T. F. Heinz, Y. R. Shen, Phys. Rev. Lett. **51**, 1983, 1983

[26] J. E. Sipe, J. J. Moss, H. M. van Driel, Phys. Rev. B, **35**, 1129, 1987

[27] J. E. Sipe, V. Mizrahi, G. I. Stegeman, Phys. Rev. B **35**, 9091, 1987

[28] J. E. Sipe, J. Opt. Soc. Am. B **4**, 481, 1987

[29] J. E. Sipe, Surf. Sci. **105** 489, 1980

[30] P. Guyot-Sionnest, W. Chen, Y. R. Shen, Phys. Rev. B **33**, 8254, 1986

[31] P. Guyot-Sionnest, Y. R. Shen, Phys. Rev. B, **35**, 4420, 1987

[32] P. Guyot-Sionnest, Y. R. Shen, Phys. Rev B **38**, 7985, 1988

[33] D. J. Bottomley, G. Lüpke, C. Meyer, Y. Makita, Opt. Lett. **20**, 453, 1995

[34] D. J. Bottomley, G. Lüpke, J. G. Mihaychuk, H. M. van Driel, J. Appl. Phys. **74**, 6072, 1993

[35] G. Lüpke, D. J. Bottomley, H. M. van Driel, J. Opt. Soc. Am. B, **11**, 33, 1994

[36] D. Epperlein, B. Dick, G. Marowsky, Appl. Phys. B **44**, 5, 1987

[37] B. U. Felderhof, G. Marowsky, Appl. Phys. B **44**, 11, 1987

[38] B. U. Felderhof, A. Bratz, G. Marowsky, O. Roders, F. Sieverdes, J. Opt. Soc. Am. B **10**, 1824, 1993

[39] F. Sieverdes, M. Pinnow, G. Marowsky, Appl. Phys. B **54**, 95, 1992

[40] A. Liebsch, Surf. Sci. **307-309**, 1007, 1994

[41] B. Koopmans, F. van der Woude, G. A. Sawatzky, Phys. Rev. B **46**, 12780, 1992

[42] T. F. Heinz, M. M. T. Loy, W. A. Thomspson, J. Vac. Sci Technol. B **3**, 1467, 1985

[43] P. Bratu, K. L. Kompa, U. Höfer, Phys. Rev. B **49**, 14070, 1994

[44] A. A. Shklyaev, T. Suzuki, Phys. Rev. Lett. **75**, 272, 1995

[45] C. W. van Hasselt, E. Mateman, M. A. C. Devillers, T. Rasing, A. A. Fedyanin, E. D. Mishina, O. A. Aktsipetrov, J. C. Jans, Surf. Sci. **331-333**, 1367, 1995

[46] O. A. Aktsipetrov, A. A. Fedyanin, E. D. Mishina, A. A. Nikulin, A. N. Rubtsov, C. W. van Hasselt, M. A. C. Devillers, T. Rasing, Phys. Rev. Lett. **78**, 46, 1997

[47] S. A. Mitchell, R. Boukherroub, S. Anderson, J. Phys. Chem. B **104**, 7668, 2000

[48] S. A. Mitchell, M. Mehendale, D. M. Villeneuve, R. Boukherroub, Surf. Sci. **488**, 367, 2001

[49] S. A. Mitchell, J. Phys. Chem. B **107**, 9388, 2003

[50] C. H. Bjorkman, T. Yasuda, C. E. Shearon Jr., Y. Ma, G. Lucovsky, U. Emmerichs, C. Meyer, K. Leo, H. Kurz, J. Vac. Sci. Technol. B **11**, 1521, 1993

[51] C. H. Bjorkman, C. E. Shearon Jr, Y. Ma, T. Yasuda, G. Lukovsky, U. Emmerichs, C. Meyer, K. Leo, H. Kurz, J. Vac. Sci. Technol. A **11**, 964, 1993

[52] U. Emmerichs, C. Meyer, H. J. Bakker, H. Kurz, C. H. Bjorkman, C. E. Shearon Jr., Y. Ma, T. Yasuda, Z. Jing, G. Lucovsky, J. L. Whitten, Phys. Rev. B **50**, 5506, 1994

[53] F. Ito, H. Hirayama, Phys. Rev. B **50**, 11208, 1994

[54] H. Hirayama, K. Watanabe, Phys. Rev. B **51**, 14717, 1995

[55] H. Hirayama, F. Ito, K. Watanabe, J. Vac. Sci. Technol A **13**, 750, 1995

[56] K. Watanabe, H. Hirayama, M. Kawata, Appl. Phys. Lett. **66**, 2232, 1995

[57] K. Watanabe, M. Kawata, E. Hasegawa, H. Hirayama, J. Appl. Phys. **79**, 4146, 1996

[58] K. Koh, H. Niimi, G. Lucovsky, Surf. Coatings Technol. **98**, 1524, 1998

[59] G. Lucovsky, J. Vac. Sci. Technol. A **16**, 356, 1998

[60] J. Dadap, B. Doris, Q. Deng, M. Downer, J. Lowell, A. Diebold, Appl. Phys. Lett. **64**, 2139, 1994

[61] S. T. Cundiff, W. H. Knox, F. H. Baumann, K. W. Evans-Lutterodt, M.-T. Tang, M. L. Green, H. M. van Driel, Appl. Phys. Lett. **70**, 1414, 1997

[62] G. Erley, W. Daum, Phys. Rev. B **58**, 1734(R), 1998

[63] W. Daum, H.-J. Krause, U. Reichel, H. Ibach, Phys. Rev. Lett. **71**, 1234, 1993

[64] C. Meyer, G. Lüpke, U. Emmerichs, F. Wolter, H. Kurz, C. H. Bjorkman, G. Lucovsky, Phys. Rev. Lett. **74**, 3001, 1995

[65] G. Lüpke, D. J. Bottomley, H. M. van Driel, Phys. Rev. B **47**, 10389, 1993

[66] C. W. van Hasselt, M. A. Verheijen, Th. Rasing, Phys. Rev. B, **42**, 9263, 1990

[67] G. Lüpke, C. Meyer, U. Emmerichs, F. Wolter, H. Kurz, Phys. Rev. B **50**, 17292, 1994

[68] Y. Q. An, S. T. Cundiff, Phys. Rev. B 67, 193302, 2003

[69] O. A. Aktsipetrov, T. V. Dolgova, A. A. Fedyanin, D. Schuhmacher, G. Marowsky, Thin Solid Films **364**, 91, 2000

[70] M. Dürr, U. Höfer, Phys. Rev. Lett. **88**, 076107, 2002

[71] G. Lucovsky, A. Banerjee, H. Niimi, K. Koh, B. Hinds, C. Meyer, G. Lüpke, H. Kurz, Appl. Surf. Sci. **117/118**, 202, 1997

[72] G. Lucovsky, K. Koh, B. Chaflin, B. Hinds, Appl. Surf. Sci. **123/124**, 490, 1998

[73] D. Lim, M. C. Downer, J. G. Ekerdt, N. Arzate, B. S. Mendoza, V. I. Gavrilenko, R. Q. Wu, Phys. Rev. Lett. **84**, 3406, 2000

[74] C. Völkmann, M. Reichelt, T. Meier, S. W. Koch, U. Höfer, Phys. Rev. Lett. **92**, 127405, 2004

[75] C. H. Lee, R. K. Chang, N. Bloembergen, Phys. Rev. Lett. **18**, 167, 1967

[76] O. A. Aktsipetrov, A. A. Fedyanin, V. N. Golovkina, T. V. Murzina, Opt. Lett. **19**, 1450, 1995

[77] J. G. Mihaychuk, J. Bloch, H. M. van Driel, Opt. Lett. **20**, 2063, 1995

[78] J. Bloch, J. G. Mihaychuk, H. M. van Driel, Phys. Rev. Lett. **77**, 920, 1996

[79] N. Shamir, J. G. Mihaychuk, H. M. van Driel, Phys. Rev. Lett. **82**, 359, 1999

[80] J. G. Mihaychuk, N. Shamir, H. M. van Driel, Phys. Rev. B **59**, 2164, 1999

[81] O. A. Aktsipetrov, A. A. Fedyanin, E. D. Mishina, A. N. Rubtsov, C. W. van Hasselt, M. A. C. Devillers, Th. Rasing, Phys. Rev. B **54**, 1825, 1996

[82] O. A. Aktsipetrov, A. A. Fedyanin, E. D. Mishina, A. N. Rubtsov, C. W. van Hasselt, M. A. C. Devillers, Th. Rasing, Surf. Sci. **352-354**, 1033, 1996

[83] T. V. Dolgova, A. A. Fedyanin, O. A. Aktsipetrov, Phys. Rev. B **68**, 073307, 2003

[84] J. I. Dadap, P. T. Wilson, M. H. Anderson, M. C. Downer, Opt. Lett. **22**, 901, 1997

[85] J. I. Dadap, X. F. Hu, M. H. Anderson, M. C. Downer, J. K. Lowell, O. A. Aktsipetrov, Phys. Rev. B **53**, R7607, 1996

[86] G. Lüpke, C. Meyer, C. Ohlhoff, H. Kurz, S. Lehmann, G. Marowsky, Opt. Lett. **20**, 1997, 1995

[87] C. Meyer, G. Lüpke, Z. G. Lü, A. Gölz, H. Kurz, G. Lucovsky, J. Vac. Sci. Technol. B **14**, 3107, 1996

[88] C. Ohlhoff, G. Lüpke, C. Meyer, H. Kurz, Phys. Rev. B **55**, 4596, 1997

[89] P. Godefroy, W. de Jong, C. W. van Hasselt, M. A. C. Devillers, Th. Rasing, Appl. Phys. Lett. **68**, 1981, 1996

[90] Z. Marka, R. Pasternak, S. N. Rashkeev, Y. Jiang, S. T. Pantelides, N. H. Tolk, P. K. Roy, J. Kozub, Phys. Rev. B **67**, 045302, 2003

[91] Z. Marka, S. K. Singh, W. Wang, S. C. Lee, J. Kavich, B. Glebov, S. N. Rashkeev, A. P. Karmarkar, R. G. Albridge, S. T. Pantelides, R. D. Schrimpf, D. M. Fleetwood, N. H. Tolk, IEEE Trans. Nucl. Sci. **47**, 2256, 2000

[92] J. Fang, W. W. Heidbrink, G. P. Li, J. Appl. Phys. **88**, 2641, 2000

[93] J. Fang, G. P. Li, Appl. Phys. Lett. **72**, 1987, 1998

[94] M. Cernusca, R. Heer, G. A. Reider, Appl. Phys. B: Lasers and Optics **B66**, 367, 1998

[95] G. A. Reider, M. Cernusca, M. Hofer, Appl. Phys. B: Lasers and Optics **B68**, 343, 1999

[96] N. Shamir, J. G. Mihaychuk, H. M. van Driel, J. Vac. Sci. Technol. A **15**, 2081, 1997

[97] S. A. Mitchell, S. Janz, J. A. Bardwell, Chem. Phys. Lett. **310**, 361, 1999

[98] V. Fomenko, C. Hurth, T. Ye, E. Borguet, J. Appl. Phys. **91**, 4394, 2002

[99] W. Wang, G. Lüpke, M. Di Ventra, S. T. Pantelides, J. M. Gilligan, N. H. Tolk, I. C. Kizilyalli, P. K. Roy, G. Margaritondo, G. Lucovsky, Phys. Rev. Lett. **81**, 4224, 1998

[100] Yu. D. Glinka, W. Wang, S. K. Singh, Z. Marka, S. N. Rashkeev, Y. Shirokaya, R. Albridge, S. T. Pantelides, N. H. Tolk, G. Lucovsky, Phys. Rev. B **65**, 193103, 2002

[101] T. Scheidt, E. G. Rohwer, H. M. von Bergmann, H. Stafast, Eur. Phys. J. Appl. Phys. **27**, 393, 2004

[102] T. Scheidt, E. G. Rohwer, H. M. von Bergmann, H. Stafast, Phys. Rev. B **69**, 165314, 2004

[103] C. Rauscher, *Transiente Infrarot-Spektroskopie an wasserstoffverbrückten Flüssigkeiten mit Sub-Pikosekunden Zeitauflösung*, Dissertation, Technische Universität München 1997

[104] R. W. Boyd, *Nonlinear Optics*, Academic Press London, 1992

[105] M. J. Buerger, *Elementary Crystallography*, Wiley, New York, 1963

[106] N. Butcher, *Nonlinear Optical Phenomena*, Ohio State University, 1965

[107] R. W. J. Hollering, M. Barmentlo, Opt. Commun. **88**, 141, 1992

[108] N. Bloembergen, *Nonlinear Optics*, Benjamin, New York, 1965

[109] N. Bloembergen, R. K. Chang, S. S. Jha, C. H. Lee, Phys. Rev. **174**, 813, 1968

[110] P. F. Moulton, J. Opt. Soc. Am. B **3**, 125, 1986

[111] U. Morgner, F. X. Kärtner, S. H. Cho, H. A. Haus, J. G. Fujimoto, E. P. Ippen, V. Scheuer, G. Angelow, T. Tschudi, Opt. Lett **24**, 411, 1999

[112] M. Nisoli, S. De Silvestri, O. Svelto, R. Szipöcs, K. Ferencz, Ch. Spielmann, S. Sartania, F. Krausz, Opt. Lett. **22**, 522, 1997

[113] T. Brabec, Ch. Spielmann, P. F. Curley, F. Krausz, Opt Lett. **17**, 1292, 1992

[114] A. Thaller, M. Lettenberger, A. Brodschelm, *Fitclient*, *Fithelper*, Private Communications, 2001

[115] P. W. Milonni, J. H. Eberly, *Lasers*, Wiley & sons, New York, 1988

[116] R. P. Southwell, M. A. Mendicino, E. G. Seebauer, J. Vac. Sci. Technol. A **14**, 928, 1996

[117] Kapil Dev, M. Y. L. Jung, R. Gunawan, R. D. Braatz, E. G. Seebauer, Phys. Rev. B **68**, 195311, 2003

[118] M. J. Keevers, M. A. Green, Solar Energy Materials and Solar Cells **41/42**, 195, 1996

[119] M. A. Green, M. J. Keevers, Progress in Photovoltaics **3**, 189, 1995

[120] C. V. Shank, R. Yen, C. Hirlimann, Phys. Rev. Lett. **50**, 454, 1983

[121] J. I. Dadap, F. X. Hu, N. M. Russell, J. G. Ekerdt, J. K. Lowell, M. C. Downer, IEEE J. Sel. Top. Quantum Electron. **1**, 1145, 1995

[122] I. Lukes, R. Sasik, R. Cerny, Appl. Phys. A **54**, 327, 1992

[123] Kapil Dev, E. G. Seebauer, Surf. Sci. **550**, 185, 2004

[124] M. Y. L. Jung, R. Gunawan, R. D. Braatz, E. G. Seebauer, J. Appl. Phys. **95**, 1134, 2004

[125] J. I. Goldstein, D. E. Newbury, P. Echlin, D. C. Joy, C. Fiori, E. Lifshin, *Scanning Electron Microscopy and X-Ray Microanalysis*, Plenum, New York, 1981

[126] V. Fomenko, E. Borguet, Phys. Rev. B **68**, 081301(R), 2003

[127] V. Fomenko, J.-F. Lami, E. Borguet, Phys. Rev. B **63**, 121316(R), 2001

[128] M. McEllistrem, G. Haase, D. Chen, R. J. Hamers, Phys. Rev. Lett. **70**, 2471, 1993

[129] D. E. Aspnes, Surf. Sci. **37**, 418, 1973

[130] X. Huang, K. Terashima, K. Izunome, S. Kimura, Jpn. J. Appl. Phys. **33**, L902, 1994

[131] X. Huang, K. Terashima, K. Hoshikawa, Jpn. J. Appl. Phys. **38**, L1153, 1999

LADUNGSTRÄGERDYNAMIK UND DEFEKTGENERATION AN DER SI/SIO$_2$-GRENZFLÄCHE UNTERSUCHT MITTELS ERZEUGUNG DER OPTISCHEN ZWEITEN HARMONISCHEN DURCH ULTRAKURZE LICHTIMPULSE

Zusammenfassung

In der vorliegenden Arbeit werden die zeitabhängige Erzeugung der optischen zweiten Harmonischen (Second Harmonic Generation (SHG)) mittels nahinfraroter (NIR) ultrakurzer Lichtimpulse (λ = 782.8 nm, (75 ± 5) fs, 10.5 nJ, 80 MHz) sowie bildgebende SHG-Verfahren (SH imaging) benutzt, um die photoinduzierte Dynamik von Ladungsträgern sowie die Defektgeneration an der $\mathrm{Si/SiO_2}$-Grenzfläche zu untersuchen. Einige Ergebnisse sind vollständig neu und betreffen den laserinduzierten Transfer von Löchern in die ultradünne Oxidschicht und deren Relaxation, die Generation von Lochfallen an der $\mathrm{Si/SiO_2}$-Grenzfläche, die Entfaltung von Elektron- und Lochdynamik sowie das dotierungsbedingte interne elektrische Feld in stark Bor-dotiertem $\mathrm{p^+}$- $\mathrm{Si/SiO_2}$.

Die zeitliche Entwicklung des SHG-Signals an der $\mathrm{Si/SiO_2}$-Grenzfläche wird erstmalig im Intensitätsbereich 45 - 100 $\mathrm{GW/cm^2}$ untersucht und zeigt eine deutlich andere Dynamik als im Bereich niedrigerer Intensitäten $\leq$ 45 $\mathrm{GW/cm^2}$. Die Ergebnisse werden selbstkonsistent interpretiert unter Berücksichtigung von Lochinjektion und Population von Lochfallen in der ultradünnen $\mathrm{SiO_2}$ Schicht, die zum fieldinduzierten SHG-Signal beitragen. Bei Eingangsintensitäten > 45 $\mathrm{GW/cm^2}$ gelangen nicht nur Elektronen nach 3-Photonen-Anregung vom Silizium in das $\mathrm{SiO_2}$-Leitungsband, sondern auch Löcher nach 4-Photonen-Anregung in das $\mathrm{SiO_2}$-Valenzband. Die gesamte zeitliche Entwicklung des SHG-Signals wird quantitativ durch ein empirisches Modell reproduziert, welches die Elektron- und Lochbeiträge zum SHG-Signal addiert. Die numerische Anpassung dieses Modells an die experimentellen Daten führt zu Zeitkonstanten τ_i (i = 1..4), welche die Elektron- und Lochdynamik an der $\mathrm{Si/SiO_2}$-Grenzfläche widerspiegeln. Die Abhängigkeiten der τ_i-Werte von der Laserspitzenintensität folgen Potenzgesetzen $1/\tau_i \propto I^{n_i}$ mit $n_1 = 2.9$ und $n_2 = 2.5$ für Elektronen und $n_3 = 3.2$ und $n_4 = 3.3$ für Löcher, welche die 3- bzw. 4-Photonenprozesse als Auslöser für die Elektronen- bzw. Löcherinjektion vom Silizium in die $\mathrm{SiO_2}$-Schicht bestätigen.

Zeitabhängige SHG-Experimente an vorbestrahlten $\mathrm{Si/SiO_2}$-Proben zeigen, daß sowohl die Elektron- als auch Lochdynamiken auf deutlich kürzeren Zeitskalen als in jungfräulichen Proben stattfinden. Die numerische Datenanpassung des obigen Modells ergibt um etwa zwei Größenordnungen kleinere Werte für die Zeitkonstanten τ_i^p in vorbestrahlten

Proben verglichen mit den τ_i-Werten für jungfräuliche Proben. Diese Beobachtung wird durch photoinduzierte Defektgeneration erklärt, durch welche unter Laserbestrahlung irreversibel sowohl Elektron- und erstmalig auch Lochfallen erzeugt werden. Somit weisen vorbestrahlte Probe eine höhere Dichte elektrisch aktiver Fallen auf, die für die schnelle Ladungsträgerseparation verantwortlich sind. Die τ_i^p Werte zeigen komplexe, nichtmonotone Intensitätsabhängigkeiten und können nicht auf einfache Weise wohldefinierten Multiphotonenprozessen zugeordnet werden.

Die erstmalige systematische Untersuchung der Probenrelaxation im Dunkeln anhand des SHG-Signals bei Wiederbestrahlung nach Dunkelperioden zwischen 10 und 600 s zeigt ein überhöhtes maximales SHG-Signal, dessen Amplitude mit der Dauer der Dunkelperiode bis etwa 600 s ansteigt. Diese Signalüberhöhung wird der Relaxation von ionisierten Lochfallen bei Strahlunterbrechung zugeordnet und hat eine Zeitkonstante von (110 ± 15) s.

Mit Hilfe der Erkenntnisse aus den SHG-Experimenten an vorbestrahlten Proben können die Elektron- bzw. Lochbeiträge zum SHG-Signal an der $\mathrm{Si/SiO_2}$ Grenzfläche entfaltet werden. Sie zeigen eine höhere Effizienz für den Transfer von Elektronen in die Oxidlage als für Löcher.

Bildgebende SHG (SH Imaging) wird angewendet, um photoinduzierte Defektstellen in $\mathrm{Si/SiO_2}$ zu visualisieren. Probenstellen, die mit identischer Dosis, aber verschiedenen Intensitäten vorbestrahlt wurden, zeigen für höhere Intensitäten bei der Vorbestrahlung sowohl höhere SHG-Signale als auch grössere Durchmesser. Diese Beobachtungen beinhalten, daß die photoinduzierte Defektgeneration unter Bestrahlung mit NIR- Femtosekundenimpulsen eine nichtlineare Funktion der Eingangsintensität ist. Diese Defekte sind permanent, was durch SH Imaging und *Scanning Electron Microscopy* bestätigt wird.

Erstmalig werden zeitabhängige SHG-Messungen an stark dotierten $\mathrm{Si/SiO_2}$-Proben durchgeführt. Für Bor-Dotierungskonzentrationen > $7.5 \cdot 10^{17}\ \mathrm{cm}^{-3}$ wird ein instantanes SHG-Signal beobachtet und einem internen elektrischen Feld zugeordnet, das sich aufgrund positiver Ionisierung von Grenzflächenzuständen bei starker p-Dotierung ausbildet. Dieses interne Feld ist den laserinduzierten Elektroneneffekten entgegengerichtet und wird von diesen überlagert. Die Intensitätsabhängigkeit des instantanen SHG-Signals ist nichtquadratisch, was auf eine Abschirmung des internen elektrischen Feldes durch photogenerierte Elektron-Loch-Paare hindeutet. Die Photoinjektion und Population von Lochfallen ist in stark p-dotiertem $\mathrm{Si/SiO_2}$ (> $7.5 \cdot 10^{17}\ \mathrm{cm}^{-3}$) gehemmt im Vergleich zu schwach dotierten Proben. Dies wird durch eine kleinere Dichte an verfügbaren Lochfallen erklärt, weil die Fallen zumindest teilweise aufgrund der starken Dotierung populiert sind. Die Erweiterung des obigen empirischen Simulationsmodells unter Berücksichtigung des durch

Dotierung hervorgerufenen internen elektrischen Feldes reproduziert die zeitabhängigen Messkurven. Das Modell unterstützt die obige Interpretation in den wesentlichen Punkten, auch wenn es nur teilweise die zugrundeliegenden Prozesse erkennen lässt.

In stark n-dotierten $\mathrm{Si/SiO_2}$-Proben wird bis zu Dotierungskonzentrationen von $\sim 10^{19}$ $\mathrm{cm^{-3}}$ kein instantanes SHG Signal und damit keine dotierungsabhängige Ladungsträgeranhäufung an der $\mathrm{Si/SiO_2}$ Grenzfläche beobachtet. Vorläufige Ergebnisse deuten auf eine beschleunigte Dynamik der Elektroneneffekte in stark n-dotiertem $\mathrm{Si/SiO_2}$ hin.

Erstmals wird in dieser Arbeit die Methode SHG benutzt, um Modifikationen in $\mathrm{Si/SiO_2}$ zu untersuchen, die durch UV-Excimer-Laser-Impulse (λ = 308 nm, 16 ns, 0.45 - 2.8 $\mathrm{J/cm^2}$) erzeugt werden. Zeitabhängige SHG-Experimente zeigen einen deutlich beschleunigten Elektronentransfer in die $\mathrm{SiO_2}$-Schicht. Diese Beobachtung zeigt, daß die UV-Laser-induzierte Schmelze und nachfolgende Rekristallisierung von grenzflächennahem Silizium zu einer Erhöhung der Elektronenfallendichte an der $\mathrm{Si/SiO_2}$-Grenzfläche führen. Auch thermisch ausgelöste chemische Reaktionen, insbesondere die Reduktion von $\mathrm{SiO_2}$ zu SiO an der Grenzfläche, werden als mögliche Mechanismen zur UV-induzierten Probenmodifikation vorgeschlagen. Somit werden Stöchiometrie und Struktur der grenzflächennahen Suboxidschicht ($\mathrm{SiO_x}$) verändert, was eine Erhöhung der Elektronenfallendichte plausibel macht. Die Lochdynamik ist von der UV-Laser-induzierten Probenmodifikation offensichtlich nicht betroffen, wie zeitabhänge SHG-Messungen zeigen.

SH Imaging von verschiedenen Probenstellen, die mit UV-Laserimpulsen variierender Energien vorbestrahlt werden, zeigt einen Sättigungseffekt für die UV-induzierte Probenmodifikation. Eine Schwellfluenz von $\sim$ 0.47 $\mathrm{J/cm^2}$ wird ermittelt und als die Schmelzschwelle von grenzflächennahem Silizium interpretiert. Der Wert is vergleichbar mit einer Literarangabe ($\sim$ 0.36 $\mathrm{J/cm^2}$), die mit Hilfe eines ArF-Lasers ermittelt wurde (λ = 193 nm). Für Fluenzen unterhalb der Schmelzschwelle zeigt sich bei wiederholtem UV-Laserbeschuß ein akkumulatives Verhalten in der UV-induzierten Probenmodifikation. Dies deutet auf einen dosisabhängigen Effekt hin, der die Argumentation unterstützt, daß thermisch ausgelöste chemische Reaktionen für die mikroskopische Veränderung und die erhöhte Elektronenfallendichte in $\mathrm{Si/SiO_2}$ nach UV-Laserbestrahlung verantwortlich sind.

In Summe tragen die in dieser Dissertation vorgestellten SHG-Experimente zu einem tieferen und detaillierteren Verständnis der Ladungsträgerseparations- und Defekterzeugungsprozesse an der $\mathrm{Si/SiO_2}$ Grenzfläche bei. Insbesondere in Bezug auf den Löcherbeitrag zum zeitabhängigen SHG-Signal gibt es neue Erkenntnisse. Die Ergebnisse stehen einerseits im Zusammenhang technologisch wichtiger Fragen zur Anwendung und Herstellung ultradünner Oxidschichten in der MOS-Technologie. Andererseits sind sie von grundlegendem festkörperphysikalischem Interesse und bieten Einblicke insbesondere in die nichtlinearen optischen Eigenschaften von vergrabenen Grenzflächen zwischen kristallinen und amorphen Festkörpern.

Acknowledgements

Ich möchte mich bedanken bei:

- meinem Freund Erich Rohwer, durch den mir die Arbeit und auch die Freizeit in Stellenbosch viel gegeben hat. Er und seine Frau Inge gaben mir ein zweites zu Hause.
- thanks to my Dear friend Gillian Ahrendse, who was always there for me.
- meinem Betreuer und Doktorvater Prof. Dr. Herbert Stafast, der sich stets mit großem Interesse und Elan um seinen Doktoranden am andern Ende der Welt gekümmert und mich sehr unterstützt hat.
- meinem Chef in Südafrika, Prof. Hubertus von Bergmann, der mir alle mögliche Unterstützung entgegengebracht und mir alle Freiheiten gelassen hat. Also Prof. Piet Walters for all his help and moral support.
- the whole laser group and support team in Stellenbosch, Ulli Deutschländer, Christine Steinmann, Christine Ruperti, Pieter Neethling, Anton du Plessis, Trevor Gordon, Saturnin Ombinda, Timo Stehmann, Marcello Bartolini, John Burns, Boel Botha, Wolfgang Gauernack, David Pool, Stanley February, Faisel Timmey, Sybille Peterson as well as Greg Hillhouse.
- Herrn Prof. Dr. Dr. h.c. Alfred Laubereau für seine Unterstützung beim DAAD sowie sein Interesse an meiner Arbeit und daß er als externer Gutachter bereitstand.
- Herrn Prof. Dr. Roland Sauerbrey, für seine Bereitschaft als Zweitgutachter an meinem Promotionsverfahren teilzunehmen.
- den Herren Andy Thaller und Andreas Brodschelm für die Hilfe aus der Ferne.
- dem Deutschen Akademischen Austauschdienst e.V. für einen großen Teil meiner Brötchen (und Steaks).
- all my South African friends who kept me alive over the last three and a half years, particularly my housemates Aty and Cathy. Baie dankie, totsiens.
- meinen Eltern, daß sie mir nie reingeredet haben.
- Frau Anika Bosse, daß sie mir die Heimkehr aus Südafrika erleichtert hat:)

Tabellarischer Lebenslauf

Name:	Torsten Scheidt
Geburtsdatum:	27. November 1974
Geburtsort:	Würzburg
1985 - 1994:	Ignaz-Günther-Gymnasium Rosenheim
Jul. 1994:	Allgemeine Hochschulreife
Aug. - Sept. 1994:	6-wöchiges Industriepraktikum bei British Aerospace, Warton, Lancashire, Großbritannien
Okt. 1994 - Sept. 1995:	Wehrdienst bei 4./352 Panzergrenadier Batallion, Mellrichstadt und Stabsversorgungsstaffel., Heeresfliegerregiment 26, Roth
Nov. 1995 - Sept. 2001:	Studium der Physik an der Technischen Hochschule München
Apr. 1998:	4-wöchiges Industriepraktikum bei Deutsche Airbus AG, Hamburg
Jan. - Dez. 1999:	Studienaufenthalt an der *University of Stellenbosch*, Südafrika
Dez. 1999:	Südafrikanischer Hochschulabschluß: *Bachelor of Science with Honours (BSc. Hon.) (cum laude)*
03. Sept. 2001:	Hochschulabschluß: Diplom Physiker (Univ.), Technische Hochschule München, Thema der Diplomarbeit: Generation von solvatisierten Elektronen in Alkoholen
ab Okt. 2001:	Doktorand an der Physikalisch-Astronomischen Fakultät der Friedrich-Schiller-Universität Jena
Jan. 2002 - Dez. 2004:	Wissenschaftlicher Forschungsaufenthalt bei *Laser Research Institute, Physics Department*, *University of Stellenbosch*, Südafrika
Feb. 2002 - Jan 2004:	DAAD Doktorandenstipendium für Forschungsaufenthalt in Südafrika

Jena, den 4. Mai 2005

Ehrenwörtliche Erklärung

Ich erkläre hiermit ehrenwörtlich, daß ich die vorliegende Arbeit selbständig, ohne unzulässige Hilfe Dritter und ohne Benutzung anderer als der angegebenen Hilfsmittel und Literatur angefertigt habe. Die aus anderen Quellen direkt oder indirekt übernommenen Daten und Konzepte sind unter Angabe der Quelle gekennzeichnet. Weitere Personen waren an der inhaltlich-materiellen Erstellung der vorliegenden Arbeit nicht beteiligt. Insbesondere habe ich hierfür nicht die entgeltliche Hilfe von Vermittlungs- bzw. Beratungsdiensten (Promotionsberater oder andere Personen) in Anspruch genommen. Niemand hat von mir unmittelbar oder mittelbar geldwerte Leistungen für Arbeiten erhalten, die im Zusammenhang mit dem Inhalt der vorgelegten Dissertation stehen. Die Arbeit wurde bisher weder im In- noch im Ausland in gleicher oder ähnlicher Form einer anderen Prüfungsbehörde vorgelegt. Die geltende Promotionsordnung der Physikalisch-Astronomischen Fakultät ist mir bekannt. Ich versichere ehrenwörtlich, daß ich nach bestem Wissen die reine Wahrheit gesagt und nichts verschwiegen habe.

Jena, den 4. Mai 2005